

DOKUZ EYLÜL UNIVERSITY
GRADUATE SCHOOL OF NATURAL AND APPLIED SCIENCES

**PV SYSTEM CONNECTED TO GRID THROUGH
DC/DC BUCK-BOOST CONVERTER AND DC/AC
UNIPOLAR SWITCHING INVERTER**

by
Enes DURBABA

June, 2018
İZMİR

**PV SYSTEM CONNECTED TO GRID THROUGH
DC/DC BUCK-BOOST CONVERTER AND DC/AC
UNIPOLAR SWITCHING INVERTER**

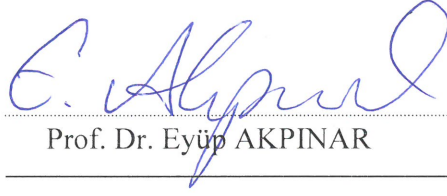
**A Thesis Submitted to the
Graduate School of Natural and Applied Sciences of Dokuz Eylül University
In Partial Fulfillment of the Requirements for the Degree of Master of Science
in Electrical and Electronics Engineering Program**

**by
Enes DURBABA**

**June, 2018
İZMİR**

M.Sc THESIS EXAMINATION RESULT FORM

We have read the thesis entitled “PV SYSTEM CONNECTED TO GRID THROUGH DC/DC BUCK-BOOST CONVERTER AND DC/AC UNIPOLAR SWITCHING INVERTER” completed by ENES DURBABA under supervision of PROF. DR. EYÜP AKPINAR and we certify that in our opinion it is fully adequate, in scope and in quality, as a thesis for the degree of Master of Science.


Prof. Dr. Eyüp AKPINAR

Supervisor


Prof. Dr. Engin Karatepe

(Jury Member)


Prof. Dr. Levent Eren

(Jury Member)



Prof. Dr. Latif SALUM

Director

Graduate School of Natural and Applied Sciences

ACKNOWLEDGMENTS

I express my deepest gratitude to my advisor Prof. Dr. Eyup AKPINAR for his guidance and support in every stage of my research. The technique background research experience and the research experience I have gained under his care will be valuable asset to me in the future.

I would like to thank Asst. Prof. Abdul Balikci, Res. Asst. Dr. Buket Turan Azizođlu, Ph.D student Ali Eren Kocamiř, and ađlar Yeřil for all support and encouragement.

I also want to express my gratitude towards my family for all their patience and support in my life. Especially, I want to thank to my mother who has played a very important role in all my success, to my father who always trusted in me in the works that I have stepped in, and finally to my wife and sister for all his sharing of my sadness and happiness. I would also like to thank to my friends for all their friendship, help and patience during my study.

Enes DURBABA

PV SYSTEM CONNECTED TO GRID THROUGH DC/DC BUCK-BOOST CONVERTER AND DC/AC UNIPOLAR SWITCHING INVERTERS

ABSTRACT

In this thesis, grid connected photovoltaic system with the DC to DC buck-boost, boost converters and DC/AC unipolar switched inverter has been analyzed. Two different DC to DC converters have been used to extract the maximum power available from the solar panel. The single-phase unipolar inverter has been used for the interface between the DC to DC converter and grid.

In this study, the leakage current flowing through parasitic capacitor of the photovoltaic panel has been taken into consideration and minimized with the help of inverter design. The time variation of the common mode voltage of the inverter causes the leakage current. Therefore, the existing photovoltaic inverter topologies have been investigated and a new photovoltaic inverter which provides the constant common mode voltage has been proposed. The mathematical models of the PV inverters have been analyzed in the Matlab/Simulink and tested in power quality laboratory.

Also, the effect of the model predictive current control on determination of maximum power point of the photovoltaic modules has been studied to determine the fast and robust maximum power point tracking system. The voltage controlled perturb and observe algorithm with the linear controllers (i.e, proportional-integral type controller) and the voltage controlled perturb and observe with the predictive current control method have been compared and simulation of these methods have been carried out in MATLAB/Simulink. Also, the particle swarm optimization algorithm is used in the simulation and two different MPPT algorithms are compared.

Keywords: PV inverter, Common mode voltage, Leakage current, Maximum power point tracking, Predictive current control, Particle swarm optimization, Perturb and observe method, DC to DC converters

ŞEBEKEYE DC/DC ALÇALTICI-YÜKSELTİCİ VE DC/AC İNVERTER ARACILIĞI İLE BAĞLI PV SİSTEM

ÖZ

Bu tez çalışmasında DA/DA alçaltıcı-yükseltici, yükseltici dönüştürücülerle ve tek kutup anahtarlamalı DA/AA çevirici aracılığı ile şebekeye bağlı fotovoltaik sistem incelenmiştir. İki farklı DA/DA dönüştürücü güneş panelinin sağlayabileceği maksimum gücü elde etmek için kullanılmıştır. Tek faz DA/AA çevirici güneş paneli ile şebeke arasında bağlantıyı kurmak için kullanılmıştır.

Bu tezde, DA/AA çeviricinin ortak mod gerilimindeki değişimin neden olduğu ve güneş panelinin kaçak kapasitelerinden akan kaçak akım incelenmiş ve DA/AA çevirici tasarımı ile bu kaçak akım azaltılmaya çalışılmıştır. Ortak mod gerilimindeki salınım kaçak akımın akmasına neden olmaktadır. Bu nedenle, literatürde var olan çevirici tasarımları incelenmiş ve ortak mod gerilimini sabit tutan yeni bir DA/AA çevirici önerilmiştir. Literatürde olan çeviriciler ve önerilen çevirici yapısı Matlab/Simulink ile incelenmiş ve güç kalitesi laboratuvarında test edilmiştir.

Ayrıca, hızlı ve doğru maksimum güç noktası takibi yapan algoritmaya karar vermek için, model ön-görünümlü akım kontrolcüsünün maksimum güç noktası takibi üzerindeki etkileri çalışılmıştır. Gerilim kontrollü değiştir-gözlemle algoritmasının doğrusal kontrol (oransal-integral kontrolcü) yöntemi ile beraber kullanıldığı ve gerilim kontrollü değiştir-gözlemle algoritmasının tahmini akım kontrolü ile beraber kullanıldığı kontrol metotları karşılaştırılmıştır ve MATLAB/Simulink kullanılarak benzetimleri yapılmıştır. Ayrıca, parçacık sürü optimizasyon algoritması benzetimlerde kullanılmış ve iki maksimum güç algoritması karşılaştırılmıştır.

Anahtar kelimeler: Fotovoltaik invertör, Ortak mod gerilimi, Kaçak akım, Maksimum güç noktası takibi, Öngörülen akım denetimi, Parçacık sürü optimizasyonu, Değiştir ve gözle yöntemi, DA- DA dönüştürücüler

CONTENTS

	Page
M.Sc THESIS EXAMINATION RESULT FORM.....	ii
ACKNOWLEDGMENTS	iii
ABSTRACT.....	iv
ÖZ	v
LIST OF FIGURES	viii
LIST OF TABLES	xii
CHAPTER ONE - INTRODUCTION	1
CHAPTER TWO - COMMON MODE VOLTAGE ANALYSIS.....	5
2.1 Definition of Differential Mode Voltage and Common Mode Voltage	5
2.2 Common Mode Voltage Analysis in Differential Amplifier.....	7
2.3 Common Mode and Differential Mode Voltages in the Single Phase Inverter.....	9
CHAPTER THREE - SINGLE PHASE TRANSFORMERLESS PHOTOVOLTAIC INVERTERS	11
3.1 Leakage Current Analysis in Transformerless Photovoltaic Inverters.....	14
3.1.1 H6 Type Inverter.....	18
3.1.2 oH5 Type Inverter.....	19
3.1.3 Improved H6 Type Inverter	20
3.1.4 Proposed Inverter Topology	22
3.2 Compression of Transformerless Photovoltaic Inverters	26
3.3 Efficiency Calculation Methods	28
CHAPTER FOUR - DC-DC CONVERTERS FOR MAXIMUM POWER POINT TRACKING	33

4.1 Two-Switch Non-Inverting Buck Boost Converter.....	35
4.2 One-Switch Inverting Buck Boost Converter	38
4.3 Boost Converter.....	39
CHAPTER FIVE - MPPT METHODS	41
5.1 Model Predictive Current Controller Based MPPT	43
5.1.1 Model Predictive Current Controlled Boost Converter	45
5.2 Model of Digital PI Controller	53
5.3 MPPT with Particle Swarm Optimization.....	55
CHAPTER SIX - SIMULATION AND EXPERIMENTAL RESULTS	59
6.1 Single Phase Photovoltaic Inverters Results	59
6.1.1 Proposed Topology	62
6.1.2 oH5 Topology.....	66
6.1.3 H6 and Improved H6 Topologies	68
6.2 Simulation and Efficiency Calculation with PSpice	70
6.3 Boost Converter with Model Predictive Current Control	74
6.3.1 Predicted Current Control with Perturb and Observe Algorithm	75
6.3.2 Particle Swarm Optimization with Duty Cycle Control	79
CHAPTER SEVEN - CONCLUSION	84
7.1 Future Work	85
REFERENCES.....	86

LIST OF FIGURES

	Page
Figure 1.1 (a) Photovoltaic cell, (b) Photovoltaic Module.....	2
Figure 1.2 Terminal characteristics of the PV array. (a) Voltage – Current characteristic, (b) Power – Voltage characteristic.....	2
Figure 1.3 Effect of the irradiance change (T=25°C). (a) Voltage & Current, (b) Power & Voltage.....	2
Figure 1.4. Leakage current.	4
Figure 2.1 Two wire system.....	5
Figure 2.2 Differential and common mode voltage analysis.	7
Figure 2.3 Differential amplifier circuit.....	7
Figure 2.4 Differential amplifier circuits with respect to the V_{dm} and V_{cm}	8
Figure 2.5 H-Bridge inverter topology.....	10
Figure 3.1 Grid connected photovoltaic system with high frequency (HF) transformers.....	11
Figure 3.2 Grid connected photovoltaic system with low frequency (LF) transformers.....	12
Figure 3.3 Grid connected transformerless photovoltaic system.	12
Figure 3.5 Grid connected H bridge based photovoltaic system.	15
Figure 3.6 Equivalent circuit.....	16
Figure 3.7 H6 Type Inverter Topology.....	18
Figure 3.8 Gate signals of H6 type inverter.....	19
Figure 3.9 oH5 Type Inverter Topology.....	19
Figure 3.10 Gate signals of oH5 type inverter.....	20
Figure 3.11 Improved H6 Inverter Topology.....	21
Figure 3.13 Proposed Topology.....	23
Figure 3.14. Four operation mode of proposed inverter for grid connection. (a) active current path for positive half cycle, (b) freewheeling modes for	

positive half cycle, (c) active current path for negative half cycle, (d) freewheeling modes for negative half cycle.....	24
Figure 3.15 Gate signals of improved H6 type inverter.....	25
Figure 3.16 Gate signal model in SPICE	30
Figure 3.17 Diode and IGBT switching characteristics for loss calculation.....	30
Figure 4.1 Voltage-Current (I-V) characteristic of the PV panel.	33
Figure 4.2 DC to DC Converter Connected to the PV Panel.	34
Figure 4.3 Operation regions; a) Buck Converter b) Boost Converter c) Buck-Boost converter.....	35
Figure 4.4 Two Switch Non-inverting Buck Boost Converter.	36
Figure 4.5 Gate Signals for the boost/buck or buck-boost mode operations	36
Figure 4.6 (a) Gate Signal, (b) Inductor Current (c) Indictor Voltage (d) Source Current (e) Output Capacitor Current.	37
Figure 4.7 Buck-Boost converter topology.....	39
Figure 4.8 Boost Converter Structure.	40
Figure 5.1 PV Cell model.	41
Figure 5.2 General structure of the predictive current controlled system.....	43
Figure 5.3 System block scheme with PI compensator.....	44
Figure 5.4 Block scheme of P&O algorithm.....	45
Figure 5.5 Model predictive control methods classifications.	46
Figure 5.6 Boost converter switching sate a) Switch closed b) Switch open.	46
Figure 5.7. Modulation methods. a) Trailing edge modulation b) Leading edge modulation c) Trailing triangle modulation.	48
Figure 5.8 Inductor current	48
Figure 5.9 One switching period.....	50
Figure 5.10 General wave form of the inductor current.....	52
Figure 5.11 Block diagram of the PI controller.	53
Figure 5.12 Flowchart of the PSO method.	56
Figure 6.1 Simulation model for constant DC link voltage condition.	59
Figure 6.2 Simulation model for the grid connected PV system	60
Figure 6.3 PV characteristic.....	60
Figure 6.4 Experimental setup.	62

Figure 6.5 Simulation results under the constant DC link voltage for proposed topology.....	63
Figure 6.6 Grid connected PV system with proposed inverter.	64
Figure 6.7 Experimental waveforms of proposed converter for grid connection for one grid period and for one switching period a) Inverter voltage and current b) V_{A0} c) V_{B0} d) (2xCommon mode voltage) $V_{A0}+V_{B0}$	64
Figure 6.8 Experimental waveforms of proposed converter for grid connection for one grid period and for one switching period a) Inverter voltage and current b) $V_{A0} - V_{B0}$ c) (2xCommon mode voltage) $V_{A0}+V_{B0}$ d) Leakage current.	65
Figure 6.9 Simulation results under the constant DC link voltage for oH5 topology.....	66
Figure 6.10 Grid connected PV system with oH5 inverter.	67
Figure 6.11 Experimental waveforms of oH5 converter for grid connection a) Inverter voltage and current b) $V_{A0} - V_{B0}$ c) (2xCommon mode voltage) $V_{A0}+V_{B0}$ d) Leakage current.	67
Figure 6.12 Grid connected PV system with H6 topology.	68
Figure 6.13 Experimental waveforms of improved H6 converter for grid connection a) Inverter voltage and current b) $V_{A0} - V_{B0}$ c) (2xCommon mode voltage) $V_{A0}+V_{B0}$ d) Leakage current.	69
Figure 6.14 Efficiency of the experimentally tested topologies.	69
Figure 6.15 Schematic of the converter in SPICE.	70
Figure 6.16 Picture of prototype used for experimental test.....	71
Figure 6.17 Simulation Results a) Differential mode voltage waveform b) Load current c) V_{A0} and V_{B0} voltage (Note that, V_{A0} is shifted to observe the waveform clearly) d) Common mode voltage ,time axis are same for all waveforms.	72
Figure 6.18 Experimental results a) Differential mode voltage wave form (50 V/div) b) Load current (1 A/div) c) V_{A0} and V_{B0} voltage (20 V/div) d) Common mode voltage (20 V/div)	73
Figure 6.19 Boost converter with predictive control.	74

Figure 6.20 Inductor current of the boost converter under the different modulation technique (trailing edge, trailing triangle and leading edge modulation)	75
Figure 6.21 PV system with boost converter.	76
Figure 6.22 PV characteristic.....	76
Figure 6.23 Digital PI controller used in Matlab.	77
Figure 6.24 Voltage oriented perturb observe algorithm results.....	77
Figure 6.25 Voltage oriented perturb observe algorithm with FS-MPC results.	78
Figure 6.26 Voltage oriented perturb observe algorithm with VCC-MPC results. ...	79
Figure 6.27 Simulation result of MPPT with PSO algorithm.	81
Figure 6.28 Zoomed current and voltage waveform of the PSO.	82
Figure 6.29 Inductance current of the boost converter with voltage oriented P&O. .	82
Figure 6.30 Inductance current of the boost converter with duty controlled P&O....	83
Figure 6.31 Inductance current of the boost converter with PSO.....	83

LIST OF TABLES

	Page
Table 3.1 The summary of standards for the photovoltaic system connected to the grid.....	13
Table 3.2 Comparison of topologies	28
Table 4.1 R_i values for converter types.....	35
Table 5.1 Controlled Current according to the modulation technique.....	50
Table 5.2 Slopes of the inductance of the basic converters	52
Table 6.1 Parameters of the grid connected inverters.....	61
Table 6.2 Circuit Parameters.....	71
Table 6.3 Power and Efficiency comparison	74
Table 6.4 Initial values and boundaries of parameters.....	80

CHAPTER ONE

INTRODUCTION

Energy policies and global warming have become important topic on the international agenda in the recent years. The use of renewable energy sources, both clean and economical, is of great importance to supply the ever-increasing need for energy. Moreover, the renewable energy sources are the most powerful alternative to the traditional fossil-fuel based energy sources which are creating the climate changes due to their negative effects on environmental conditions (Balikci et all, 2017).

The wind energy and solar energy are the sustainable renewable energy sources. Solar energy is the one of most potent renewable energy source since, they generate electricity from the solar irradiance without emitting the greenhouse gasses. Also, photovoltaic panels can be installed in unused geographical and residential areas such as; deserts and roofs. The increase of the energy demand and widespread use of the power electronic converters have prompted the researchers to investigate the high efficient and reliable energy conversion systems used in the photovoltaic (PV) systems. These systems have been mostly implemented at low and medium voltage levels.

Photovoltaic systems become prominent among the renewable energy sources. The global market in 2015 was 50 GW and it is exponentially increasing to be 100 GW in 2020 according to the global annual PV market scenario published by the European Photovoltaic Industry Association (“European solar energy,” 2017).

Solar cells which are made from the silicon and other materials, are the most basic component of the photovoltaic panels and it takes advantages of the p – n junction. Also, the solar panels are formed by parallel or series connection of solar cells. The photovoltaic cell and photovoltaic module are shown in Figure 1.1.

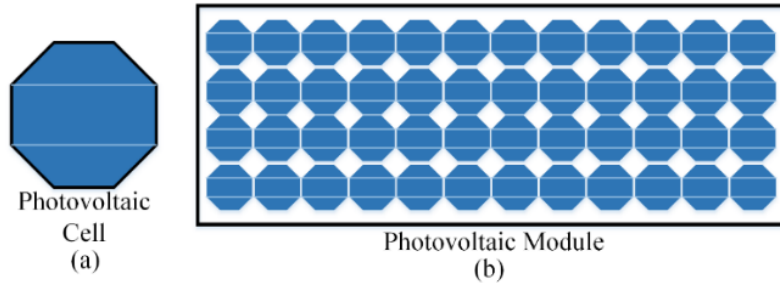


Figure 1.1 (a) Photovoltaic cell, (b) Photovoltaic Module

The photovoltaic arrays have nonlinear voltage-current characteristic with a single point in which maximum power can be extracted as shown in Figure 1.2. This point highly depends on the irradiance and temperature conditions.

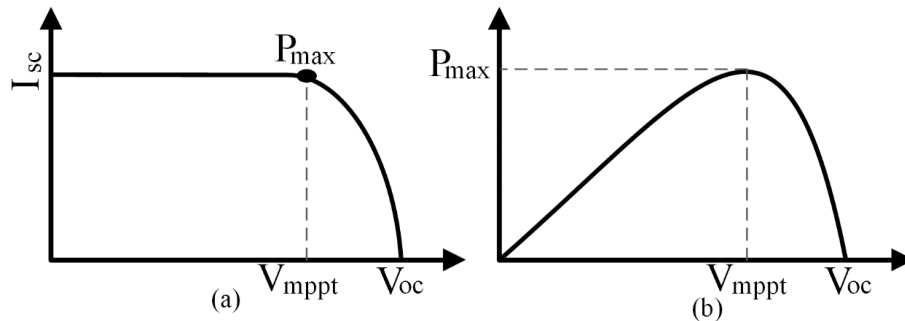


Figure 1.2 Terminal characteristics of the PV array. (a) Voltage – Current characteristic, (b) Power – Voltage characteristic

Figure 1.3 shows the effect of the irradiance change with constant temperature condition. Because of the change in the irradiance and temperature during the day, the maximum power that harvested from the PV panels change as shown in Figure 1.3.

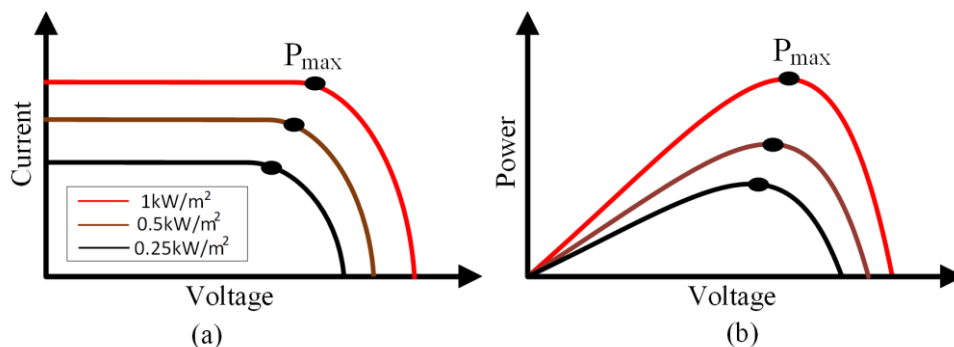


Figure 1.3 Effect of the irradiance change ($T=25^\circ\text{C}$). (a) Voltage & Current, (b) Power & Voltage

Maximum power point (MPPT) algorithm is needed because of these nonlinear characteristic and dependency of the environment conditions of the photovoltaic

module. The maximum power can be harvested by a DC / DC converter to be connected to the solar panel. These converters interface the PV panels and the loads or grid, and force the operating point of the PV panels at the MPP by changing the apparent impedance of the PV panel to match with the maximum power point impedance value (Taghvaei, et.al, 2013). Different types of the DC/DC converters (Buck, Boost, Buck-Boost, Cuk, Sepic, etc.) have been used for the MPPT operation. Moreover, many different MPPT algorithm and different type of control methods are proposed in literature. Such as; perturb and observe, incremental conductance, fuzzy logic control, neural network are the most popular MPPT algorithms. Moreover, researchers are increasingly interested in MPPT technique by using optimization based control strategy (model predictive control) in order to reduce the transient time and steady state error of the MPPT algorithms.

The photovoltaic modules generate DC power; so, they need an inverter to convert the DC electrical power into the AC at the grid frequency for feeding the electrical power to the grid. Therefore, grid connected inverters are the significant components of the photovoltaic system because of their function as an effective interface between the photovoltaic panels and grid (Islam, Mekhilef, & Hasan, 2015). These inverters can be designed with or without transformer. If the transformer is used, the galvanic isolation is exist. Thus, the dangerous leakage current for the safety does not flow through parasitic capacitor, which exist between photovoltaic cell and its grounded metal supported frame, of the photovoltaic panel. The value of the parasitic capacitors depends on: atmospheric condition, dusty, humidity, type of the photovoltaic panel and etc. Since, the transformer is bulky, expensive and also reduce the efficiency of the system, transformerless photovoltaic systems are designed in order to increase the efficiency of the system. On the other hand, if the transformer is not used, the galvanic isolation disappears. Therefore, common mode current flow through stray capacitor of the photovoltaic panel and this current reduce the personal safety, also it reduce the efficiency of the system. Figure 1.4 shows the common mode current flowing through the parasitic capacitor of the PV panel.

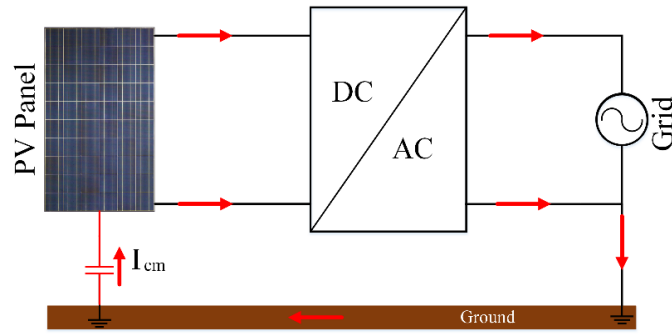


Figure 1.4 Leakage current

Content of the thesis can be summarized briefly as follows;

In chapter two, the common mode voltage is formulated on the network and its analysis with the proposed structure of the inverter is performed. The effects of the common mode voltage in photovoltaic system are described.

In chapter three, transformerless photovoltaic inverters are analyzed in detail. Firstly, the effect of the transformer is described, then the transformerless inverter structures are explained. Also, a new transformerless inverter topology is proposed and analyzed with all switching logic. Finally, the efficiency calculation methods are compared and the Matlab and Pspices package programs are used together in order to simulate the power electronic converters.

In chapter four, the DC to DC two switch buck-boost, boost, inverting buck/boost convert topology which are used for the MPPT operation are analyzed.

In chapter five, the predictive current control method is used in order to reduce the response time of the MPPT operation. The effective use of the predictive current control with the MPPT algorithm for the boost converter is analyzed. The perturb and observe based MPPT algorithm and the particle swarm optimization based MPPT algorithm are programmed and explained by using their flowchart.

In chapter six, all the results from the simulation and tested circuits are interpreted and compared. Finally, some conclusions of the research done in this thesis are given in chapter 7.

CHAPTER TWO

COMMON MODE VOLTAGE ANALYSIS

Rapid developments in the solid state technology have increased the use of power electronic system especially in renewable energy generation, space and transportation technology and power system applications (Zhu, 2013). The use of power electronics converters has led to significant improvements in productivity, power quality development and energy production. However, the power converter technology still has the ongoing problems to solve the problems such as; harmonic distortion, EMI effect etc., and the problems caused by common mode voltage (V_{cm}) which have drawn special attention since 1990s (Zhu, 2013).

2.1 Definition of Differential Mode Voltage and Common Mode Voltage

The common mode voltage is the voltage that is common to more than one line (typically a differential pair) to the circuit common. The value of the common mode voltage is equal to average of the voltage each line with respect to the local common or ground (González, Gubia, Lopez & Maroyo, 2008; Yang, Li, Gu, Cui & He, 2012). Differential mode voltage is equal to difference between the signals as the name implies (Khan, Brahim, Gastli & Benammar, 2017). Common mode voltage and differential mode voltage (V_{dm}) can be analyzed in many circuit or system such as; differential amplifier circuit, inverter circuits, etc. in the same way. As a simple example, Figure 2.1 shows two wire network where, V_1 and V_2 line voltage with respect to the common ground, Z_1 and Z_2 are line impedance and Z_{cm} and Z_{dm} shows the common mode and differential mode impedance respectively (Zhu, 2013).

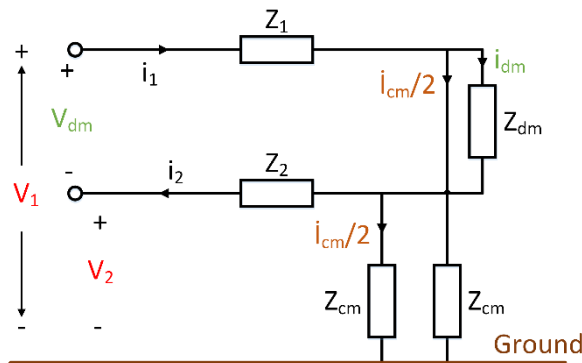


Figure 2.1 Two wire system

In here, common mode voltage and differential mode voltage can be calculated by using equations (2.1) and (2.2) respectively.

$$V_{cm} = \frac{V_1 + V_2}{2} \quad (2.1)$$

$$V_{dm} = V_1 - V_2 \quad (2.2)$$

The current i_1 and i_2 can be defined as (Zhu, 2013);

$$i_1 = i_{dm} + \frac{i_{cm}}{2} \quad (2.3)$$

$$i_2 = i_{dm} - \frac{i_{cm}}{2} \quad (2.4)$$

By using the equations (2.1) and (2.2), V_1 and V_2 expressed as (Li et al., 2015; Stiles, 2011);

$$V_1 = V_{cm} + \frac{V_{dm}}{2} \quad (2.5)$$

$$V_2 = V_{cm} - \frac{V_{dm}}{2} \quad (2.6)$$

Here, it is clear that, if there are two signal with same reference point, these signals have two component; common mode and differential mode voltage component. The differential mode voltage appears on both line with same magnitude but reverse direction (Zhu, 2013). On the other hand, the common mode voltage appears on both line with same phase and amplitude.

Figure 2.2 (a) shows a network (power electronics converters, differential amplifier circuits, etc.) that have two input signals with respect to the same reference point. Input voltages can be expressed in terms of the common mode and differential mode voltages as shown in Figure 2.2 (b) to analyze effect of the common and differential mode voltages on the network. So, whole system can be redrawn as in Figure 2.2 (c).

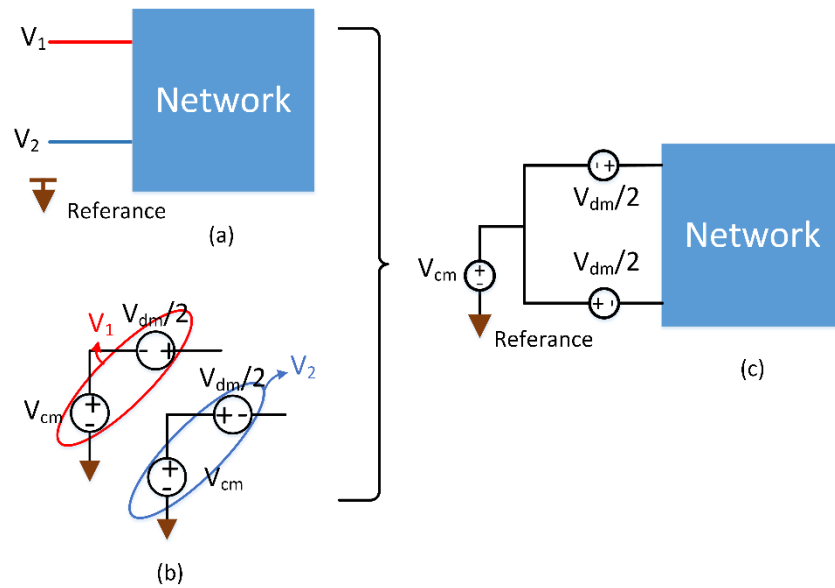


Figure 2.2 Differential and common mode voltage analysis

2.2 Common Mode Voltage Analysis in Differential Amplifier

Differential amplifier is an amplifier that amplifies the difference between the input signals. Figure 2.3 shows the simple differential amplifier circuit where V_1 and V_2 are the input voltages.

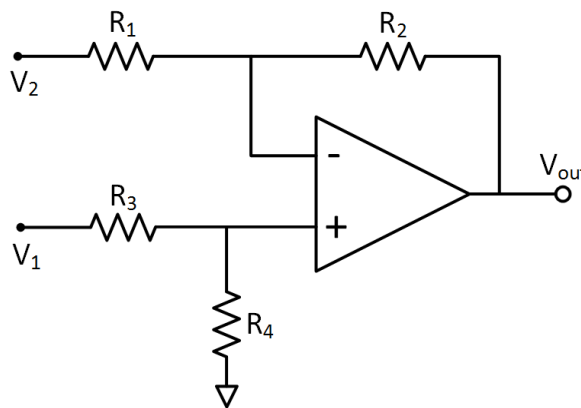


Figure 2.3 Differential amplifier circuit

The output voltage of differential amplifier can be obtained by using superposition method,

$$V_{out} = \left(1 + \frac{R_2}{R_1}\right) \left(\frac{R_4}{R_3 + R_4}\right) V_1 - \left(\frac{R_2}{R_1}\right) V_2 \quad (2.7)$$

The common mode and differential mode voltage can be defined like in equations (2.1) and (2.2) and thus, the input voltages can be redefined in terms of the V_{dm} and V_{cm} like in (2.5) and (2.6). Substitute equation (2.5) and (2.6) into equation (2.7), we get,

$$V_{out} = \left(1 + \frac{R_2}{R_1}\right) \left(\frac{R_4}{R_3 + R_4}\right) \left(V_{cm} + \frac{V_{dm}}{2}\right) - \left(\frac{R_2}{R_1}\right) \left(V_{cm} - \frac{V_{dm}}{2}\right) \quad (2.8)$$

If equation (2.8) is rearranged, we have,

$$V_{out} = \left[\left(1 + \frac{R_2}{R_1}\right) \left(\frac{R_4}{R_3 + R_4}\right) + \left(\frac{R_2}{R_1}\right) \right] \left(\frac{V_{dm}}{2}\right) + \left[\left(1 + \frac{R_2}{R_1}\right) \left(\frac{R_4}{R_3 + R_4}\right) - \left(\frac{R_2}{R_1}\right) \right] (V_{cm}) \quad (2.9)$$

The common mode and differential mode voltages can be used simultaneously on the differential amplifier as it is given in Figure 2.4.

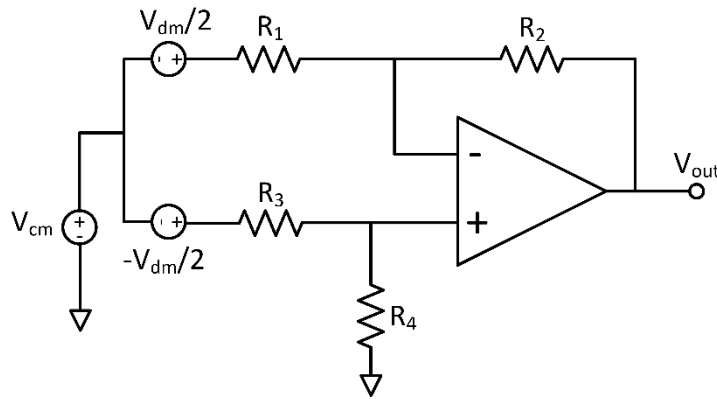


Figure 2.4 Differential amplifier circuits with respect to the V_{dm} and V_{cm}

Although it is assumed that the differential amplifier amplifies the differential mode voltage component of the input signals, common mode component of the input voltage is also appears at the output in practice and it also cause an error at the output signal. The effect of this error in a differential amplifier circuit is determined by common mode rejection ratio (CMRR), which is calculated as,

$$\text{CMRR} = 20\log\left(\frac{A_{\text{dm}}}{A_{\text{cm}}}\right) \quad (2.10)$$

and, A_{dm} and A_{cm} are differential and common mode gain respectively, which are defined as,

$$A_{\text{dm}} = \left[\left(1 + \frac{R_2}{R_1} \right) \left(\frac{R_4}{R_3 + R_4} \right) + \left(\frac{R_2}{R_1} \right) \right] \quad (2.11)$$

$$A_{\text{cm}} = \left[\left(1 + \frac{R_2}{R_1} \right) \left(\frac{R_4}{R_3 + R_4} \right) - \left(\frac{R_2}{R_1} \right) \right] \quad (2.12)$$

2.3 Common Mode and Differential Mode Voltages in the Single Phase Inverter

The common mode voltage cause problems in power converter system, if the leakage current is an important parameter for the system. In photovoltaic system, because of small thickness and large surface area of photovoltaic panels, there exist stray capacitors between ground and panel (Zhu, 2013). If there is a high frequency variation of common mode voltage in time and no galvanic isolation, a large amount of leakage current which reduce the safety and efficiency of the system can flow through between stray capacitor and ground. Moreover, in motor drive system, common mode voltage cause damage on the insulation of the system, induce shaft voltage and bearing current, so that the motor life is shorted (Zhu, 2013).

Switching state of semiconductor devices determine the common mode voltage of the power converters (Gu et al., 2013). In Figure 2.5, it is shown a single phase H-bridge inverter topology, where V_{DC} is the input DC voltage of the inverter and, V_{A0} and V_{B0} are the output terminals of the inverter.

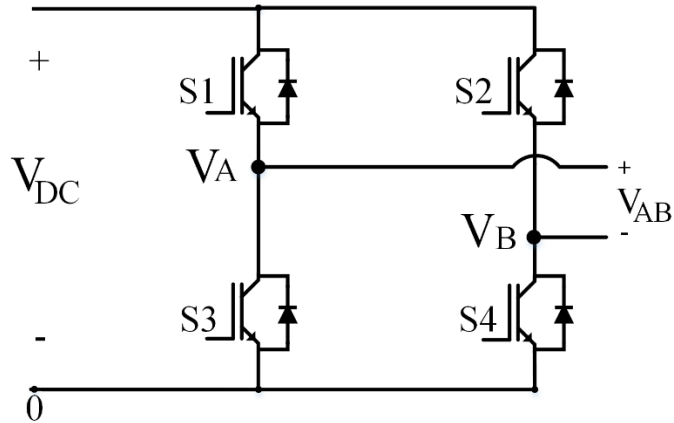


Figure 2.5 H-Bridge inverter topology

The differential mode voltage and common mode voltage can be computed as follows,

$$V_{AB} = V_{A0} - V_{B0} \quad (2.13)$$

$$V_{cm} = \frac{V_{A0} + V_{B0}}{2} \quad (2.14)$$

CHAPTER THREE

SINGLE PHASE TRANSFORMERLESS PHOTOVOLTAIC INVERTERS

A photovoltaic panel converts the solar energy to the electrical energy with DC voltage available, therefore an inverter is required as an interface to convert the DC voltage to the AC voltage at the grid frequency. Hence, a PV inverter is the essential component of a photovoltaic system because of their function as an effective interface between the photovoltaic panels and grid (Islam, Mekhilef, & Hasan, 2015). The common ground of the grid and the PV panel creates a path for the circulation of leakage current in the system. In order to avoid the leakage current circulation, the photovoltaic system needs either a galvanic isolation or the interface converter with the time-invariant common mode voltage (Yang & Blaabjerg, 2015; Khan et al., 2017).

The transformer can be used for galvanic isolation in the region of either high frequency operation of converter or low frequency (line frequency) operation at the grid side (Yang & Blaabjerg, 2015). Figure 3.1 shows the single phase grid connected photovoltaic system with high frequency (HF) transformer that adjusts the the input voltage level of the DC to AC inverter (Yang & Blaabjerg, 2015).

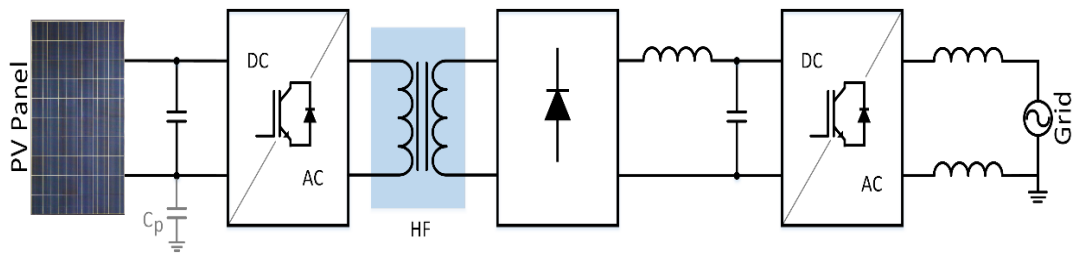


Figure 3.1 Grid connected photovoltaic system with high frequency (HF) transformers

A grid connected photovoltaic system can contain a transformer at grid side for the galvanic isolation (Khan et al., 2017). This line transformer disconnects the path of the leakage current (common mode current) circulation between the photovoltaic system and the grid. In this path, the parasitic capacitance (C_p) between photovoltaic panel and ground carries leakage current (Li et al., 2015). Besides that, the line transformer can also provide an interface between the inverter output terminals and

grid (Li et al., 2015). Figure 3.2 shows the single phase grid connected photovoltaic system with line frequency (LF) transformers and L_f represents the line filter.

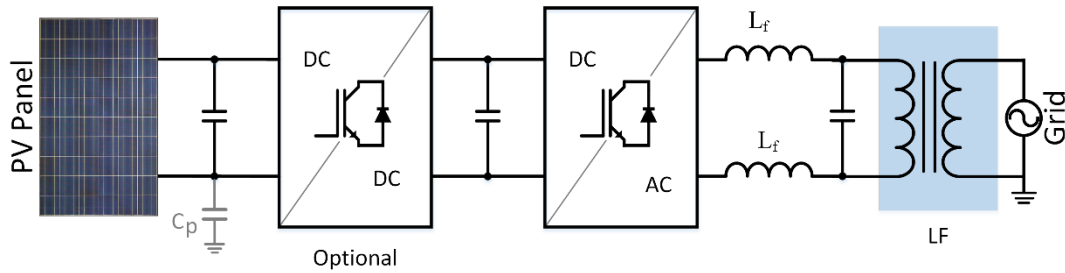


Figure 3.2 Grid connected photovoltaic system with low frequency (LF) transformers

Nevertheless, the use of transformer in photovoltaic system has many disadvantages. The line transformer is large, heavy and expensive because of its low frequency, also it is the source of additional power loss (Meneses, Blaabjerg, Garcia, & Cobos, 2013; Li et al., 2015). Moreover, use of the high frequency transformer increases the complexity of the system because power converter system needs the more power level, due to generated DC voltage first modulated at the high frequency and then converted the line frequency (Khan et al., 2017). Therefore it causes the extra losses, which reduces efficiency of the system, too.

Transformerless photovoltaic inverter can be used to avoid the disadvantages of the transformer mentioned above (Khan et al., 2017; Li et al., 2015). Figure 3.3 shows a transformerless photovoltaic system. Transformerless grid connected inverters have %1-2 higher efficiency than the ones with transformer (Khan et al., 2017). Furthermore, transformerless inverters have the advantages of smaller size, lower cost and weight when compared to the inverter with transformer (Khan et al., 2017; Li et al., 2015; Meneses et al., 2013).

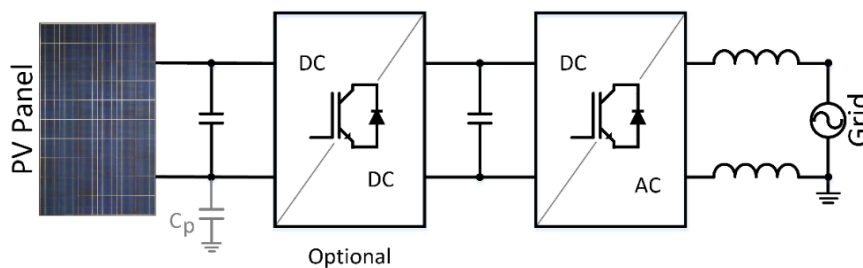


Figure 3.3 Grid connected transformerless photovoltaic system

However, the use of transformerless inverter in grid tied photovoltaic system is not simple. Like other grid connected inverters, transformerless inverters must satisfy grid connection standards which deal with the grid interface, power quality and grounding (Kjaer, Pedersen, & Blaabjerg, 2005). Table 3.1 shows that a summary of the grid connection standards of the photovoltaic system.

Table 3.1 The summary of standards for the photovoltaic system connected to the grid (Meneses et al., 2013)

Issue	IEC 61727		IEEE1547-2008		EN6100-3-2		VDE	
Nominal Power	10 kW		30 kW		16 A @ 230 V		-	
Harmonic Content	order (h)	Limit	order (h)	Limit	order (h)	Limit (A)	order (h)	Limit (A/MVA)
	3 - 9	4.0%	3 - 9	4.0%	3	2.3	3	3
	11 - 15	2.0%	11 - 15	2.0%	5	1.14	5	1.5
	17 - 21	1.5%	17 - 21	1.5%	7	0.77	7	1
	23 - 33	0.6%	23 - 33	0.6%	9	0.4	9	0.7
			>35	0.3%	11	0.33	11	0.5
					13	0.21	13	0.4
	Even harmonics are limited to 25% of the odd harmonics limits shown				(15 - 39)	2.25/h	17	0.3
							19	0.25
					2	1.08	23	0.2
					4	0.43	25	0.15
					6	0.3	(25 - 40)	3.75/h
	THD < 5%				(8 - 40)	1.84/h	Even	1.5/h
						>40	4.5/h	
DC current injection	Less than 1% of rated output current		Less than 0.5% of rated output current		< 0.22 A		< 1 A; max. Trip time 0.2s	
Voltage deviation	range %	time (s)	range %	time (s)	-		range %	time (s)
	V < 50	0.1	V < 50	0.16			V < 85	0.2
	50 ≤ V < 88	2	50 ≤ V < 88	26			V ≥ 110	0.2
	110 ≤ V < 120	2	110 ≤ V < 120	1				
	V ≥ 120	0.05	V ≥ 120	0.16				
Frequency deviation	range(Hz)	time (s)	range %	time (s)	-		range(Hz)	time (s)
	49 < f < 51	0.2	59.3 < f < 60.5	0.16			47.5 < f < 50.2	0.2
Leakage current	-		-		-		average current(mA)	time (s)
							30	0.3
							60	0.15
							100	0.04
							300 (peak)	0.3

If the galvanic connection is exist, the dangerous ground leakage current (common mode current) can circulate between the stray capacitor (C_p) of photovoltaic panels and ground, because of the varying common mode voltage (V_{cm}) generated by inverter. In Table 3.1, it can be seen that the maximum values of the leakage current according to the German codes VDE (300mA peak). Moreover, if there is no galvanic isolation (i.e., transformerless topology) in system, DC current can be injected into the grid, therefore the DC current is also limited by the standards given in Table 3.1.

3.1 Leakage Current Analysis in Transformerless Photovoltaic Inverters

The use of inverter without transformer in photovoltaic system becomes popular (Khan et al., 2017). Beside the advantages of the transformerless inverter, they have significant disadvantage of ground leakage current which flows between the ground and photovoltaic array through the parasitic capacitance (C_p). The parasitic capacitance exist between photovoltaic cell and its metal supported frame (Barater, Lorenzani, Concari, Franceschini, & Buticchi, 2016). Since, the metal supported frame is usually grounded for safety reasons, parasitic capacitor connected to the ground. Therefore, this leakage capacitor appears between ground and photovoltaic module. The value of the capacitor is varied because it depend on many factors such as weather condition, frame structure, surface of cell, dust, humidity, etc. (Barater et al., 2016). For example; monocrystalline and polycrystalline panels, value of the stray capacitor vary from 10 nF/kW to 100 nF/kW (Khan et al., 2017) and by considering the worst case scenario, the stray capacitor value of the BPSolar MSX120 photovoltaic module has been measured as 75 nF/kw (Islam et al., 2015). Moreover, the value of the capacitor can be measured up to 1000 nF/kW for thin film panels (Li et al., 2015).

The leakage ground current increases as the capacitance value increases, if no precautions are taken (Barater et al., 2016). The value of the leakage current depends on the voltage across the stray capacitor (V_{0n}) as it can be seen in equation (3.1),

$$i_{cm} = C_p \frac{dV_{0n}}{dt} \quad (3.1)$$

If there is no time-varying voltage across the capacitor terminals, the current of the capacitor is equal to zero. Therefore, the voltage across the parasitic capacitor must be limited both amplitude and frequency to limit the leakage current (Barater et al., 2016).

Figure 3.4 shows the single phase full bridge topology which is the basic structure for the PV inverters. The leakage current is analyzed in terms of L_1 and L_2 (representing the filter and grid inductance), R_g (representing the grid resistance), i_g and i_{cm} showing the grid current and leakage current, respectively.

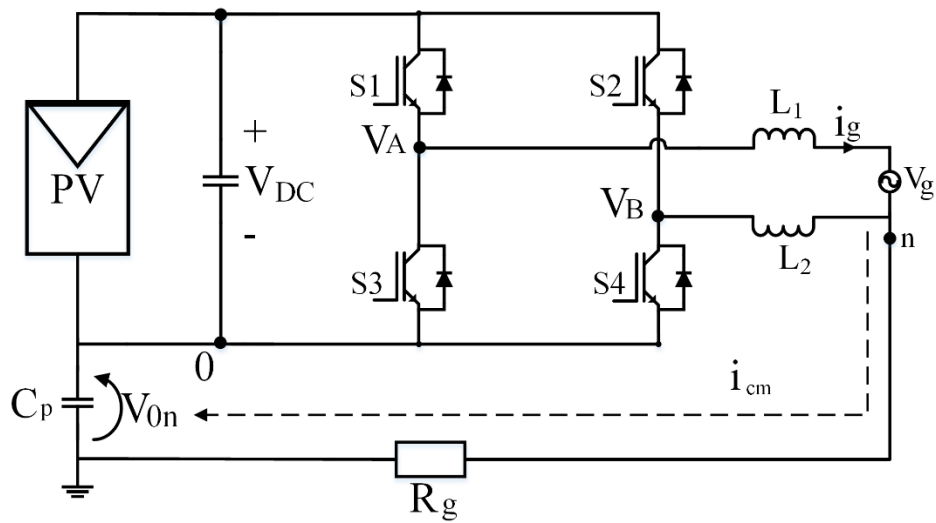


Figure 3.4 Grid connected H bridge based photovoltaic system

The common mode model of the grid connected H-bridge topology is shown in Figure 3.5 where, V_{cm} and V_{dm} shows the common mode voltage and differential mode voltage of the inverter output terminals V_{0A} and V_{0B} . Also, V_{gdm} and V_{gcm} show the grid terminals common mode and differential mode voltages.

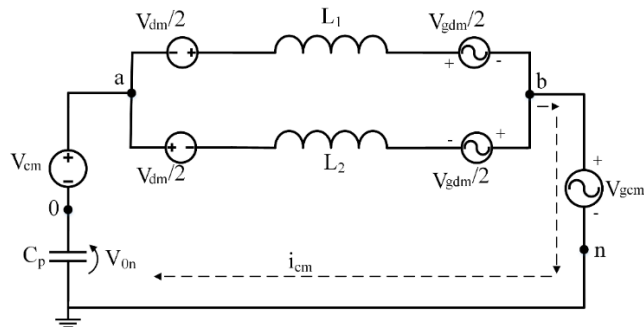


Figure 3.5 Grid connected H bridge based photovoltaic system

In Figure 3.5, R_g is neglected because its impedance lower than the other elements in the circuit (Kot, Stynski, Stepien, & Zeleski, 2016). The Thevenin equivalent circuit can be obtained by using superposition method between points “a” and “b” to find the stray capacitor voltage. Figure 3.6 shows the equivalent circuit of the whole system (Gonzales et al., 2008; Barater et al., 2016).

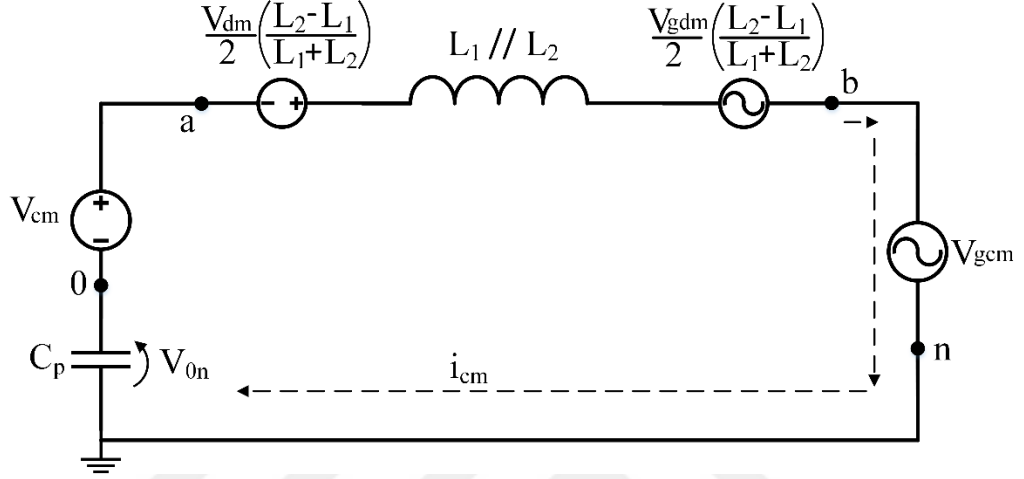


Figure 3.6 Equivalent circuit

The voltage across the parasitic capacitor (V_{0n}) can be calculated as follows,

$$V_{0n} = -V_{cm} - \frac{V_{dm}}{2} \left(\frac{L_2 - L_1}{L_1 + L_2} \right) + \frac{V_{gdm}}{2} \left(\frac{L_2 - L_1}{L_1 + L_2} \right) + V_{gcm} + \frac{di_{cm}}{dt} \left(\frac{L_1 L_2}{L_1 + L_2} \right) \quad (3.2)$$

The leakage current can be eliminated by keeping the stray capacitor voltage at constant value or equal to zero. The grid common mode voltage (V_{gcm}) and differential mode voltage (V_{gdm}), which are the low frequency component, can be ignored because of the high value of the parasitic capacitive impedance at grid frequency (Barater et al., 2016). When the inverter output inductances (L_1 and L_2) are selected equally, the effect of the differential mode voltages (V_{dm} and V_{gdm}) can be also canceled out (Gonzales et al., 2008). On the other hand, if the inverter common mode voltage (V_{cm}) which consists of high frequency harmonic components becomes a significant important parameter, since the stray capacitance's impedance has low impedance characteristic at higher frequency values (Barater et al., 2016). Due to the aforementioned assumptions, inverter common mode voltage must be maintained constant to limit the leakage current.

The common mode voltage can be controlled by setting the switching logic and modifying the inverter topology. In literature, it has been proposed many different inverters which keep the common mode voltage constant by changing the inverter topology or modulation strategy (switching logic) (Khan et al., 2017). Moreover, there are many different approaches in literature to classify the transformerless inverters (Islam et al., 2015). One of the most comprehensive classification can be found in (Li et al., 2015). According to (Li et al., 2015), the transformerless inverters can be divided into two main group as symmetrical inductor-based group and asymmetrical inductor-based group.

Half bridge based inverters proposed in (Gonzâles et al., 2008 ;Bruckner et al., 2005; Kouro et al., 2010; Schweizer et al., 2013) which need twice grid peak voltage at dc link side, dual buck converter based inverters proposed in (Xiao et al., 2011; Arauzo et al., 2010) which include two buck converter, virtual dc bus based inverters proposed in (Gu et al., 2013; Wang et al., 2008), line frequency unfolding transformerless inverters proposed in (Prasad et al., 2008), are some of the asymmetrical inductor based inverters ($L_1=0$ or $L_2=0$). But, asymmetrical inductor based photovoltaic inverters aren't the subject of this thesis.

Full bridge inverter that is one of the inverter with the symmetrical inductor structures, can eliminate the common mode voltage variation. According to the applied switching technique, it can generate two different output voltage wave form; unipolar or bipolar output voltage. If unipolar switching algorithm is applied, the common mode voltage does not stay constant, it oscillates between zero voltage level and half of the input voltage level according to the switching condition. The oscillation of common mode voltage has been prevented by using the bipolar switching algorithm. But, efficiency of bipolar switching algorithm is lower than the unipolar technique because, two diodes and two IGBTs are switching at the switching frequency with whole input voltage (Gonzâles et al., 2008). Therefore, the new solution has been created with hybrid design consisting of bipolar operation of switching devices and generation of unipolar output voltage by modifying the converter. H6, optimized H5 (oH5), improved H6, H5, HERIC, AC-based H6, active

clamping topology, passive clamping topology are some of the inverters developed with this approach (Li et al., 2015).

H6, oH5 and improved H6 structures which are analyzed here are the inverters having the symmetrical inductors. Also, a new inverter topology called “active clamped snubber based inverter” has been proposed in this thesis. The proposed topology has been connected to the grid and tested in laboratory. H6 structure has been tested only as an inverter without grid connection. Beside, oH5 and improved H6 topologies have been analyzed only simulation environment by using MATLAB/Simulink and SPICE package programs.

3.1.1 H6 Type Inverter

H6 type inverter has been proposed by Gonzales et al. (2007). This inverter is designed with six controlled switches, two diodes and two capacitors. It is a transformerless single phase PV inverter that eliminates the leakage current. Moreover, this inverter is named as passive clamped dc-based NPC (neutral point clamped) H6 inverter in Li et al., 2015. Figure 3.7 shows the circuit topology of this inverter.

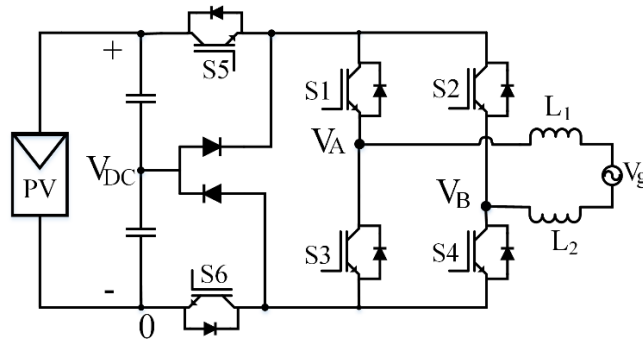


Figure 3.7 H6 Type Inverter Topology

S5 and S6 switches are used for decoupling the DC voltage from the AC terminals at the zero output voltage level. Also, two diodes are connected to the midpoint of the DC-link capacitors to get constant common mode voltage during the freewheeling instants. This topology has special switching logic. While S1 and S4 switches are conducting during whole positive half cycle, S2-S3 and S5-S6 switches commutate complementarily at the switching frequency. For the negative half cycle

S2 and S3 are turned on. S1-S4 and S5-S6 switches commutate complementarily at the switching frequency as well. Figure 3.8 shows the switching algorithm of the H6 type inverter.

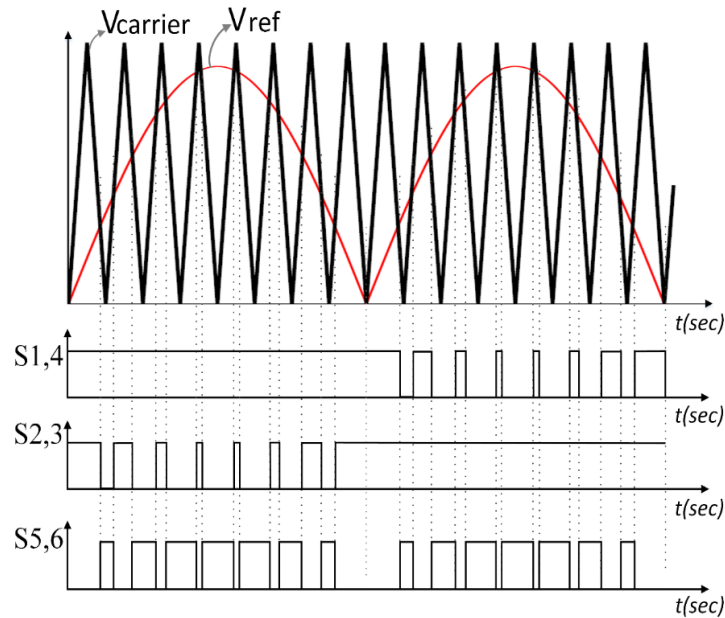


Figure 3.8 Gate signals of H6 type inverter

3.1.2 oH5 Type Inverter

Optimized H5 (oH5) topology which is proposed by Xiao et al in 2011, is one of the most efficient transformerless photovoltaic inverter (Xiao, Xie, Chen, & Huang, 2011). This inverter structure includes two capacitors and six IGBTs as in Figure 3.9. Instead of diodes used in H6 topology, oH5 topology uses the active switching device (S6 IGBT) in freewheeling instants.

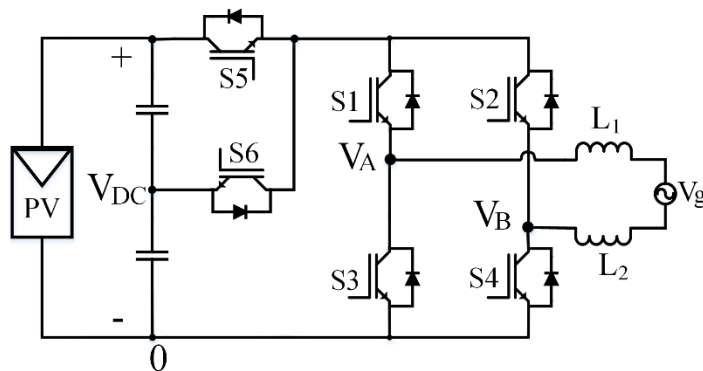


Figure 3.9 oH5 Type Inverter Topology

Figure 3.10 shows the switching logic of the oH5 topology. Switch S5 is turned on during positive and negative half cycle of grid current. In freewheeling modes of positive half cycle, S3, S4 and S5 switches are turned off, and S1-S2 switches are turned on. S6 is turned on in order to guarantee that the common mode voltage is clamped to the half of the input voltage. In negative freewheeling interval, S1, S2 and S5 switches are turned off, and S3-S4 switches are turned on. V_{A0} and V_{B0} voltages are clamped to the mid-point of the input capacitors voltage level since S6 is turned on. Therefore, the common mode voltage is equal to half of the input voltage in all switching intervals.

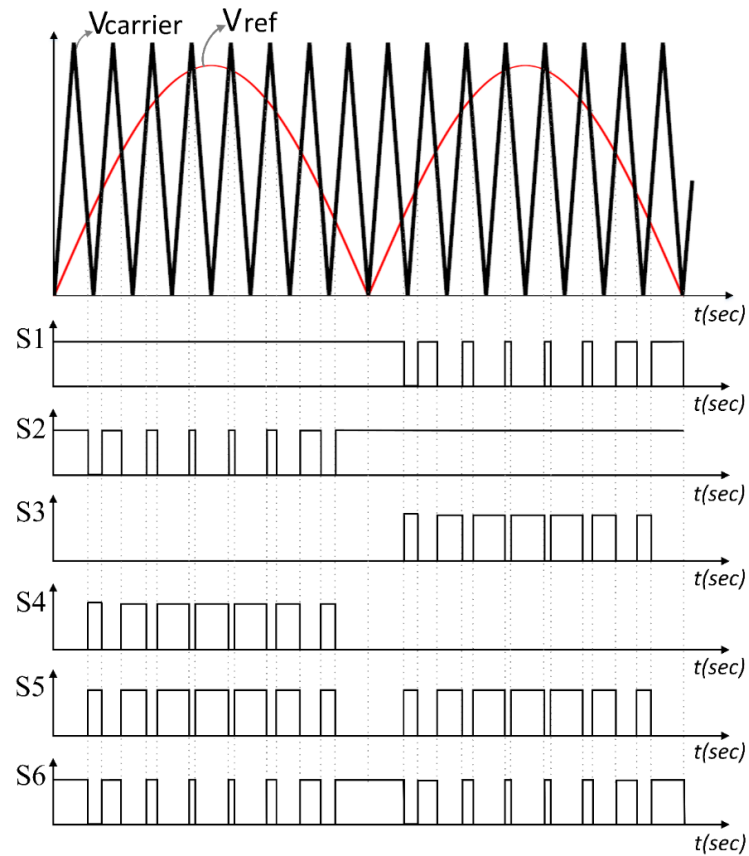


Figure 3.10 Gate signals of oH5 type inverter

3.1.3 Improved H6 Type Inverter

Improved H6 topology is the one of the proposed inverter structures to keep the common mode voltage constant. This structure is formed by adding two symmetrical switches (S5-S6) to the traditional H bridge structure as shown Figure 3.11.

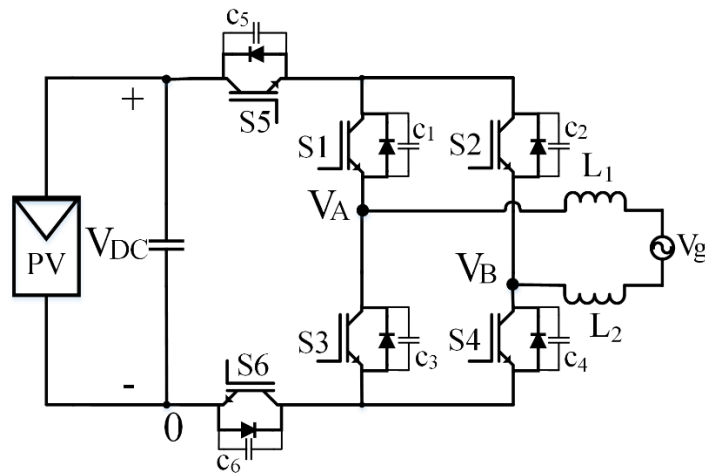


Figure 3.11 Improved H6 Inverter Topology

Figure 3.12 shows the gate drive logic with unipolar SPWM of the improved H6 topology. One leg of the H-bridge including S1 and S2 is commutating at grid frequency and the other leg (S3-S4) is operating at switching frequency like standard unipolar SPWM. The additional switches (S5 and S6) are used for generating the DC decoupling states.

In positive half cycle, two different modes are exist; power processing (generating the V_{DC} level at the output terminal) and DC decoupling (generating the zero voltage level). S1 and S6 switches are always on state, and S4-S5 switches are commutating at the switching frequency with the complementarily to S2 and S3. S4- S5 are turned on to generate non-zero voltage level, and S2-S3 are tuned on to generate the DC decoupling modes. In the DC decoupling mode, inner capacitor of the IGBTs, which generate the resonant circuit with the filter inductances, are used to kept common mode voltage constant. As in positive half cycle, two different modes are exist; one of them is power processing (generate the $-V_{DC}$ level at the output terminal) interval and the other is DC decoupling (generating the zero voltage level) in negative half cycle. At this time, S2 and S5 switches are always ON, and S3-S6 switches are commutating at the switching frequency with the complementarily to S1 and S4. S3- S6 are turned on to generate the power processing, and S1-S4 are tuned on to generate the DC decoupling modes. Like the positive DC decoupling stages, the inner capacitor of the IGBTs, which generate the resonant circuit with the filter inductances, are used to kept common mode voltage constant. As a result, the

common mode voltage is constant and equal to the half of the input voltage ($V_{DC}/2$) during the four operation modes.

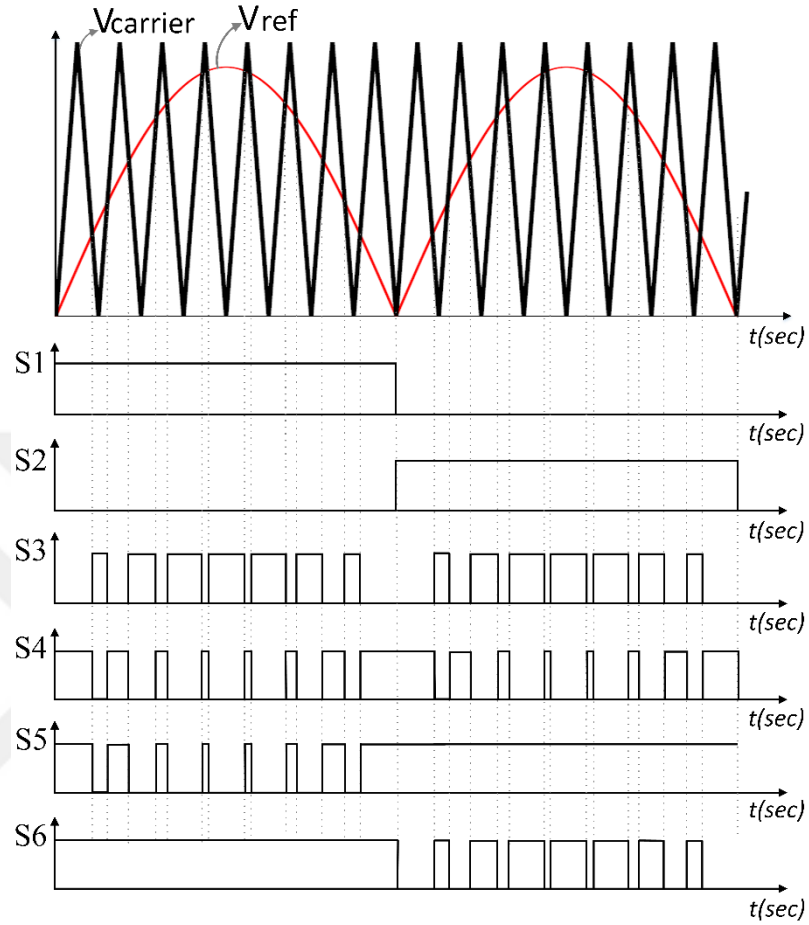


Figure 3.12 Gate signals of improved H6 type inverter

3.1.4 Proposed Inverter Topology

The proposed topology consists of seven IGBTs and two RC snubber circuits as shown in Figure 3.13. This proposed topology is named as active clamped snubber based inverter. The active clamping IGBT ($S7$) is operated only during the freewheeling instant. A small amount of leakage current flows through its collector when it is turned on to hold the common mode voltage constant. The collector emitter voltage of the $S7$ switch is equal to the DC link voltage (V_{DC}) when it is switched off. Two RC snubber circuits are used in parallel with two decoupling IGBTs. The capacitor of the snubber circuit is charged to the half of DC link voltage level and it retains the common mode voltage constant. The snubber also reduces the

switching losses of S5 and S6 (Naayagi et al. 2011). The RC time constant determines how fast the common mode voltage will be tracked.

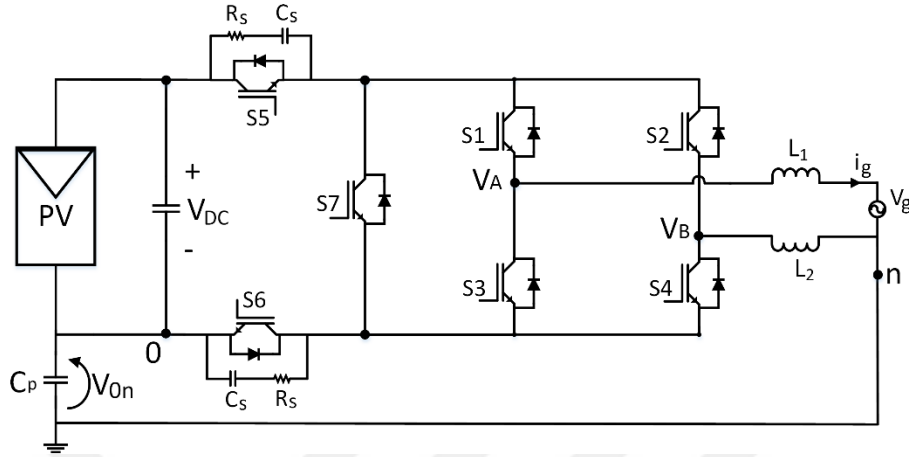


Figure 3.13 Proposed Topology

There are four modes of operation over one period of the grid current. The active current path in the inverter during the positive half cycle is seen in Figure 3.14(a). The differential mode voltage can be written in terms of V_{A0} and V_{B0} as follows;

$$V_{DM} = V_{A0} - V_{B0} \quad (3.3)$$

The common mode voltage is equal to;

$$V_{CM} = \frac{(V_{A0} + V_{B0})}{2} \quad (3.4)$$

As it is given in Figure 3.15, during the positive half cycle of the reference sinusoidal signal, S1 is continuously conducting, whereas S3 is at off position. These two switches commute alternately. S4, S5, and S6 complementarily commutates S2 at the frequency (switching frequency) of carrier wave. In this period, the common mode voltage is;

$$V_{CM} = \frac{(V_{DC} + 0)}{2} = \frac{V_{DC}}{2} \quad (3.5)$$

In order to obtain the freewheeling path, S4 is turned off and S2 is turned on during the zero level of inverter output voltage. Also, S5 and S6 switches are turned off and active clamping switch S7 turns on simultaneously to keep the common

mode voltage constant. During the conduction of the S7 switch, the current flows through the snubber circuit as seen in Figure 3.14(b) until the snubber capacitor's voltage value reaches to the half of the DC voltage level. The common mode voltage is retained at the previous value as follows;

$$V_{CM} = \frac{(V_{DC}/2 + V_{DC}/2)}{2} = \frac{V_{DC}}{2} \quad (3.6)$$

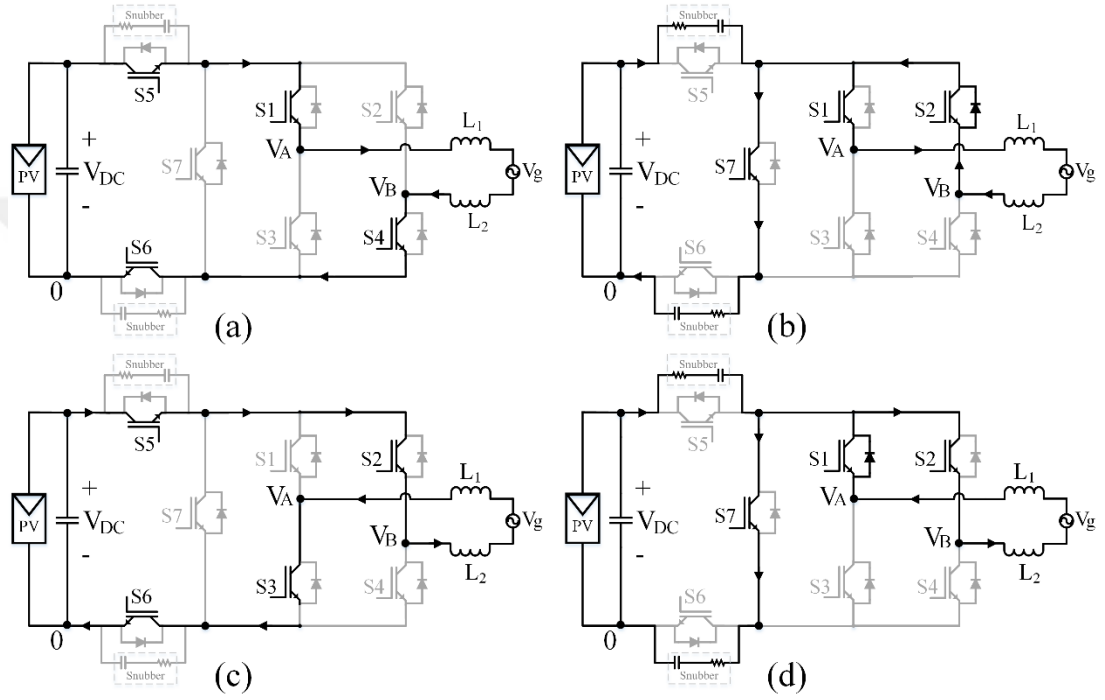


Figure 3.14 Four operation mode of proposed inverter for grid connection. (a) active current path for positive half cycle, (b) freewheeling modes for positive half cycle, (c) active current path for negative half cycle, (d) freewheeling modes for negative half cycle

The active current path during the negative half cycle of the reference wave is depicted in Figure 3.14 (c). In this case, while S2 is always conducting, S4 is turned off. S2 and S4 are always commutating alternately. The common mode voltage is given in (3.7) during this mode of operation.

$$V_{CM} = \frac{(0 + V_{DC})}{2} = \frac{V_{DC}}{2} \quad (3.7)$$

In the freewheeling mode during the negative half cycle, the constant common mode voltage is obtained as shown in Figure 3.14(d). The snubber capacitor voltages

are charged to the half of the DC link voltage since the capacitance values are same. In this instants, small amount of current flows through on the S7 IGBT until the snubber capacitors charged. The common mode voltage is given below;

$$V_{CM} = \frac{(V_{DC}/2 + V_{DC}/2)}{2} = \frac{V_{DC}}{2} \quad (3.8)$$

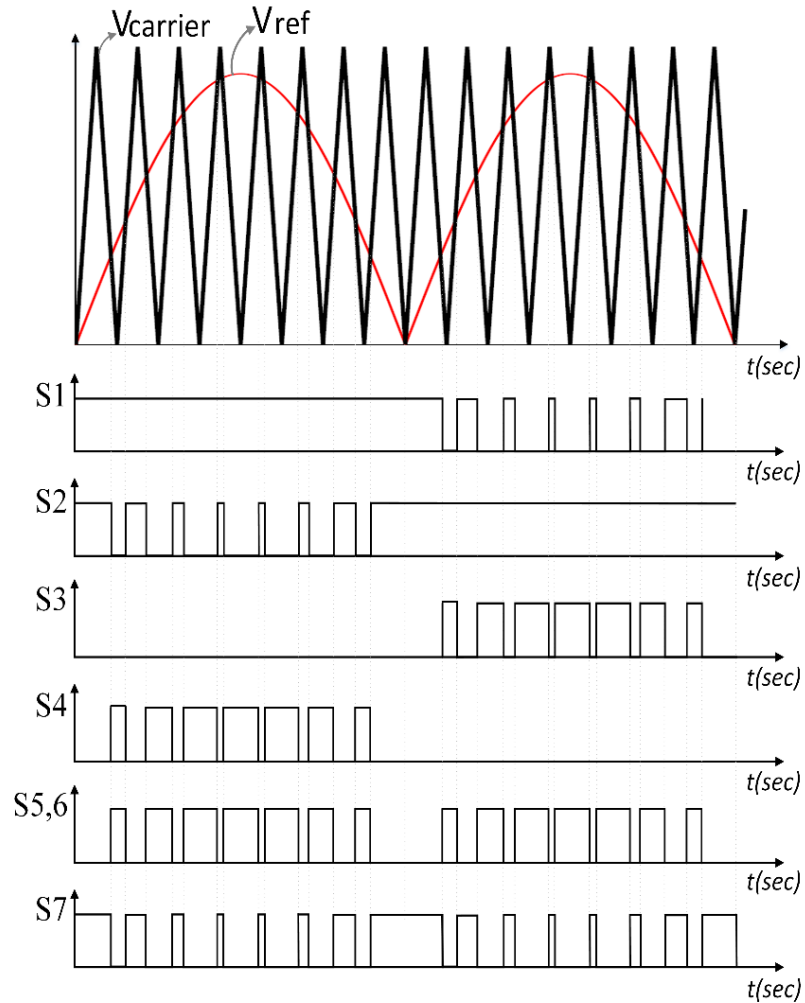


Figure 3.15 Gate signals of improved H6 type inverter

The common mode voltage in all operation modes is constant for the unipolar switching logic and it is equal to the half of the DC link voltage ($V_{DC}/2$). The snubber circuit ensures that the circuit remains at a constant common mode voltage without fluctuations during the freewheeling periods. The conduction of the switch (S7) guarantees the voltage of the snubber circuit shared equally at the half of the DC voltage level. If the S7 switch was not operated, the snubber capacitors would not be

charged since no current would flow through the snubber circuit at the freewheeling instant. This would cause the floating voltages of the inverter terminals (V_{A0} , V_{B0}).

Gate signals of the proposed inverter for SPWM are shown in Figure 3.15. It is clearly seen that S1, S2, S3, and S4 are operated with the unipolar switching scheme, as the S5 and S6 work simultaneously as the complement of the S7 switch. Therefore, unipolar output voltage is generated at the output terminals of the inverter.

3.2 Compression of Transformerless Photovoltaic Inverters

The PV inverters can be compared in terms of their efficiencies, number of devices used in topology, stability of common mode voltage, switching algorithms and etc. The advantages and disadvantages of the proposed topology are compared with H6, optimized H5 and improved H6 as given in Table 3.2.

The number of the component used in topology is an important parameter for compare the existing topologies. DC link capacitors are one of the factors that determine the reliability, life span and usability of the photovoltaic inverters. The DC link capacitors are the most vulnerable components of the inverters and their lifetime should be considered for the whole system reliability and life span (Wang, & Blaabjerg, 2014; Buticchi, Barater, Lorenzani, & Franceschini, 2012). The failure ratio of the capacitors is observed as 30 percent among the main components in the power electronic systems (Wang, Liserre, & Blaabjerg, 2013). The capacitor voltages may not be evenly distributed in topologies using two series connected DC-link capacitors. The deviation of the capacitor's instantaneous voltage values increases the ground current. The PV inverters designed with two DC-link capacitors (Xiao et al., 2011; Gonzalez et al., 2007) need software solutions or some extra components to guarantee that the capacitor voltages are balanced. A resistor voltage divider circuit can also be connected in parallel to the capacitors to ensure the equal voltage sharing between the capacitors. These solutions in hardware can cause more losses, heating problems or require a complicated algorithm in the software. Although H6 and Optimized H5 topologies have constant common mode voltages (Freddy, Rahim, Hew, & Che, 2014), they require capacitor voltages balancing (Xiao et al., 2011).

The junction capacitances of the switching devices are taken into account for controlling the leakage current in the circuit (Azary, Sabahi, Babaei, Meinagh, 2018). But those capacitors are internal units in the solid-state devices and their values change device to device in the range of picofarads or nanofarads. Therefore, their effectiveness on the circuit operation is highly dependent on the distributed stray capacitors in the electrical network. The ground leakage current could not be completely taken under the control because of the possible resonance with the distributed stray inductances (Li et al., 2015; Khan, Ben-Brahim, Gastli, & Benammar, 2017). Despite the fact that the improved H6 topologies does not require voltage balancing, the common mode voltages is floating due to junction capacitors are used to keep the common mode voltage constant (Khan et al., 2017).

The unipolar output voltage form is desired at the output terminals of the inverters, since it increases the efficiency of the system. The unipolar output voltage could be generated by the simple switching logic. However, the standard unipolar switching logic can not be used in H6 topology. The common gate drivers are not used in this topology, since the common driver circuit does not generate the same switching condition at same time. Therefore, it require complicated switching logic to produce the unipolar output voltage.

The common mode voltage is maintained constant while the voltage balancing is not required under favor of using one capacitor in the proposed topology. Also, in this topology, the resonance current path does not occur, this topology utilizes the snubber circuits to keep the common mode voltage constant. Even though the proposed topology has an additional switch, the current carrying capacity of it is good enough to carry the snubber current for a very short time. Small amount of current flows through on the additional switch (S7) until the snubber capacitor charged at the freewheeling instants. Moreover, the unipolar output voltage can be generated by using standard unipolar switching logic.

Table 3.2 Comparison of topologies

	H6	Optimized H5	Improved H6	Proposed
Number of Devices	6 IGBTs 2 Diodes 2 Capacitors	6 IGBTs 2 Capacitors	6 IGBTs 1 Capacitor	7 IGBTs 1 Capacitor 2 snubber
Common Mode Voltage	Constant	Constant	Float	Constant
Unipolar Switching Logic	Complicated	Standard	Standard	Standard
Capacitor Voltage Balance	Required	Required	Not Required	Not Required
Resonance Current Circuit	Not Occurred	Not Occurred	Occurred	Not Occurred

3.3 Efficiency Calculation Methods

Since the efficiency of the inverters has a crucial importance for PV applications, the estimation method should be accurate as much as it is possible and fairly applicable for comparison. The most common method is the use of manufacturing data on switching losses related to junction temperature (Mitova et al., 2014). Moreover, the linearized switching characteristics of the semiconductor devices based on curve fitting are usually preferred in the estimation of the efficiency (Xiao et al., 2011). The calculation based on the experimentally recorded switching waveforms such as collector-emitter voltage and collector current is also an alternative approach (Schweizer, & Kolar, 2013). When the comparison between the alternative converters is the main target then the estimation should cover the same assumptions such as the same ambient conditions and soldering the network components, same switching devices, and same operating conditions. The most reliable comparison can be performed with a dedicated simulation program used for converter analysis. Furthermore, the estimation of efficiency can be carried out by taking into account the experimental measurement, and a dedicated analysis based on the use of the MATLAB and the PSPICE (Balikci, et al., 2017).

When the inverter input voltage, input current, load voltage and load current are recorded, the average input power to the inverter and output power supplied to the

load can be computed by using equations (3.9) and (3.10) in the software facility of oscilloscope.

$$P_{in} = \frac{1}{T_g} \int_0^{T_g} (V_{DC}(t) \cdot i_{DC}(t)) dt \quad (3.9)$$

$$P_{out} = \frac{1}{T_g} \int_0^{T_g} ((v_{A0}(t) - v_{B0}(t)) \cdot i_L(t)) dt \quad (3.10)$$

The efficiency of the inverters is usually given in the papers by using the manufacturer data of solid-state devices (Picas et al., 2015), testing the converter circuits (Azri, Rahim, & Halim, 2015) or based on estimation from simulation (Barater et al., 2012). The highest efficiency with the minimum cost is the preference for the selection of the inverters; hence all papers published give efficiency comparison between the proposed converter and conventional ones. This effort is usually time consuming part because it requires a test setup of conventional circuits in addition to proposed circuit. Therefore, the MATLAB/Simulink and the SPICE package programs can be used together in order to analyze the converters efficiency.

The operation of converter has been simulated in MATLAB. The simulation of the same converter in the SPICE could be carried out by using the logic gates and optocouplers from its library. In this case, a complex structure would be required to drive the IGBTs and the simulation would take very long time and could cause convergence problems in solver. In this analysis, the efficiency calculation on the converter is the main objective, therefore, the switching characteristics of the solid state devices are used from the SPICE library and the gate power loss of the IGBTs is neglected. Then the gate signals are generated in MATLAB program and transferred as a “text file” to the SPICE program. Thus, the circuit is analyzed in the SPICE during the transient and the steady-state operation with the pre-specified gating signals in a short execution time (Balikci, et al., 2017).

The gate signals generated from the MATLAB must be extracted to the workspace in the “array” format. Then the data is stored in the “text files” for each IGBT. The source components located in the SPICE library execute the program by importing the six “text files” corresponding to IGBTs. The V

PWL_F_RE_FOREVER is one of the components in the source library and it calls the “text files” during the analysis of circuit over the multiple periods defined by the user as in Figure 3.16.

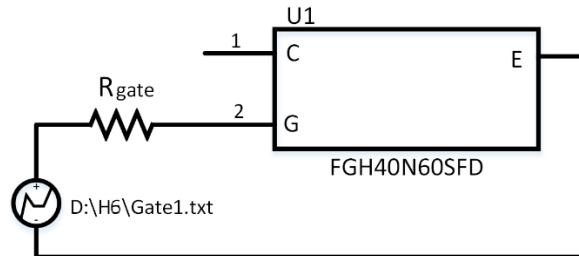


Figure 3.16 Gate signal model in SPICE

The SPICE simulation has calculated the efficiency by using the equations (3.9) and (3.10). Since the efficiency has been computed from the input and output powers on the inverter, the switching losses are already taken into consideration.

The loss calculation for the switching power semiconductor devices (i.e., IGBTs and diodes) based on manufacturing data is explained in (Xiao et al., 2011). The efficiency of the converter can also be estimated by using the losses of the semiconductor devices. The switching characteristics of these devices during the turn-on and turn-off intervals are given in Figure 3.17.

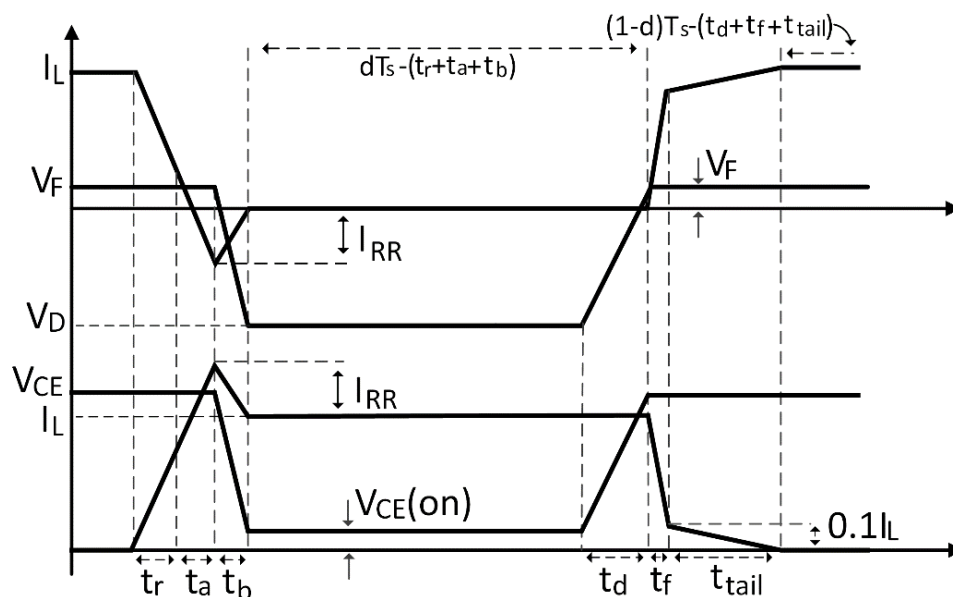


Figure 3.17 Diode and IGBT switching characteristics for loss calculation

The energy losses of an IGBT and a diode can be classified into three categories. These are called as turn-on, turn-off and conduction losses. The turn-on loss of an IGBT and the turn-off loss of a diode depend on the rise time (t_r) and reverse recovery time (t_a, t_b) as seen in (3.11) and (3.12);

$$E_{IGBT_on} = \frac{V_{CE}(I_L + I_{RR})(t_a + t_r)}{2} + \frac{V_{CE}I_{RR}t_b}{3} + \frac{V_{CE}I_Lt_b}{2} + \frac{V_{CE(on)}(3I_L + I_{RR})t_b}{6} \quad (3.11)$$

$$E_{D_off} = \frac{V_F(I_L - I_{RR})(t_a + t_b)}{2} + \frac{(V_D - 2V_F)I_{RR}t_b}{6} \quad (3.12)$$

The turn-off delay time (t_d), fall time (t_f) and tail time (t_{tail}) determine the value of turn-off loss of IGBT and turn-on loss of diode as indicated in (3.13) and (3.14).

$$E_{IGBT_off} = \frac{(V_{CE} + V_{CE(on)})I_Lt_d}{2} + \frac{11V_{CE}I_Lt_f}{20} + \frac{V_{CE}I_Lt_{tail}}{20} \quad (3.13)$$

$$E_{D_on} = \frac{9V_F I_L t_f}{20} + \frac{19V_F I_L t_{tail}}{20} \quad (3.14)$$

The conduction loss depends on the on-state voltage drop ($V_{CE(on)}$), load current, duty cycle (d), and switching period (T_s).

$$E_{IGBT_c} = V_{CE(on)} \cdot I_L (dT_s - (t_r + t_a + t_b)) \quad (3.15)$$

$$E_{D_c} = V_F I_L ((1-d)T_s - (t_d + t_f + t_{tail})) \quad (3.16)$$

The total switching power loss can be calculated for constant switching frequency (f_s) by using (3.17) and (3.18)

$$P_{IGBT_loss} = f_s (E_{IGBT_on} + E_{IGBT_off} + E_{IGBT_c}) \quad (3.17)$$

$$P_{D_loss} = f_s (E_{D_on} + E_{D_off} + E_{D_c}) \quad (3.18)$$

The efficiency of the inverters can be estimated by the help of the equation (3.17) and (3.18). The power loss calculation would be performed by specifying the conduction sequence of the solid state devices over one switching period like in (Xiao

et al., 2011). Since the instantaneous value of load current (I_L) flow through the solid state devices during the switching period, the loss calculation depends on the value of load current. The average value of I_L is used in computation as $I_L = (\frac{2}{\pi})I_m$, here I_m is the peak value of the load current. The value of the duty cycle in (3.15) and (3.16) changes in every switching period therefore its average value is estimated from the relation $d_{av} = (\frac{2}{\pi})m$ (Kolar, Ertl, & Zach, 1991). Here, m is the modulation index. The much more accurate calculation on devices losses could be performed over the one period of grid voltage by taking the instantaneous values of load current and duty cycle. However, the algorithm needs the tabulated values of duty cycle as a function of conduction intervals for devices.

CHAPTER FOUR

DC-DC CONVERTERS FOR MAXIMUM POWER POINT TRACKING

One of the most important renewable energy source is the PV (Hernandez et al, 2011). However, PV plants have two significant problems: the efficiency of the PV panels are very low, and the generated electrical energy by the PV panels depends on many factors, such as temperature, life time of the panels, load conditions and irradiance (Mellit, et al, 2011).

Since PV panels have non-linear voltage-current characteristic, there is a single point where maximum power is produced and this point strictly depends on the irradiance condition and, also depends on the panel temperature. Figure 4.1 shows the voltage-current (I-V) characteristic of the PV panel at different irradiance conditions.

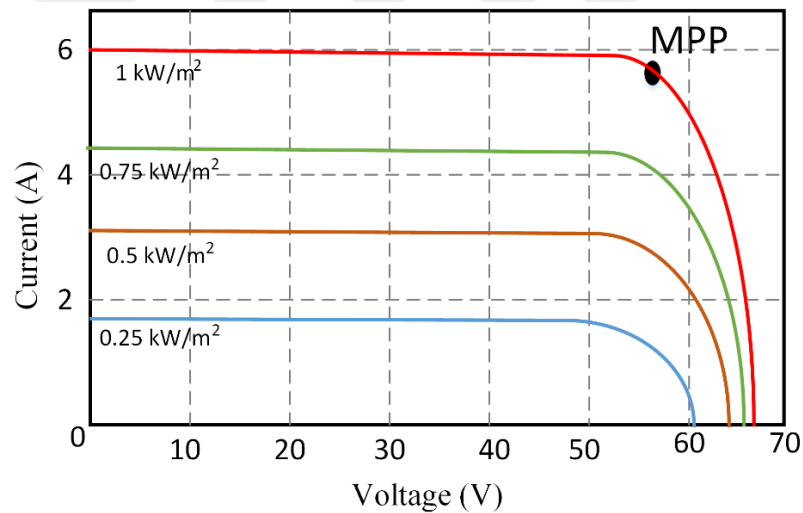


Figure 4.1 Voltage-Current (I-V) characteristic of the PV panel

Because of the impedance mismatch, maximum power point tracking systems (MPPT) are needed in order to get the maximum power from the PV arrays in the photovoltaic application (Morales, et al, 2010). The DC/DC converters with the maximum power point tracking algorithm is used to operate PV module at the maximum power point. These converters interface the PV panels with the loads or grid, and force the operating point of the PV panels at the MPP by changing the apparent impedance of the PV panel to match with the maximum power point impedance value (Taghvaei, et al, 2013).

Different types of the DC/DC converters (Buck, Boost, Buck-Bosst, Cûk, Sepic, etc.) have been used for the MPPT operation. The DC/DC converters used in the maximum power tracking system are compared in (Taghvae, et.all, 2013) in order to determine the best solution for maximum power point system. According to the (Taghvae, et al, 2013), using the buck or boost converter allow achieving maximum power within the limited area although the efficiency of these converters are high. Therefore, boost or buck converter have a tracking problem when the irradiance or temperature are changed. On the other hand, Sepic or Cûk are the ideal convert types for the MPPT system, but number of the reactive component in the circuit topologies and high costs are the main drawbacks of these converters. However, in (Wang, et al, 2014) it stated that, the buck boost converter is the best choice for MPPT operation, since it tracks the maximum power point regardless of the irradiance level, temperature or load conditions.

The MPPT system injects a resistance value to the output of PV panel in order to extract maximum power from it. It means that the input resistance of the DC to DC converter will be equal to the equivalent resistance of PV at maximum power point (R_{MMP}) (Enrique, et al., 2006). The R_{MMP} value can be defined as the value of V_{MPP}/I_{MPP} . The DC/DC converter, used for tracking the MPPT, changes the value of the output load impedance of PV panel by varying the duty cycle. R_L represent the load impedance at the output of DC to DC converter while the R_i represent the value of the load impedance referred to the input terminals (like a transformer) as shown in Figure 4.2.

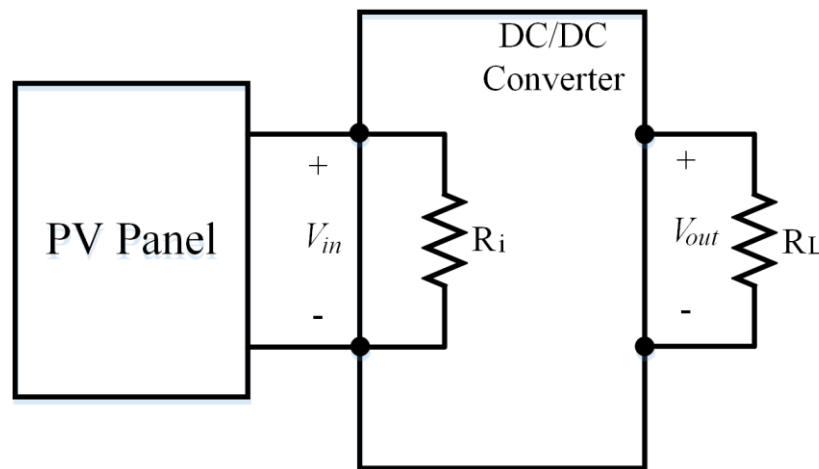


Figure 4.2 DC to DC Converter Connected to the PV Panel

Table 4.1 shows the conversion ratio of input resistance to the load resistance, assuming the continuous conduction mode (CCM) and lossless converter. “d” shows the duty cycle of the converter.

Table 4.1 R_i values for converter types

Converter	R_i (CCM)
Boost	$R_L(1-d)^2$
Buck	R_L/d^2
Boost-Boost	$R_L(1-d)^2/d^2$

Therefore, it can be observed that, the MPP capture region of the converter changes with respect to the converter type (Taghvaei, et al., 2013). If the boost converter is used, the MPP capture is only possible for $R_L \geq R_{MPP}$. Figure 4.3 shows the MPP capture region of the converters.

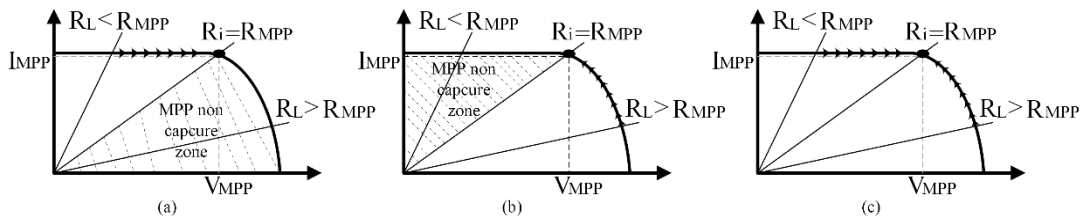


Figure 4.3 Operation regions; a) Buck Converter b) Boost Converter c) Buck-Boost converter

In this thesis, two-switch non-inverting buck boost converter is also used for MPPT operation, because the traditional buck boost converter has negative output voltage according to the input voltage. In addition to that the inverting buck-boost converter is used at the output of PV panel as well because the inverted voltage can be fed to the input of inverter connected to the grid. The analyses of DC to DC converters at continuous current mode (CCM) are given in the following sections.

4.1 Two-Switch Non-Inverting Buck Boost Converter

Two switch buck-boost converter includes two controlled switches (S1-S2), two diodes (D1-D2), one inductor and one capacitor as it can be seen Figure 4.4.

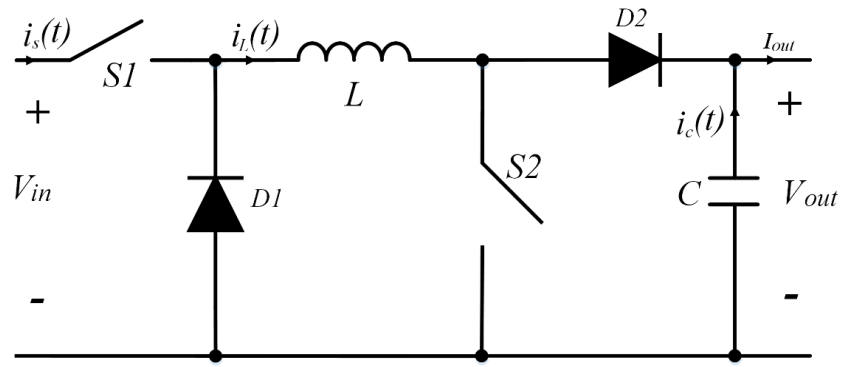


Figure 4.4 Two Switch Non-inverting Buck Boost Converter

It provides positive output voltage with respect to the ground of input voltage. This converter is combination of step up and step down converter. Moreover, two switch non inverting buck boost converter has three operation modes according to the operation modes of the controlled switches (S1-S2). It can be operate buck-boost mode, buck mode or boost mode. If S1 is kept always in conduction state and S2 controlled, the converter operates like a step up converter. Further, if the S2 is always get turn off signals and S1 is switched, this converter operates in buck mode. Moreover, the converter can be operate in buck-boost mode, if the S1 and S2 are controlled simultaneously with same gate signal. The required gate signals according to the used operation mode are shown in Figure 4.5.

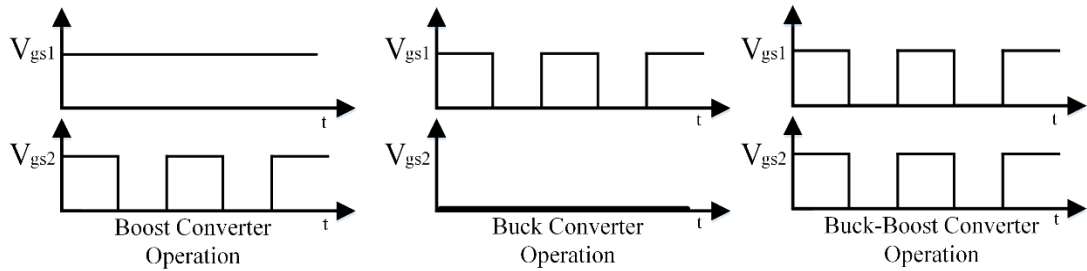


Figure 4.5 Gate Signals for the boost/buck or buck-boost mode operations

The equation of the inductor current in buck mode and boost mode are different. Therefore, the discontinuity occur on the inductor current at the transition between buck mode and boost mode because of the different instantaneous inductor current. On the other hand, the mode transitions are not needed for the buck-boost mode operation. In this thesis, buck-boot mode operation is used in order to eliminate the current distortion on the inductor current.

The relationship between input and output voltages is given in equation (4.1) for the buck-boost mode operation.

$$V_{out} = \frac{V_{in}d}{(1-d)} \quad (4.1)$$

In here, "d" represent the duty cycle. If duty cycle (d) bigger than the 0.5, the converter step up output voltage. If the duty cycle (d) is lower than the 0.5, the converter operates as a step down converter.

The circuit parameters of the converter in buck boost mode can be calculated with the help of Figure 4.6. If the inductor current is in continuous conduction mode as in Figure 4.4, the inductor current can be estimated by using equation (4.2).

$$i_L(t) = I_{L_min} + \int_0^t V_L(t)d(t) \quad (4.2)$$

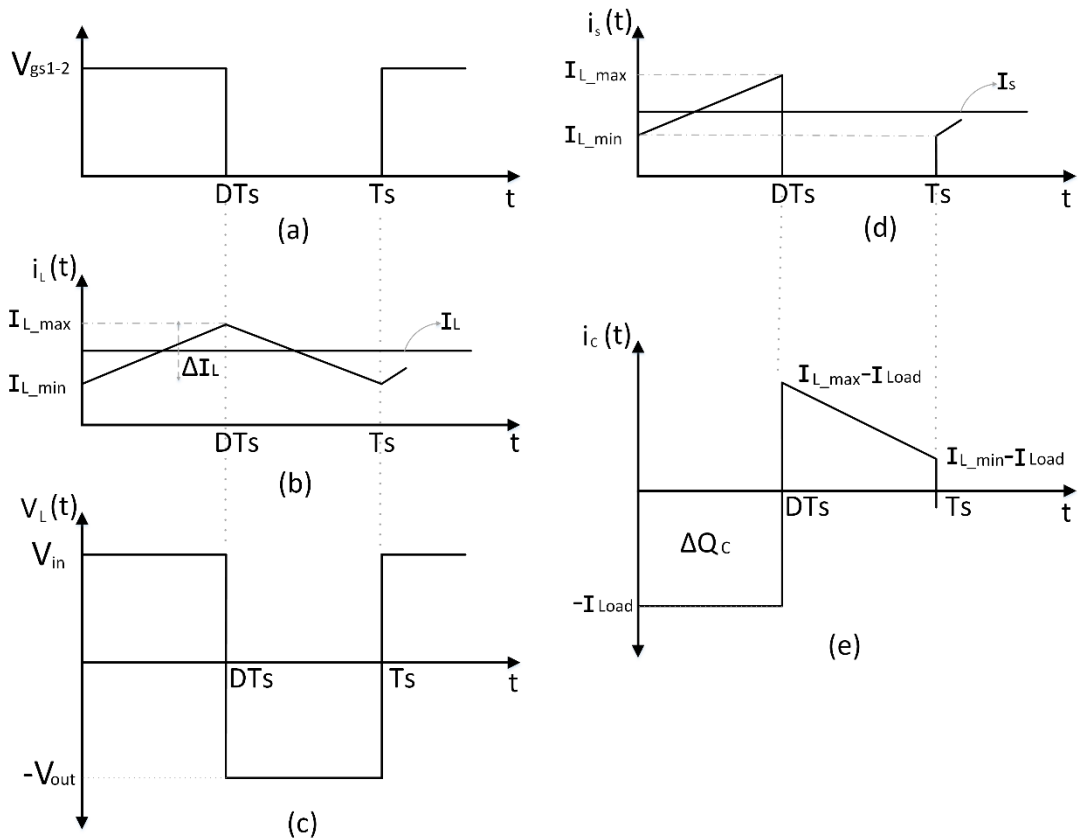


Figure 4.6 (a) Gate Signal, (b) Inductor Current (c) Inductor Voltage (d) Source Current (e) Output Capacitor Current

If $t=dT_s$, $i_L = (dT_s) = I_{max}$. Therefore inductor current is;

$$I_{max} = I_{min} + \frac{V_{in}dT_s}{L} \quad (4.3)$$

Here, the required inductor value for the continuous conduction mode can be computed by using equation (4.4).

$$\Delta I_L = \frac{V_{in}dT_s}{L} \rightarrow L \geq \frac{V_{in}dT_s}{\Delta I_L} \quad (4.4)$$

The maximum and minimum inductor current can be represented as;

$$I_{max} = I_L + \frac{\Delta I_L}{2} = \frac{d^2V_{in}}{R(1-D)^2} + \frac{V_{in}d^2}{2L} \quad (4.5)$$

$$I_{min} = I_L + \frac{\Delta I_L}{2} = \frac{d^2V_{in}}{R(1-d)^2} - \frac{V_{in}d^2}{2L} \quad (4.6)$$

The output capacitance value can be estimated based on the change of charge value,

$$\Delta V_{out} = \frac{\Delta Q}{C} = \frac{I_{Load}dT_s}{C} \rightarrow C \geq \frac{I_{Load}dT_s}{\Delta V_{out}} \quad (4.7)$$

Also, the average source current can be calculated based on average inductor current as follows;

$$I_s = dI_L \quad (4.8)$$

4.2 One-Switch Inverting Buck Boost Converter

One switch buck boost converter provides an output voltage that can be greater or less than the input voltage like two switch buck boost converter (Rashid, 2014). However, the output voltage polarity is opposite of the input voltage in contrast to the two switch buck boost converter.

It include one controlled switch (S1) as the name implies, one diode (D1) and one inductor as shown in Figure 4.7.

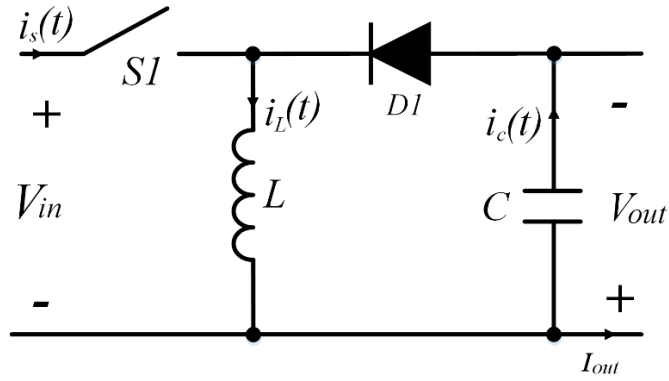


Figure 4.7 Buck-Boost converter topology

The output voltage of the converter can be defined as;

$$V_{out} = \frac{V_{in}d}{(1-d)} \quad (4.9)$$

In here, “d” is defined as duty cycle of the controlled switch. If duty cycle (d) bigger than the 0.5, the converter step up output voltage. If the duty cycle (d) is lower than the 0.5, the converter operates as a step down converter.

The peak to peak inductor ripple current can be defined as given in (4.10) for this converter topology.

$$\Delta I = \frac{V_{in}(-V_{out})}{f_s L(-V_{out}-V_{in})} \quad (4.10)$$

or

$$\Delta I = \frac{V_{in}d}{f_s L} \quad (4.11)$$

where f_s is defined as switching frequency L is the inductor value. Moreover, peak to peak output voltage can be defined like;

$$\Delta V_{out} = \frac{I_{out}d}{f_s C} \quad (4.12)$$

4.3 Boost Converter

The boost converter is the most common used converter for the MPP operation. The output of the boost converter is greater than the input voltage (Rashid, 2014).

One controlled switch (S1) and one un-controlled switched (D1) is used in structure of the boost converter as shown in Figure 4.8. The energy stored in inductor “L”, which included in the structure of the boost converter, transferred to the output.

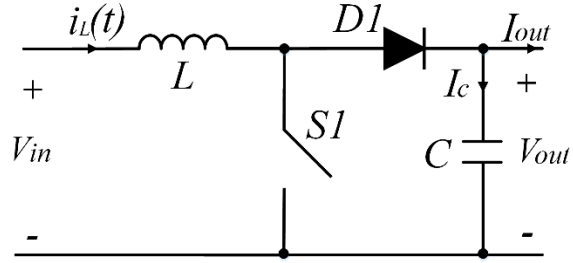


Figure 4.8 Boost Converter Structure

The average output voltage can be defined as;

$$V_{out} = \frac{V_{in}}{(1-d)} \quad (4.13)$$

The peak to peak inductor ripple current can be defined as given in (4.14) for this converter topology.

$$\Delta I = \frac{V_{in}(V_{out}-V_{in})}{f_s L V_{out}} \quad (4.14)$$

or

$$\Delta I = \frac{V_{in}d}{fL} \quad (4.15)$$

where f_s is defined as switching frequency L is the inductor value. Moreover, peak to peak output voltage can be defined like;

$$\Delta V_{out} = \frac{I_{out}d}{f_s C} \quad (4.16)$$

Also, critical value of the inductor and capacitor for the continuous conduction mode can be defined as;

$$L_c = \frac{d(1-d)R}{2f_s} \quad (4.17)$$

$$C_c = \frac{d}{2f_s R} \quad (4.18)$$

CHAPTER FIVE MPPT METHODS

Generally, PV cell characteristic is modelled by the help of single diode or double diode models. Single diode model is used in this thesis, because, it is simple and moderately accurate for the nonlinear characteristic of the PV cell. Figure 5.1 shows the single diode model of the PV cell.

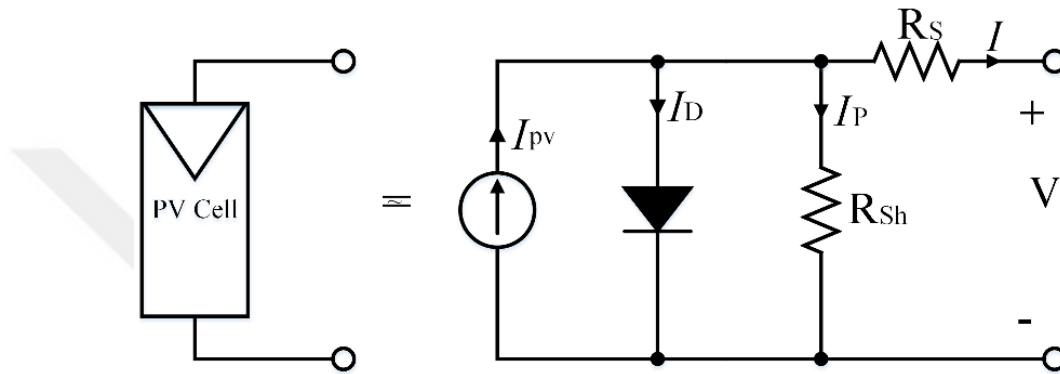


Figure 5.1 PV Cell model

The output current can be determined by using the KCL and given bellow:

$$I = I_{PV} - I_o \left(e^{\frac{q(v+IR_s)}{akT}} - 1 \right) - \frac{V+IR_s}{R_{sh}} \quad (5.1)$$

where, R_s and R_{sh} are series and shunt resistance of the PV cell, I_o is diode saturation current, “a” is ideality factor of diode, “k” is Boltzmann constant (1.3805×10^{-23} J/K), “q” is electron charge (1.6×10^{-19} C) and “T” is the temperature in °C.

Harvesting the maximum power that the solar panel can produce is an important research topic to improve the efficiency of the solar energy system. The dependence of the power generated by the solar panel on factors such as temperature radiation makes it difficult to track the maximum power that can be harvested from the solar panel. In the last decade, many maximum power point tracking (MPPT) algorithms have been developed in order to accurately and rapidly tracking the maximum power generated by the PV module under the changing irradiation and temperature. Most of the MPPT algorithms are compared to each other in (Esrām & Chapman, 2007). Although perturb and observe (P&O) and incremental conductance (INC) are the

most well-known MPPT algorithms, the genetic algorithm, fuzzy logic based algorithm and artificial network based algorithm are some of the recent developed MPPT algorithms that operate under the partially shaded condition (Kakosimos, Kladas & Manias, 2013).

It is important to quickly and accurately set the maximum power point to harvest maximum power from the solar panel under the changing atmospheric condition. P&O algorithm is preferred in many application because of easy of the application, performance. However, P&O algorithm have relatively high response time under changing condition. Also, it cannot converge the true maximum point always. The MPPT algorithms have been combined with digital current controller for the accurately and faster MPPT operation. The combination of the MPPT algorithm with the digital current control methods can be implemented by using the today's powerful and faster microprocessors and digital signal processors (DSPs). Model predictive controller (MPC) is such a controller technique which obtain the control action for both present and future period, and also, it solves the finite horizon optimal control problem at each sampling period (Kakimos, & Kladas, 2011). The MPC has several advantages over the standard control technique such as multivariable case control and easy implementation also, it is expected to improve utilization of the PV system power under the chancing condition by getting over the uncertainties and disturbances.

Perturbation based algorithms such as; perturb and observation (P&O) hill climbing (HC), and conduction based algorithms (incremental conduction (INC), modified incremental conduction (MINC)) are simple, have good speed and accuracy (Ishaqu, et al, 2012). However, these algorithms are not suitable for partial shading conditions and they may not find the global maximum power point. Moreover, these algorithms generate the steady state oscillation around the maximum power point (Danandeh, & Mousavi, 2018). Therefore, the current of the DC to DC converter may have steady state oscillation and operation mode can go into the discontinuous mode. There are several tracking techniques proposed in literature. The methods which are perturb and observation (P&O), and the particle swarm optimization method (PSO) are commonly recommended for the MPPT. The former one tracks the

characteristic continuously while it may arrive the local maximum and oscillate around the MPP, the latter one finds the global maximum with the termination of tracking. The best algorithm is expected to track the characteristic continuously while reaching at the global maximum in any partially shading condition in a shorter time as much as possible.

5.1 Model Predictive Current Controller Based MPPT

In this theses, the model predictive current control technique is combined with the voltage and current oriented P&O algorithm in order to compare the effect of the MPC on the maximum power point tracking operation. The DC/DC boost converter is used with the resistive load for the testing the MPC with the P&O. General structure of the system is shown in Figure 5.2.

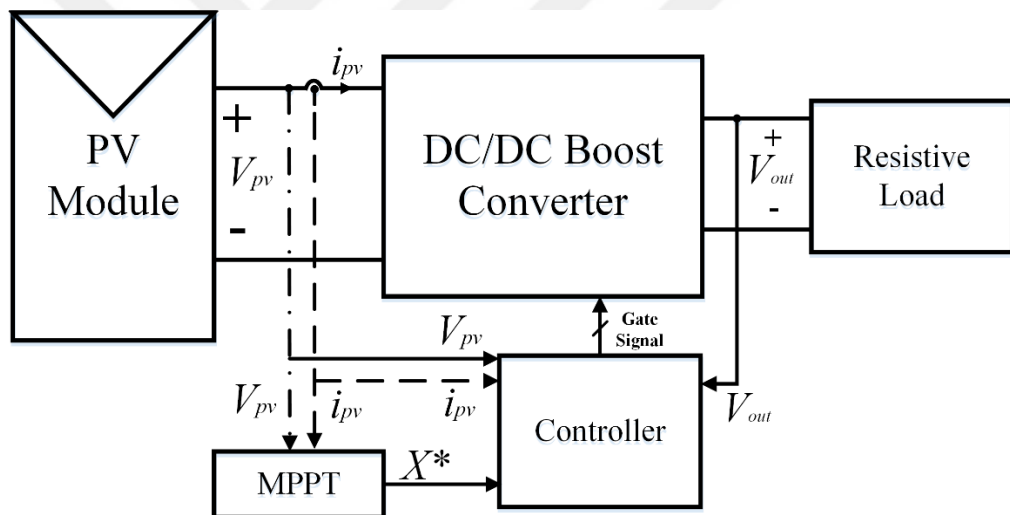


Figure 5.2 General structure of the predictive current controlled system

If the voltage oriented MPPT is used, PI controller must be used in order to convert the voltage reference which generated by the voltage oriented MPPT into the current reference as shown in Figure 5.3.

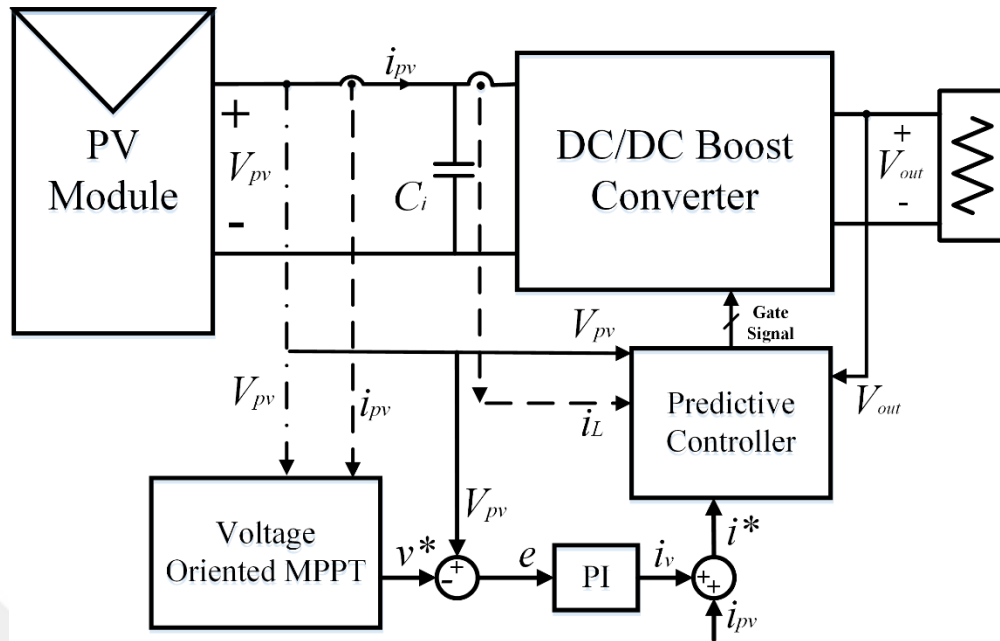


Figure 5.3 System block scheme with PI compensator

The general block scheme of perturb and observe algorithm is given in Figure 5.4. It should be noted that for the voltage oriented MPPT, $x_1: V_{pv}$, $x_2: i_{pv}$ and for the current oriented MPPT $x_1: i_{pv}$, $x_2: V_{pv}$. Moreover, only the voltage oriented P&O algorithm also has been used for the MPPT operation. By this way, effect of the MPC can be seen clearly. In this method, voltage oriented P&O algorithm generate the voltage reference and this reference subtracted by the actual voltage of the PV array and then passed through the PI controller. The output of the PI controller used as gate signal of the converter.

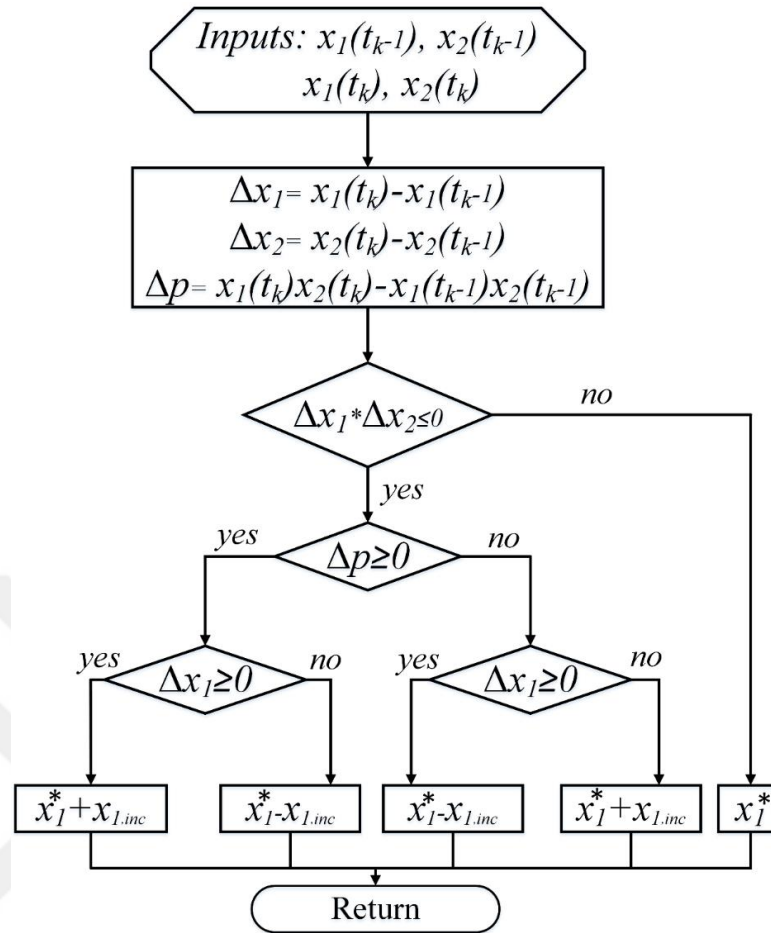


Figure 5.4 Block scheme of P&O algorithm

5.1.1 Model Predictive Current Controlled Boost Converter

The many control techniques have been presented for the power converter system and model predictive control is the one of them. The model predictive control method (MPC) has several advantages which makes it preferable for the power electronic system; nonlinearity and constrains can be employed, it can be easily applied to a variety of the system, and it is intuitive and easily understandable. It requires much more mathematical calculation compared with the conventional technique. However, MPC has become feasible with the development of the powerful microprocessor. The MPC is a control method that uses system state equations to predict the future behavior of the controlled variables.

Two type of the model predictive control method are mentioned in this theses. These are MPC with continuous control set where controller outputs passed through modulator to provide the switch's gate signal and MPC with finite control set (FS

predictive control) that control the state of the converter switches (Cortes et al., 2008). Figure 5.5 shows the specification of these two method.

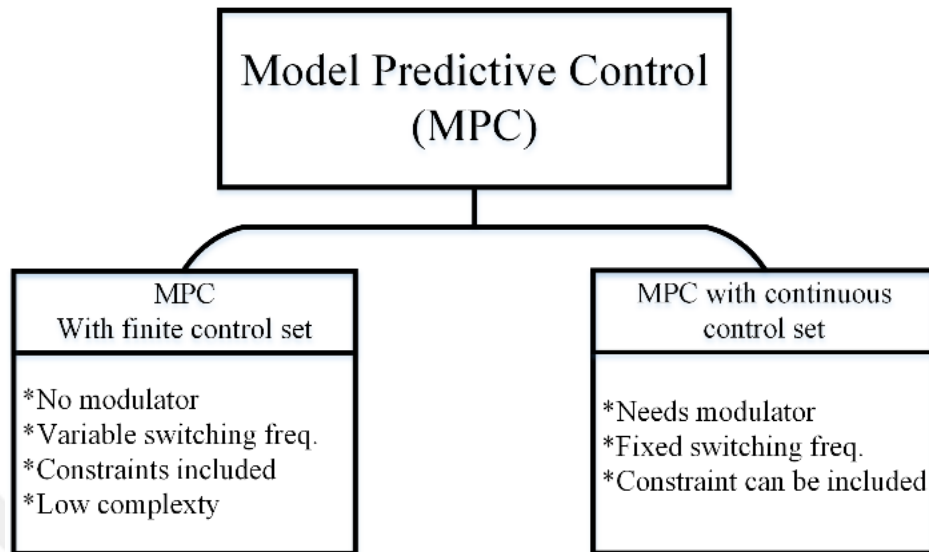


Figure 5.5 Model predictive control methods classifications

The inductor current of the boost converter can be controlled by the MPC. The system state equation for the boost converter can be written according to the switching states to control the inductor current. Boost converter and switching states are shown in Figure 5.6. The switch S1 is closed in Figure 5.6 (a) and the switch S1 is open in Figure 5.6 (b).

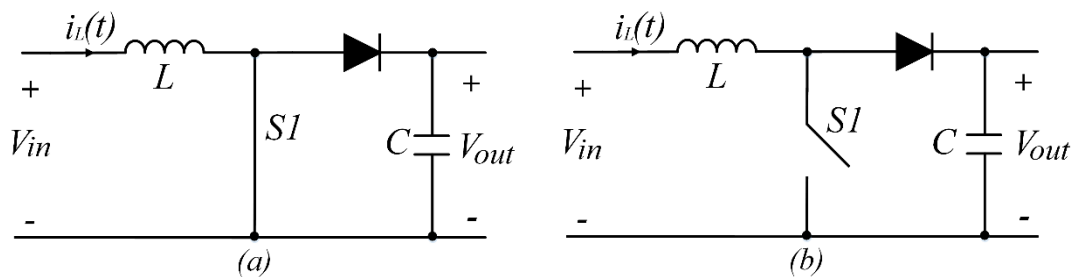


Figure 5.6 Boost converter switching state a) Switch closed b) Switch open

The inductor voltage can be written with respect to the switch state;

If the switch is closed;

$$L \frac{di_L}{dt} = V_{in} \quad (5.2)$$

If the switch is open;

$$L \frac{di_L}{dt} = V_{in} - V_{out} \quad (5.3)$$

The discrete time of the equation (5.2) and (5.3) are as follows;

$$i_L[n+1] - i[n] = \frac{T_s}{L} V_{in}[n] \quad (5.4)$$

$$i_L[n+1] - i[n] = \frac{T_s}{L} [V_{in}[n] - V_{out}[n]] \quad (5.5)$$

and the combination of inductor current can be expressed;

$$i_L[n+1] - i[n] = \frac{T_s}{L} [V_{in}[n] - u'[n+1]V_{out}[n]] \quad (5.6)$$

where the $u' = 1 - u$ represent the switching state (Logic 1 and 0). The predicted state variable shown as $i_L[n+1]$ while the current sampled value shown as $i_L[n]$ and T_s represent the sample time. And now the control variable (i_L) can be predicted next sampling time based on the cost function for the FS-MPC method. The cost function is the key factor for the FS-MPC technique. The cost function of the boost converter expressed as;

$$J = \min |i_L[n+1] - i_L^*| \quad (5.7)$$

and here i_L^* represent the reference inductor value. The next switching state can be determined according to the cost function. The FS-MPC does not require the modulator, it determines the switch state for the next switching cycle due to the cost function. For this reason, the switching frequency may change and rise to the sampling frequency. In the application, the sampling frequency depends on the analog to digital converter module of the microprocessor. This method can be extended more than one prediction step with increasing the robustness, as well as computational effort.

The MPC with continuous control set method needs modulator and it can control the valley, peak or average value of the inductor current of the boost converter

according to the modulator type (Chen, et al., 2003). The modulator types are shown in Figure 5.7.

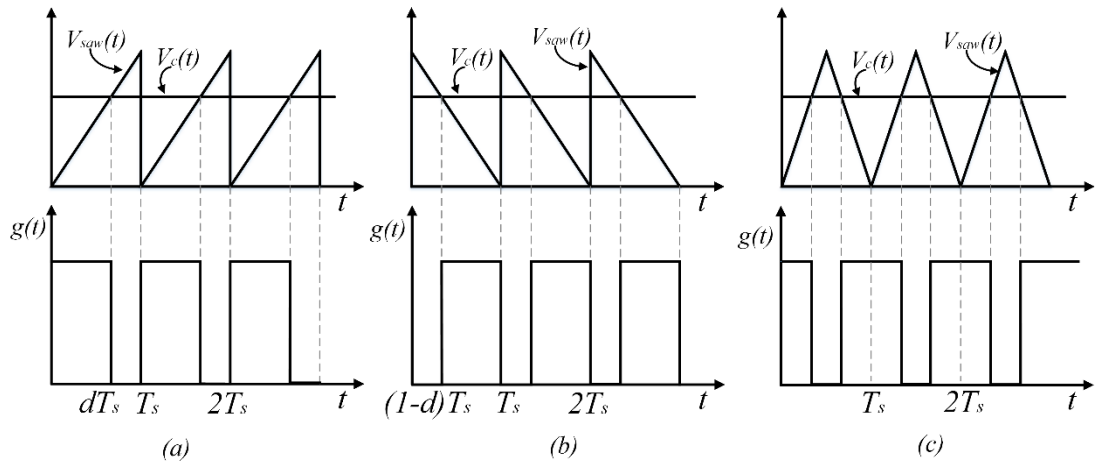


Figure 5.7. Modulation methods. a) Trailing edge modulation b) Leading edge modulation c) Trailing triangle modulation

Valley inductor current can be controlled by using the trailing edge modulation, since sampled inductor current each switching period is the valley inductor current. The equation of inductance current can be written by using the Figure 5.8 which shows the inductor current wave form under the trailing edge modulation.

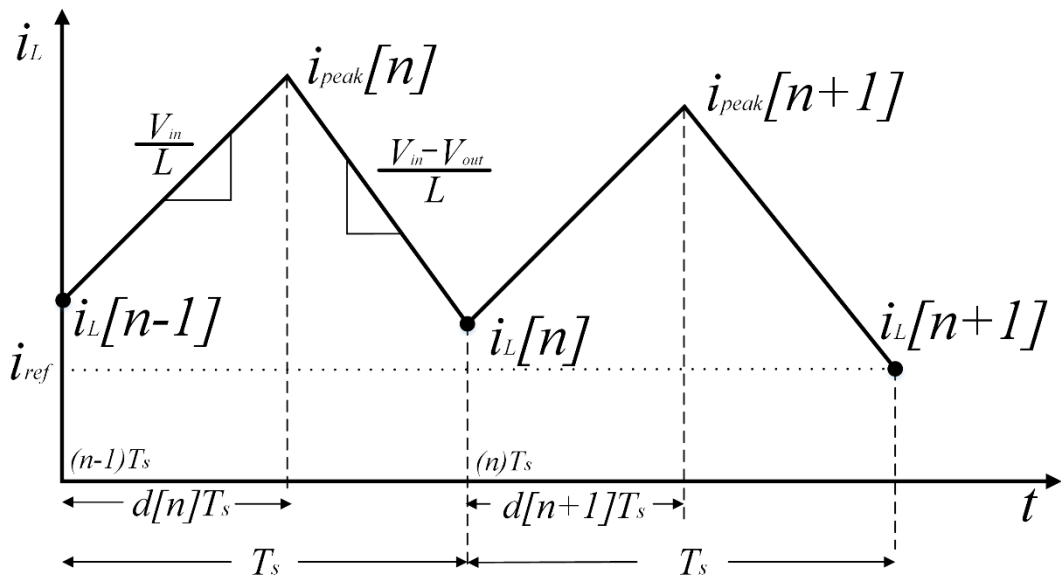


Figure 5.8 Inductor current

The required duty cycle can be predicted for the next switching period based on the sampled inductor current and possibly the input and output voltage. The input

and output voltage can be considered constant during the switching period, because they are slowly changing signals.

One step horizon inductor current can expressed as;

$$i_L[n] = i_L[n - 1] + \frac{V_{in}d[d]T_s}{L} + \frac{(V_{in}-V_{out})d'[n]T_s}{L} \quad (5.8)$$

Where $d'[n]=1-d[n]$ and substituting in (5.2), the inductance equation is;

$$i_L[n] = i_L[n - 1] + \frac{V_{in}T_s}{L} - \frac{(V_{out})d'[n]T_s}{L} \quad (5.9)$$

Equation (5.3) can be extended for another switching period (two step horizon extension);

$$i_L[n + 1] = i_L[n - 1] + \frac{2V_{in}T_s}{L} - \frac{(V_{out})d'[n]T_s}{L} - \frac{(V_{out})d'[n+1]T_s}{L} \quad (5.10)$$

Equation (5.10) can be solved for the predicted duty cycle that is used for following to reference current;

$$d[n + 1] = 2 - d[n] - \frac{L}{V_{out}-T_s} (i_L[n - 1] - i_{ref}) - \frac{2V_{in}}{V_{out}} \quad (5.11)$$

The one step horizon extension (equation 5.9) or the two step horizon extension expression (equation 5.11) of the inductor current can be used for the valley current control. However, these equation can be used for the average and peak current control by changing the modulation technique. The key point of the changing the modulation technique is to enable sampling of the targeted current of interest (peak, average, valley) at equally interval which equals to the switching period. Such as; if the leading edge modulation technique is used the peak inductor current is sampled at beginning of the switching period. Moreover, if the trailing triangle modulation is used, the average inductor current is sampled at the beginning of the switching period. Table 5.1 shows the controlled current with respect to the modulation technique.

Table 5.1 Controlled Current according to the modulation technique

	Modulation Technique	Controlled Current
Equation (5.8) or Equation (5.10)	Trailing Edge	Valley Current
	Leading Edge	Peak Current
	Trailing triangle	Average Current

Average current may also be controlled by using the trailing edge modulation method, if one period average of the inductor current is taken. Single the period of inductor current can be divided into two parts in order to calculate the average value. $f_1(t)$ define the rising side of the inductor current (switch is in conduction mode $0 < t < d[n+1]T_s$) and expressed as; $f_1(t)=a_1t+b_1$, and $f_2(t)$ is the falling side of the inductor current (switch do not conduction mode $d[n+1]T_s < t < T_s$) expressed as; $f_2(t)=a_2t+b_2$ and shown in Figure 5.9.

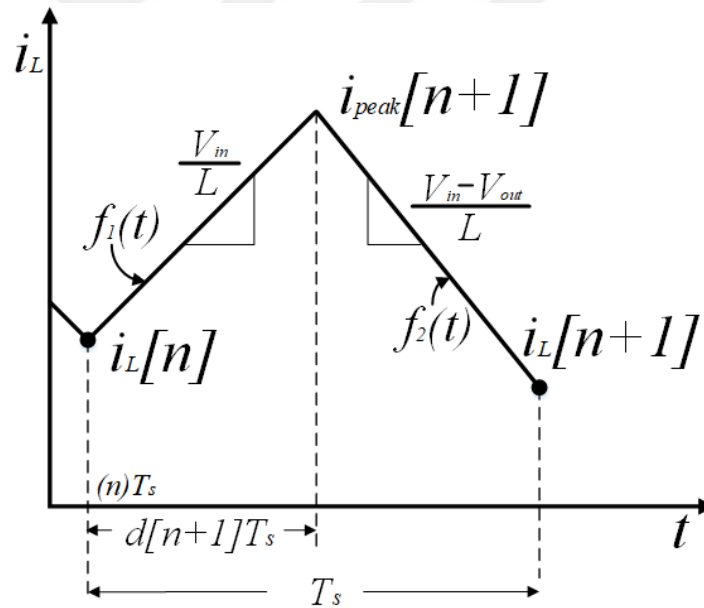


Figure 5.9 One switching period

The general definition of the average value for a periodic signal can be used here. If the function of periodic wave is $f_k(t)=a_kt+b_k$ then the average of the $f_k(t)$ can be expressed as ; $\langle f_k(t) \rangle = \frac{1}{T_s} \int_0^{T_s} f_k(t) dt$,

The average inductor current can be found as follows;

$$\langle i_L(t) \rangle = \frac{1}{T_s} \int_0^{T_s} (f_1(t) + f_2(t)) dt = (a_1 - a_2) \frac{d[n+1]^2 T_s}{2} + b_1 d[n+1] + b_2 - b_2 d[n+1] + \frac{a T_s}{2} \quad (5.12)$$

where;

$a_1 = \frac{V_{in}}{L}$, $a_2 = \frac{V_{in} - V_{out}}{L}$, $b_1 = i[n]$, and $b_2 = i[n] + \frac{V_{out} d[n+1] T_s}{L}$. If these variable substitutes in (5.12), we get;

$$\langle i_{ref} \rangle = i[n] + \frac{V_{in} T_s}{2L} - \frac{V_{out} d[n+1]^2 T_s}{2L} \quad (5.13)$$

If the next duty cycle ($d[n+1]$) is the target to be estimated, the equation (5.7) gives a nonlinear expression. This math operation is difficult to process for the microcontrollers. Therefore, this equation must be linearized and following equation is used for linearization operation;

$$i_L[n+1] = i[n] + \frac{V_{in} T_s}{L} - \frac{V_{out} d'[n+1] T_s}{L} \quad (5.14)$$

$$d = \left(1 - \frac{V_{in}}{V_{out}} \right) \quad (5.15)$$

Where (5.14) represents the valley current after the one switching period, equation (5.15) is the ideal steady state duty cycle for the boost converter for the continuous conduction mode. By substituting the (5.14) and (5.15) in equation (5.16) the linear average current expression can be obtained as follows;

$$i_{ref} = i[n] - \frac{V_{out} T_s}{L} + \frac{V_{in} d[n+1] T_s}{L} + \frac{V_{in} T_s}{L} \left(\frac{3}{2} - \frac{V_{in}}{2V_{out}} \right) \quad (5.16)$$

Then, equation (5.16) is solved for the next step duty cycle as follows;

$$d[n+1] = 1 - \frac{V_{in}}{2V_{out}} \left(3 - \frac{V_{in}}{V_{out}} \right) + \frac{L}{V_{out} T_s} (i_{ref} - i[n]) \quad (5.17)$$

Now, the average current can be controlled by using the equation (5.17) under the trailing edge modulation.

Model predictive current control can be applied for controlling the inductance current of the other DC/DC converters such as; buck-boost, buck converter. Figure 5.10 shows the general inductance wave form in continuous conduction mode for the switching converters under the trailing edge modulation. When the switch is conducting, the inductor current rises with a slope m_1 , then decreases with a slope $-m_2$ (Chen et al, 2003). Therefore, the general predictive control law equation can be defined based on slopes m_1 , $-m_2$, switching frequency, and previous duty cycle as;

$$d[n+1] = -d[n] - \frac{1}{(m_1 + m_2)T_s} [i[n-1] - i_{ref}] + \frac{2m_2}{m_1 + m_2} \quad (5.18)$$

The slopes are given in Table 5.2 for the basic DC/DC converters.

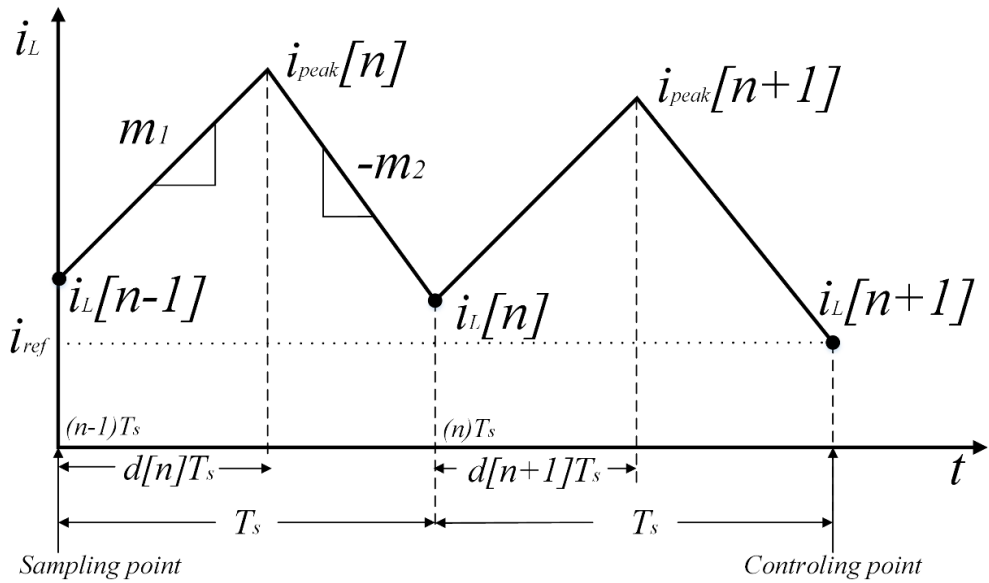


Figure 5.10 General wave form of the inductor current

Table 5.2 Slopes of the inductance of the basic converters

Boost Converter	$m_1 = \frac{V_{in}}{L}$	$-m_2 = \frac{V_{in}-V_{out}}{L}$
Buck Converter	$m_1 = \frac{V_{in}-V_{out}}{L}$	$-m_2 = \frac{-V_{out}}{L}$
Buck-Boost Converter	$m_1 = \frac{V_{in}}{L}$	$-m_2 = \frac{V_{out}}{L}$

5.2 Model of Digital PI Controller

Transfer function of the PI controller, used in the MPPT algorithm loop, can be defined as in equation (5.19) by using trapezoidal integration rule (Gurbuz, 1997; Gurbuz et.al., 1998a, 1998b, 2002).

$$K_p + K_i \frac{T(z+1)}{2(z-1)} \quad (5.19)$$

Where K_p is proportional constant, K_i is the integral constant, and T is the sampling period.

Block diagram of the PI controller is given in Figure 5.11.

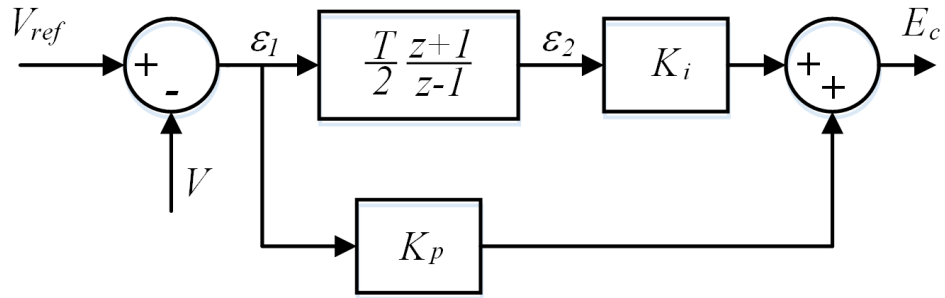


Figure 5.11 Block diagram of the PI controller

The error is the difference between reference and actual values,

$$\varepsilon_1 = V_{ref} - V \quad (5.20)$$

$$\varepsilon_2(z) = \frac{T(z+1)}{2(z-1)} \varepsilon_1 \quad (5.21)$$

Let us define;

$$\varepsilon_1(n+1) = V_{ref}(n) - V(n) \quad (5.22)$$

The discrete form of (5.21) is

$$2\varepsilon_2(n+1) - 2\varepsilon_2(n) = T\varepsilon_1(n+1) + T\varepsilon_1(n) \quad (5.23)$$

Substituting equation (5.22) into the equation (5.23) and rearranged in the state-space form given in bellow,

$$\begin{pmatrix} \varepsilon_1 \\ \varepsilon_2 \end{pmatrix}_{n+1} = \begin{pmatrix} 0 & 0 \\ T/2 & 1 \end{pmatrix} \begin{pmatrix} \varepsilon_1 \\ \varepsilon_2 \end{pmatrix}_n + \begin{pmatrix} 1 & -1 \\ T/2 & -T/2 \end{pmatrix} \begin{pmatrix} V_{ref} \\ V \end{pmatrix}_n \quad (5.24)$$

The output of the PI controller is defined as

$$E_c(n+1) = (K_p \quad K_i) \begin{pmatrix} \varepsilon_1 \\ \varepsilon_2 \end{pmatrix}_{n+1} \quad (5.25)$$

The equation (5.24) is substituted into the (5.25) as follows;

$$E_c(n+1) = (K_p \quad K_i) \left\{ \begin{pmatrix} 0 & 0 \\ T/2 & 1 \end{pmatrix} \begin{pmatrix} \varepsilon_1 \\ \varepsilon_2 \end{pmatrix}_n + \begin{pmatrix} 1 & -1 \\ T/2 & -T/2 \end{pmatrix} \begin{pmatrix} V_{ref} \\ V \end{pmatrix}_n \right\} \quad (5.26)$$

Then $\begin{pmatrix} \varepsilon_1 \\ \varepsilon_2 \end{pmatrix}_n$ term in the equation (5.26) can be expanded in terms of previous sample time and it gives,

$$E_c(n+1) = (K_p \quad K_i) \left\{ \begin{pmatrix} 0 & 0 \\ T/2 & 1 \end{pmatrix} \left\{ \begin{pmatrix} 0 & 0 \\ T/2 & 1 \end{pmatrix} \begin{pmatrix} \varepsilon_1 \\ \varepsilon_2 \end{pmatrix}_{n-1} + \begin{pmatrix} 1 & -1 \\ T/2 & -T/2 \end{pmatrix} \begin{pmatrix} V_{ref} \\ V \end{pmatrix}_{n-1} \right\} + \begin{pmatrix} 1 & -1 \\ T/2 & -T/2 \end{pmatrix} \begin{pmatrix} V_{ref} \\ V \end{pmatrix}_n \right\} \quad (5.27)$$

Then, $\begin{pmatrix} 0 & 0 \\ T/2 & 1 \end{pmatrix}$ term in equation (5.27) is re-defined as a summation of two matrices $\left(\begin{pmatrix} 0 & 0 \\ T/2 & 1 \end{pmatrix} = \begin{pmatrix} 1 & 0 \\ 0 & 1 \end{pmatrix} + \begin{pmatrix} -1 & 0 \\ T/2 & 0 \end{pmatrix} \right)$ and substituted into the equation, hence it yields,

$$E_c(n+1) = E_c(n) + (K_p \quad K_i) \begin{pmatrix} -1 & 0 \\ T/2 & 0 \end{pmatrix} \left\{ \begin{pmatrix} 0 & 0 \\ T/2 & 1 \end{pmatrix} \begin{pmatrix} \varepsilon_1 \\ \varepsilon_2 \end{pmatrix}_{n-1} + \begin{pmatrix} 1 & -1 \\ T/2 & -T/2 \end{pmatrix} \begin{pmatrix} V_{ref} \\ V \end{pmatrix}_{n-1} \right\} + (K_p \quad K_i) \begin{pmatrix} 1 & -1 \\ T/2 & -T/2 \end{pmatrix} \begin{pmatrix} V_{ref} \\ V \end{pmatrix}_n \quad (5.28)$$

Hence,

$$\Delta E_c = (K_p \quad K_i) \begin{pmatrix} -1 & 0 \\ T/2 & 0 \end{pmatrix} \left\{ \begin{pmatrix} 0 & 0 \\ T/2 & 1 \end{pmatrix} \begin{pmatrix} \varepsilon_1 \\ \varepsilon_2 \end{pmatrix}_{n-1} + \begin{pmatrix} 1 & -1 \\ T/2 & -T/2 \end{pmatrix} \begin{pmatrix} V_{ref} \\ V \end{pmatrix}_{n-1} \right\} + (K_p \quad K_i) \begin{pmatrix} 1 & -1 \\ T/2 & -T/2 \end{pmatrix} \begin{pmatrix} V_{ref} \\ V \end{pmatrix}_n \quad (5.29)$$

And then it gives;

$$\Delta E_c = \left(-K_p + K_i \frac{T}{2}\right) (V_{ref} - V)_{n-1} + \left(K_p + K_i \frac{T}{2}\right) V_{ref}(n) + \left(-K_p - K_i \frac{T}{2}\right) V(n) \quad (5.30)$$

Hence,

$$\Delta E_c = K_p(\varepsilon_1(n) - \varepsilon_1(n-1)) + TK_i(\varepsilon_1(n)) \quad (5.31)$$

where, $\varepsilon_1(n) \approx \frac{\varepsilon_1(n) + \varepsilon_1(n-1)}{2}$.

V_{ref} is the voltage references of the PV module, which is generated by the P&O algorithm and, "V" is the sampled actual PV voltage. Also equation 5.31 can be defines as;

$$E_c(n+1) = E_c(n) + K_p(\varepsilon_1(n) - \varepsilon_1(n-1)) + K_i \frac{T}{2}(\varepsilon_1(n) + \varepsilon_1(n-1)) \quad (5.32)$$

5.3 MPPT with Particle Swarm Optimization

Eberhard and Kennedy developed the particle swarm algorithm in 1995. They got inspired by the social behavior of the bird flocking and fish schooling. The PSO is the simple and effective optimization that can be applied to the problems on where a point or n-dimensional space functions to find the best solution.

In this algorithm, several cooperative agents, which are named as particle, are used and they are considered as a candidate of the solution. These agents moves in the search space and this movement determined by the best experience of the neighbor agents and its own best experience. The velocity of the particle (v_i^k) can be defined as;

$$v_i^{k+1} = w^{k+1}v_i^k + c_1^{k+1}r_1\{p_{best,i} - x_i^k\} + c_2^{k+1}r_2\{g_{best} - x_i^k\} \quad (5.33)$$

Where w is the inertia weight, c_1 and c_2 are acceleration coefficients, r_1 and r_2 normalized random number ($r_1, r_2 \in U(0,1)$), $p_{best,i}$ best position of the particle 'i' and g_{best} is the best position of the particles in the entire population. New position of the particle at k^{th} iteration can be found by using equation 5.34.

$$x_i^{k+1} = x_i^k + v_i^{k+1} \quad (5.34)$$

Flowchart of the PSO method for the MPPT system is given in Figure 5.12. Here, the particles are used as duty cycle of the power semi-conductor of the MPPT converter and trying to find the best particle tat extract the maximum power from the PV panel.

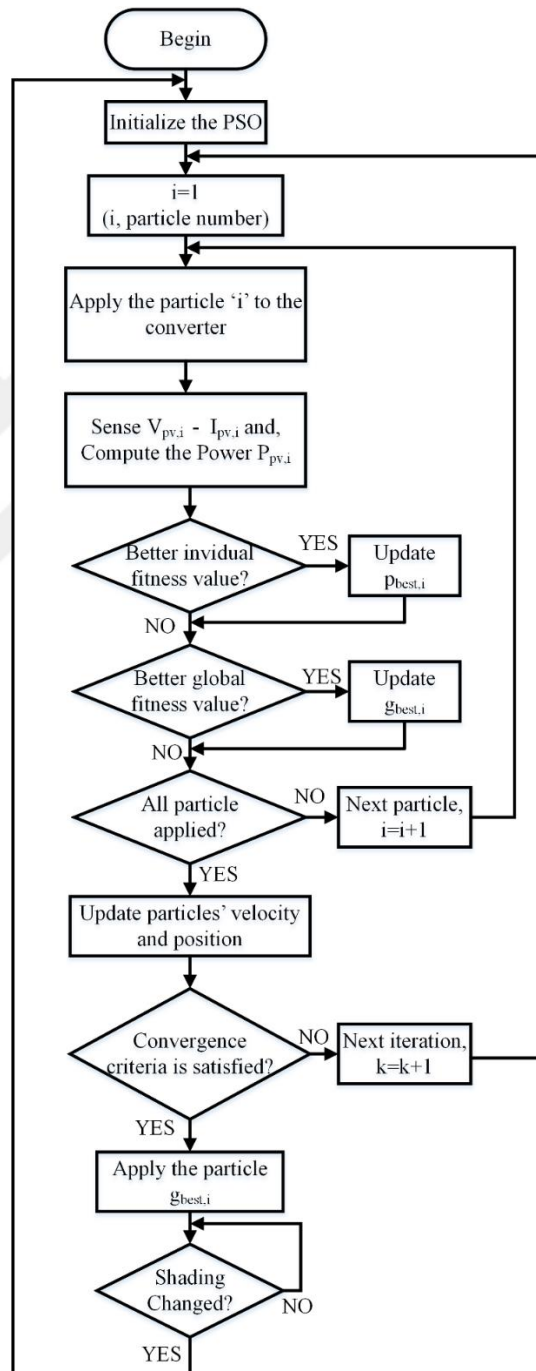


Figure 5.12 Flowchart of the PSO method

In the first block (Initialization of PSO), the upper - lower limits are defined, convergence criteria are selected and initial position of particles are determined. In this application, these particles are selected as a duty cycle (d) of the dc-dc converter. The particles can be evenly spaced distributed on whole search space ($d_{\max} - d_{\min}$). The d_{\max} and d_{\min} represent the maximum and minimum duty cycle of the converter respectively. Particle numbers can be chosen as the number of the series connected cells (Lui et al., 2012). Large number of the particle cause the long computational time but, it can cause more accurate MPPT.

The second part can be defined as fitness evaluation. In this step, all particles are applied on the converter respectively and then related power (fitness value of particle 'i') of the PV module computed by using the V_{pv} and I_{pv} . After that, the best position of the particle ($p_{\text{best},i}$) is determined by the comparing the individual best position of particle in history. Moreover, globally best particle (g_{best}) is updated according to the new power values.

After all fitness values are computed, the velocity and position of the particle should be updated by using equation (5.33) and (5.34). In conventional PSO algorithm, w , c_1 and c_2 are selected constant. If these parameters are set as the variables, the convergence time can be speed up (Lui et al., 2012). The first term (wv_i^k) of the equation (5.33) controls the convergence characteristic of the PSO. To speed up the convergence time, inertia weight can be defined linearly decreasing as shown in equations (5.35) where w_{\max} and w_{\min} show the maximum and minimum limits of the inertia weight, and k represents the iteration number. Then, the social and cognitive parameters can be selected as varying like inertia weight. These parameters determine the search ability of the particle by biasing the position of the particle. If $c_1 > c_2$, particle biasing toward the position of the $p_{\text{best},i}$. On the other hand, if $c_2 > c_1$, particle moves toward the g_{best} and this is the favored behavior for the particle. Therefore, c_1 and c_2 are updated by using equation (5.36) and (5.37).

$$w^{k+1} = w_{\max} - \frac{k}{k_{\max}} (w_{\max} - w_{\min}) \quad (5.35)$$

$$c_1^{k+1} = c_{1,\max} - \frac{k}{k_{\max}} (c_{1,\max} - c_{1,\min}) \quad (5.36)$$

$$c_2^{k+1} = c_{2,max} + \frac{k}{k_{max}}(c_{2,max} - c_{2,min}) \quad (5.37)$$

Different convergence criteria can be defined for PSO, it depends on system design. The velocity of all particle can be the convergence criteria, the variation on the fitness value can become also convergence criteria and also maximum iteration number can be a convergence criteria. Final step of the algorithm defined as re-initialization step. The conventional PSO algorithm designed for the time invariant problem solution but in the MPPT application, the global maximum changes with environment and also with loading conditions. Therefore, the particles have to be re-initialized to find new MPP when the environmental and loading conditions change. The following equation (5.38) is used to detect changing of the MPP. If this equation is satisfied, the particles are re-initialized (Miyatake, & Veerachary, 2011).

$$\frac{|P_{pv,new} - P_{pv,last}|}{P_{pv,last}} \geq \Delta P(\%) \quad (5.38)$$

where $P_{pv,last}$ shows the MPP of the last operating point, and $P_{pv,new}$ represent the new calculated power.

The execution time of the PSO algorithm for reaching at the global MPP is longer than that of the simple P&O algorithm and other conventional MPPT algorithms. Therefore, the initial positions of the particle has the critical role on the execution time. To find the global MPP faster than the standard PSO algorithm, some improvements have been done in literature (Lian et al., 2014). The PSO algorithm with P&O method are also used together to speed up the execution. In order to determine the local maximum faster, the P&O algorithm can be employed, then, the PSO algorithm takes over the process to find the global maximum. Another study in the literature has suggested the lagrangian interpolation method to find the approximate maximum power point voltage and then the initial position of the particles around this position is selected to speed up the process (Koad et al., 2017).

In this thesis, conventional PSO algorithm is used in order to investigate the effect of method on the steady-state oscillations around the MPP and it is compared to the PO method.

CHAPTER SIX

SIMULATION AND EXPERIMENTAL RESULTS

6.1 Single Phase Photovoltaic Inverters Results

The simulations and experiments have been carried out for the single phase transformerless inverters mentioned in chapter three. Simulations have been done using the MATLAB/Simulink and experiments have also been done in Power Quality Laboratory at Dokuz Eylul University.

Experiments have been done under the constant DC link voltage (not used the PV modules or PV simulators). The simulation results of grid connected inverter has been simulated under the constant DC link voltage and compared to experimental results. The complete system including PV module and DC to DC converter has been analyzed and simulated in Matlab. Figure 6.1 shows the simulation model for constant DC link voltage. The inverter model has been arranged for appropriate inverter topology used in the system and the circuit parameters are given in Table 6.1. The required gate signals have been generated with the help of proportional resonant (PR) controller that is used for grid connection (Hafezi et al., 2014a, 2014b; Balikci, Akpinar & Durbaba, 2017).

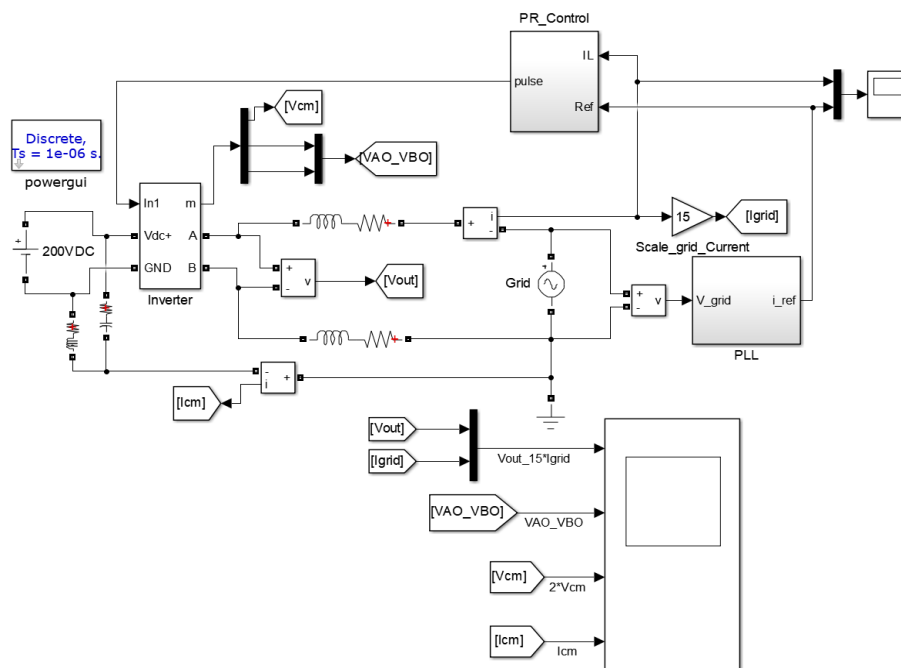


Figure 6.1 Simulation model for constant DC link voltage condition

Figure 6.2 shows the simulation model for the grid connected inverters with PV modules and two-switch buck boost converter and Figure 6.3 shows the characteristics of the used PV module used in simulation. In this model, two-switch buck boost converter is connected to the input of inverter and the input capacitance of the buck boost converter is selected at the value of 500uF. Moreover 100nF leakage (parasitic) capacitors are connected between the ground and positive, and the ground and negative terminals of the input of inverter during all simulations and experiment study.

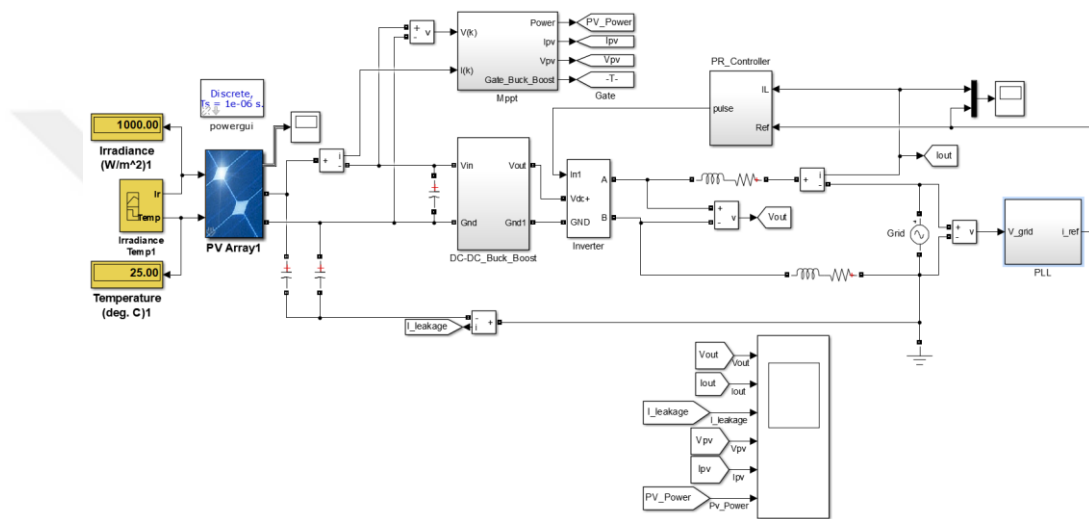


Figure 6.2 Simulation model for the grid connected PV system

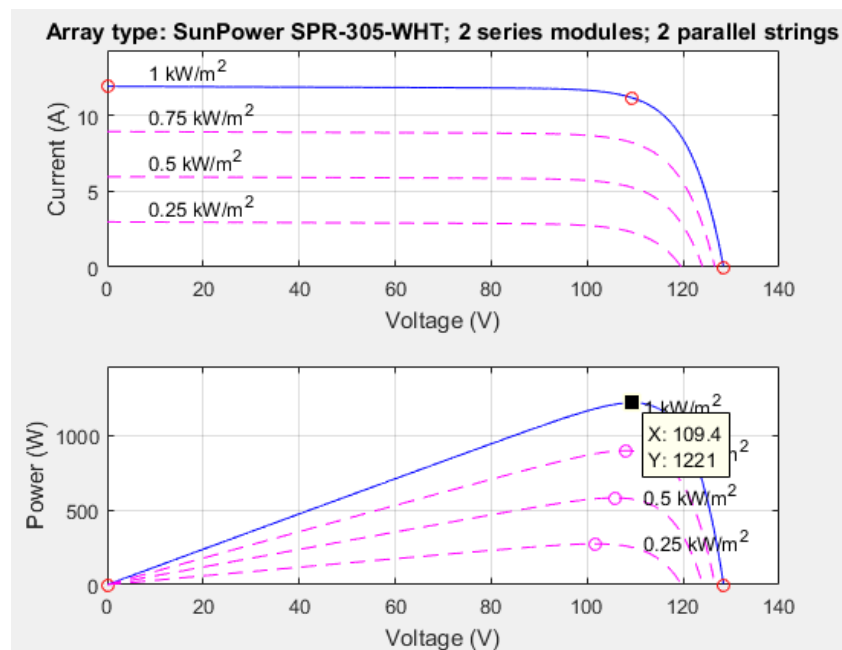


Figure 6.3 PV characteristic

The experimental and simulation results have been obtained for the proposed and oH5 topologies connected to the grid. The grid connected H6 topology has been analyzed and simulated only since the gate driver module used in the laboratory is not compatible with the switching logic given in the circuit. However, this topology is tested experimentally as an inverter (not connected to the grid) feeding power to RL load for the comparison of the efficiency results estimated from the method given in chapter three (Balıkcı, et al., 2017). On the other hand, the improved H6 topology was tested only experimentally because the internal capacitor of the switching devices are not considered in MATLAB/Simulink.

Table 6.1 Parameters of the grid connected inverters

Symbol	PARAMETER	Value
V_g	Grid voltage	110V RMS
f	Grid frequency	50 Hz.
V_{dc}	DC Bus voltage	200V
C_{dc}	DC Bus capacitor (each)	10000 μ F
L_f	Line filter inductance	3,6mH
S_1 - S_7	IGBT	SKM75GB123D
f_{sw}	Switching frequency	10kHz.
C_p	PV parasitic capacitance	100 nF

A prototype has been used in laboratory to test the grid connected inverter topologies. The common mode voltage, the leakage ground current and the efficiency under standard unipolar switching condition have been investigated. The circuit with 1 kW of power capacity has connected to the grid and tested. The system parameters used in the analysis of the proposed topology are given in Table 6.1 and Figure 6.4 shows the experimental setup.



Figure 6.4 Experimental setup (Personal archive, 2018)

6.1.1 Proposed Topology

Figure 6.5 shows the simulation result under the constant DC-link voltage for the proposed converter (Figure 3.13). It can be seen that the common mode voltage is constant and leakage current under 300mA when unipolar output voltage is generated.

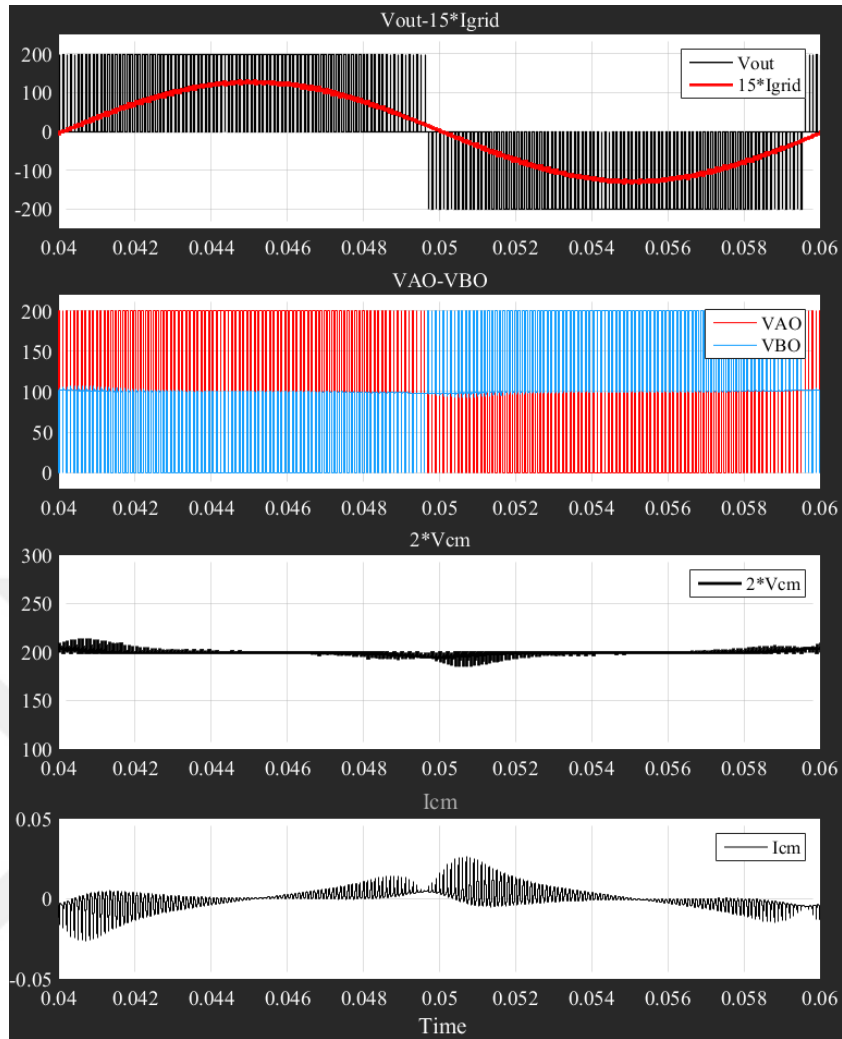


Figure 6.5 Simulation results under the constant DC link voltage for proposed topology

The simulation result for the grid connected PV system is given in Figure 6.6. In this model PV module and two-switch buck boost converter are used. Perturb and observe algorithm (duty cycle of the DC/DC converter is arranged) is used for MPPT operation. Also, 450uF capacitor have been used as a DC link capacitor. The leakage current is lower than the 400mA and PV module supply the maximum power while inverter works with unity power factor.

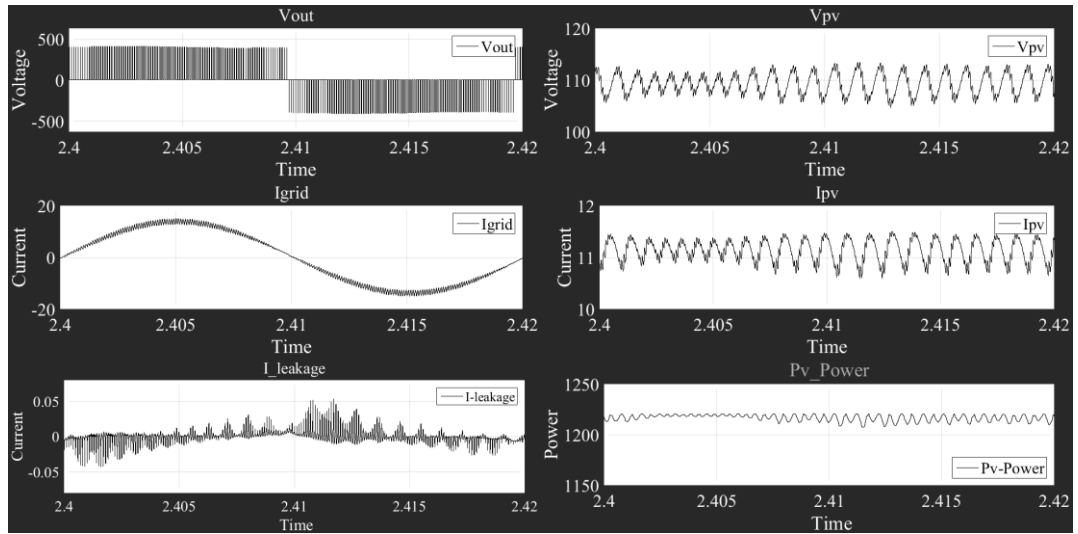


Figure 6.6 Grid connected PV system with proposed inverter

Figure 6.7 shows the experimental result for proposed topology. It should be noted that, in the experiment, 22nF – 1 ohm snubbers are used across the switches 5 and 6.

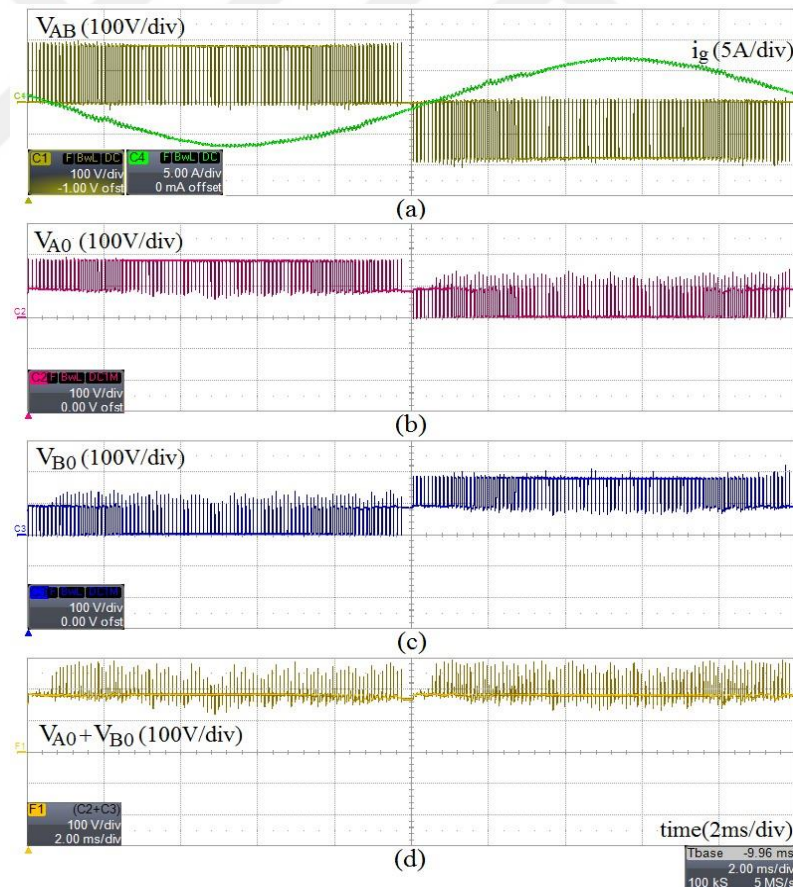


Figure 6.7 Experimental waveforms of proposed converter for grid connection for one grid period and for one switching period a) Inverter voltage and current b) V_{A0} c) V_{B0} d) $(2 \times \text{Common mode voltage } V_{A0} + V_{B0})$

The leakage current for the proposed inverter is shown in Figure 6.8 and the rms value of the leakage current is 89mA.

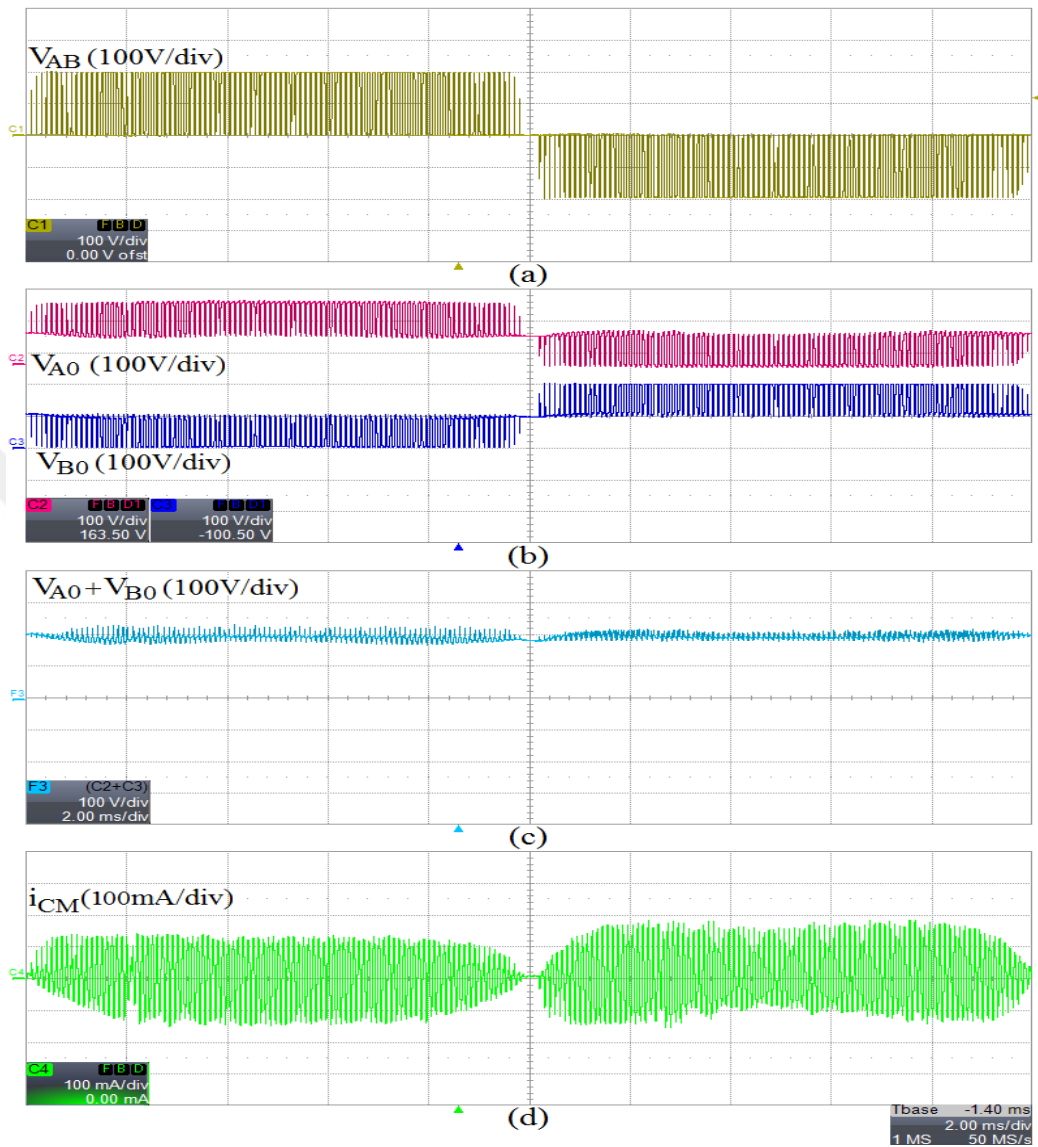


Figure 6.8 Experimental waveforms of proposed converter for grid connection for one grid period and for one switching period a) Inverter voltage and current b) $V_{A0} - V_{B0}$ c) $(2 \times \text{Common mode voltage})$ $V_{A0}+V_{B0}$ d) Leakage current

6.1.2 oH5 Topology

The simulation results under the constant DC link voltage is shown in Figure 6.9 for oH5 topology (Figure 3.9). It can be seen that, the leakage current is low and common mode voltage is constant while inverter works at unity power factor.

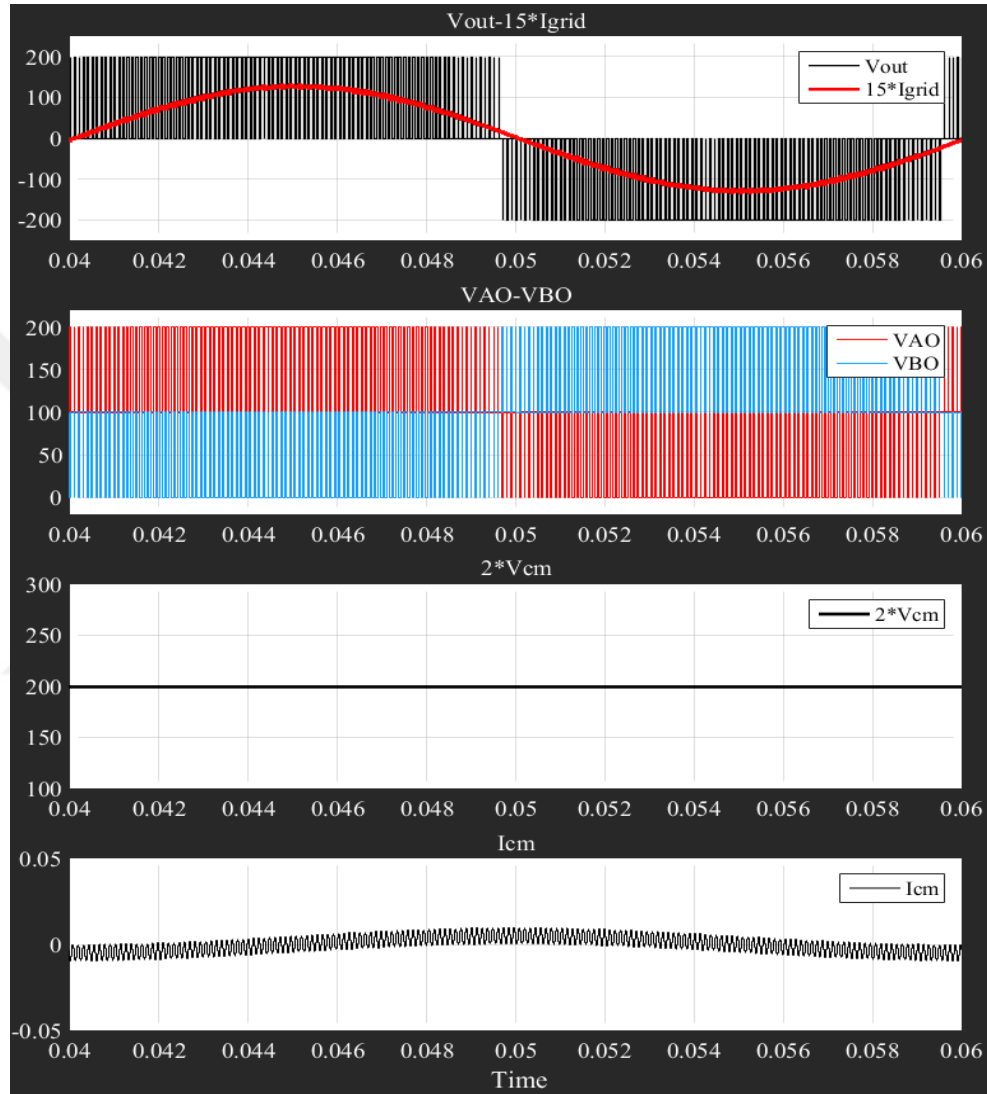


Figure 6.9 Simulation results under the constant DC link voltage for oH5 topology

Figure 6.10 shows the simulation results for the oH5 topology with PV modules and two-switch buck boost converter. A 850uF DC link capacitors have been used as the input capacitance of the inverter and a 500uF capacitor is connected in parallel to the PV module. The leakage current is bigger than the other converters. The output voltage (V_{pv}) and the output current (I_{pv}) of the PV module are fluctuating with the same parameters used in other inverter topologies.

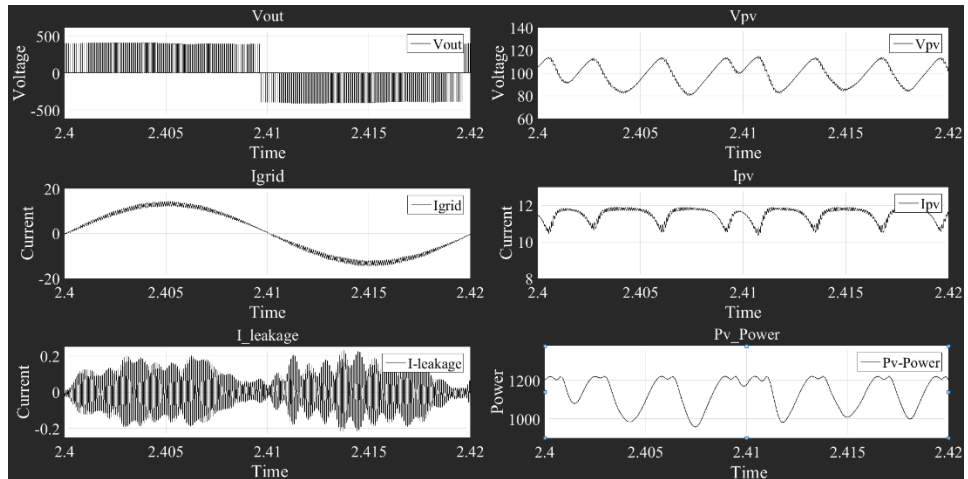


Figure 6.10 Grid connected PV system with oH5 inverter

Figure 6.11 shows the experimental results for the oH5 topology. A 22k ohm discharge resistors in parallel to each DC link capacitor is used and these resistors ensure the capacitor voltages equally divided. The rms value of the leakage current is 129mA.

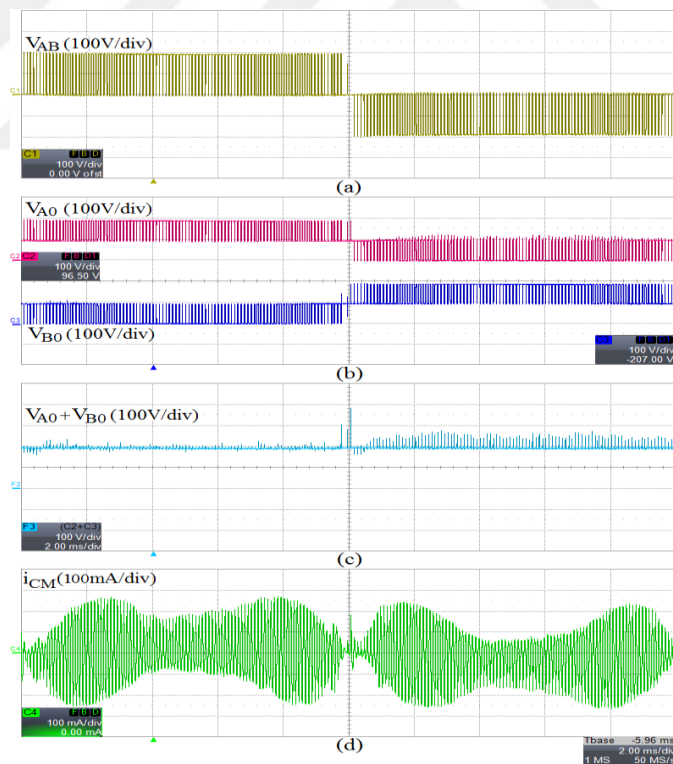


Figure 6.11 Experimental waveforms of oH5 converter for grid connection a) Inverter voltage and current b) $V_{A0} - V_{B0}$ c) $(2 \times \text{Common mode voltage}) V_{A0} + V_{B0}$ d) Leakage current

6.1.3 H6 and Improved H6 Topologies

H6 topology has not been connected to the grid since the gate driver modules in the laboratory are not compatible to the gate logic in the circuit. Therefore the simulations have been carried out only for the H6 topology (Figure 3.7). Two 850uF DC link capacitors are used at the input of the inverter and a 500uF capacitor is connected in parallel to the PV module in the model. Figure 6.12 shows the simulation results for the H6 topology with the PV system. It can be seen that, leakage current lower than the 100mA and the inverter output voltage is unipolar form when the inverter is operated at unity power factor. The PV module supplies the maximum power to the grid and fluctuation of the power is lower.

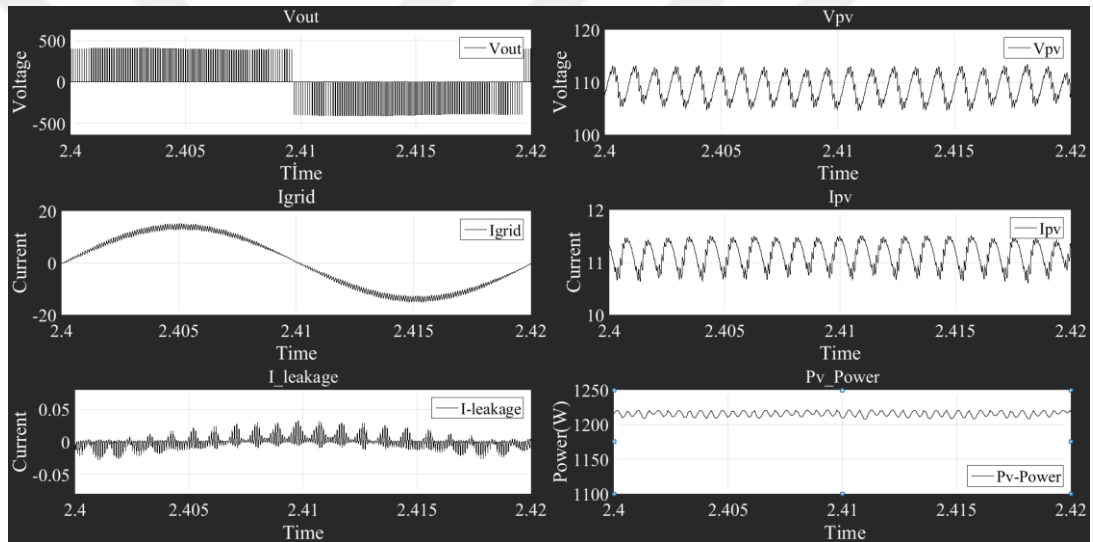


Figure 6.12 Grid connected PV system with H6 topology

Experimental work has been carried out on the improved inverter topology by using the parameters in Table 6.1. Figure 6.13 shows the experimental results recorded from the improved H6 topology under the constant DC link voltage. The common mode voltage fluctuates in improved H6 topology because of the resonance circuit as it can be seen in Figure 6.13. The leakage current at is almost equal to 20mA in rms.

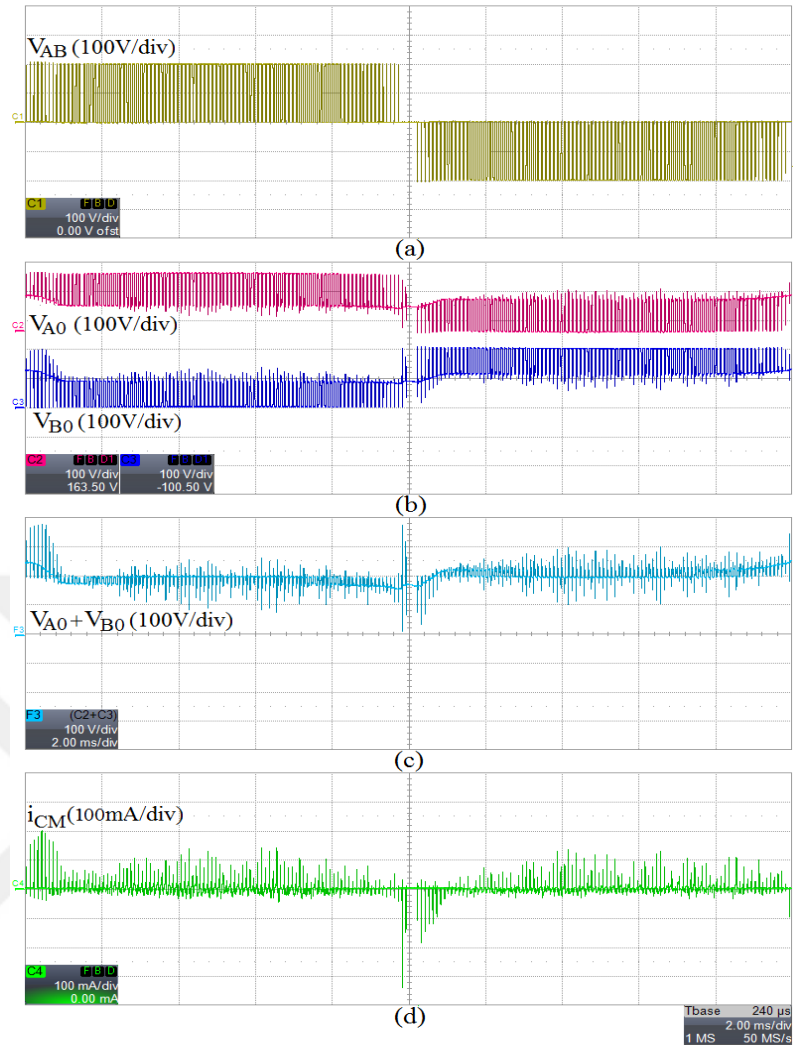


Figure 6.13 Experimental waveforms of improved H6 converter for grid connection a) Inverter voltage and current b) V_{A0} - V_{B0} c) ($2 \times$ Common mode voltage) $V_{A0} + V_{B0}$ d) Leakage current

The efficiency of the inverters given in Figure 6.14 has been measured in the laboratory under the constant DC link voltage.

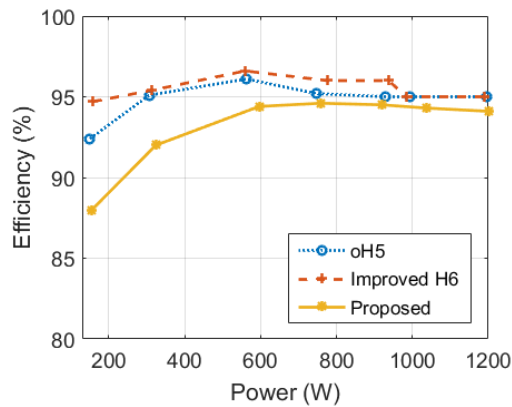


Figure 6.14 Efficiency of the experimentally tested topologies

6.2 Simulation and Efficiency Calculation with PSpice

The H6 structure have been simulated under the RL load as described in section three by using the MATLAB/Simulink with PSpice. Firstly, the H6 topology is simulated by using MATLAB and the generated gate signals have been recorded into a text file. Then, these gate signals have been used in PSpice program. Figure 6.15 shows the PSpice model of the H6 inverter topology.

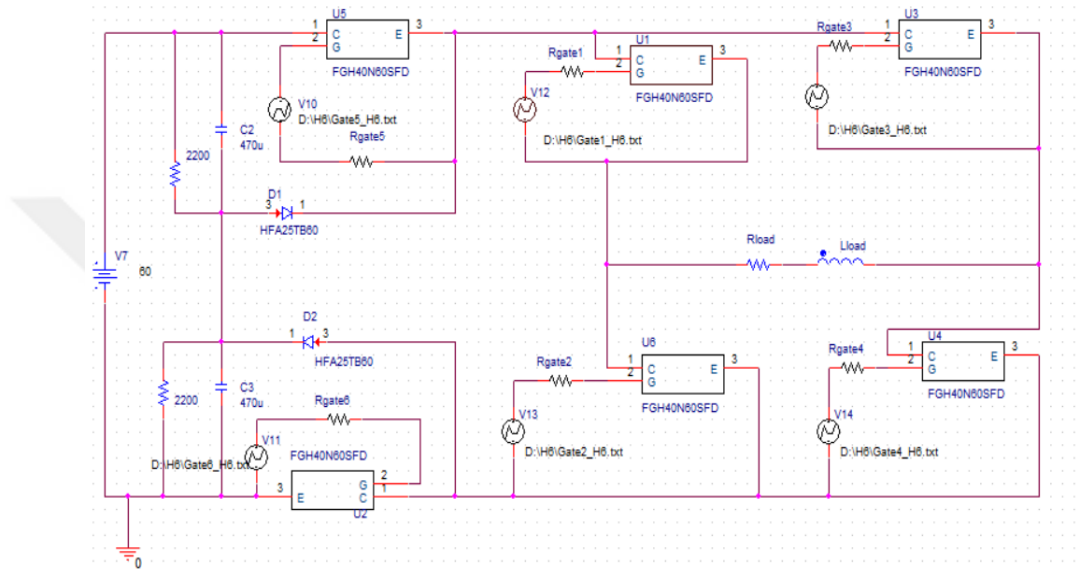


Figure 6.15 Schematic of the converter in SPICE

The solid-state devices (IGBTs) having the characteristics in PSpice package program are used in the experimental setup in order to compare the results of PSpice simulation and experimental work. Figure 6.16 shows the experimental setup for the H6 topology.

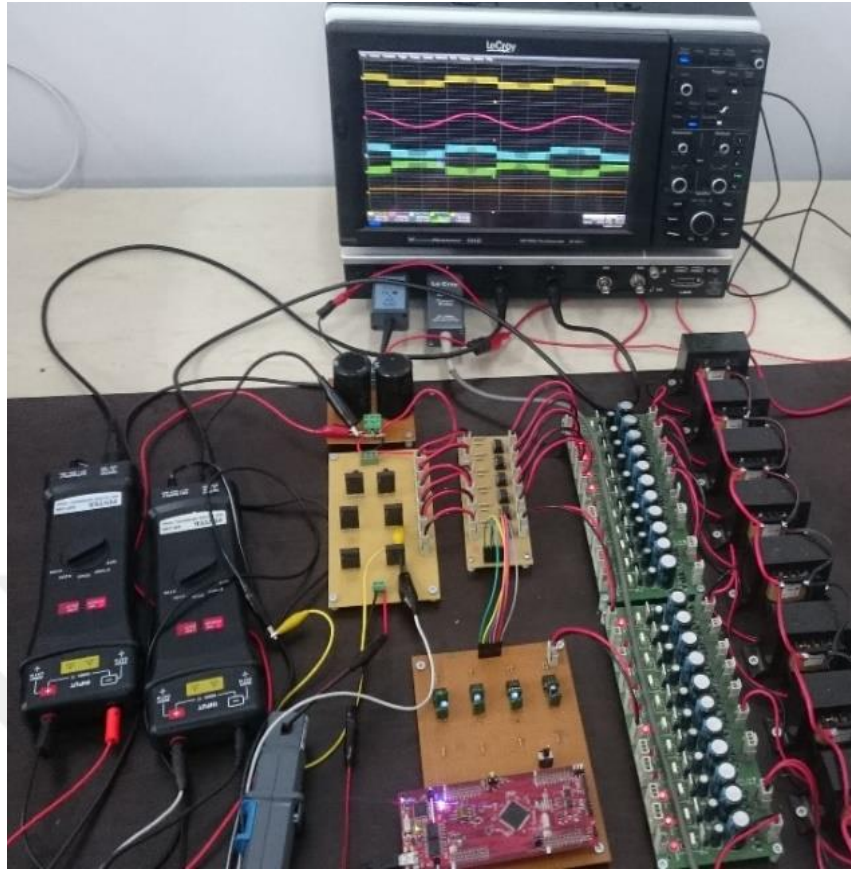


Figure 6.16 Picture of prototype used for experimental test (Personal archive, 2018)

The circuit parameters and component codes of the H6 bridge topology used in the simulations and experiment work are given in Table 6.2. The SPICE parameters of the IGBT and diodes used in simulations are taken from the manufacturer websites. Thus, the nonlinear properties of the semiconductor elements are taken into consideration in the SPICE software.

Table 6.2 Circuit Parameters

System Parameters	Value
Input Voltage	60 VDC
Switching Frequency	5 kHz
DC capacitors	470 uF
Load Inductance	7.14 mH
Load Resistance	16Ω, 19.2 Ω, 24 Ω, 32 Ω, 48 Ω
IGBT S1 - S6	FGH40N60
Diodes D1 - D2	UF5408
Micro Controller	F28377s

The results of the SPICE simulation and experimental work on the circuit are recorded when the load resistance and load inductance are 32Ω and 7.14 mH , respectively. The differential mode voltage, the load current, the load terminal voltages with respect to the negative rail (V_{A0} and V_{B0}) and the common mode voltage are given in Figure 6.17 and Figure 6.18. It should be noted that the ground level of V_{A0} is shifted to separate the waveforms on the same screen from each other.

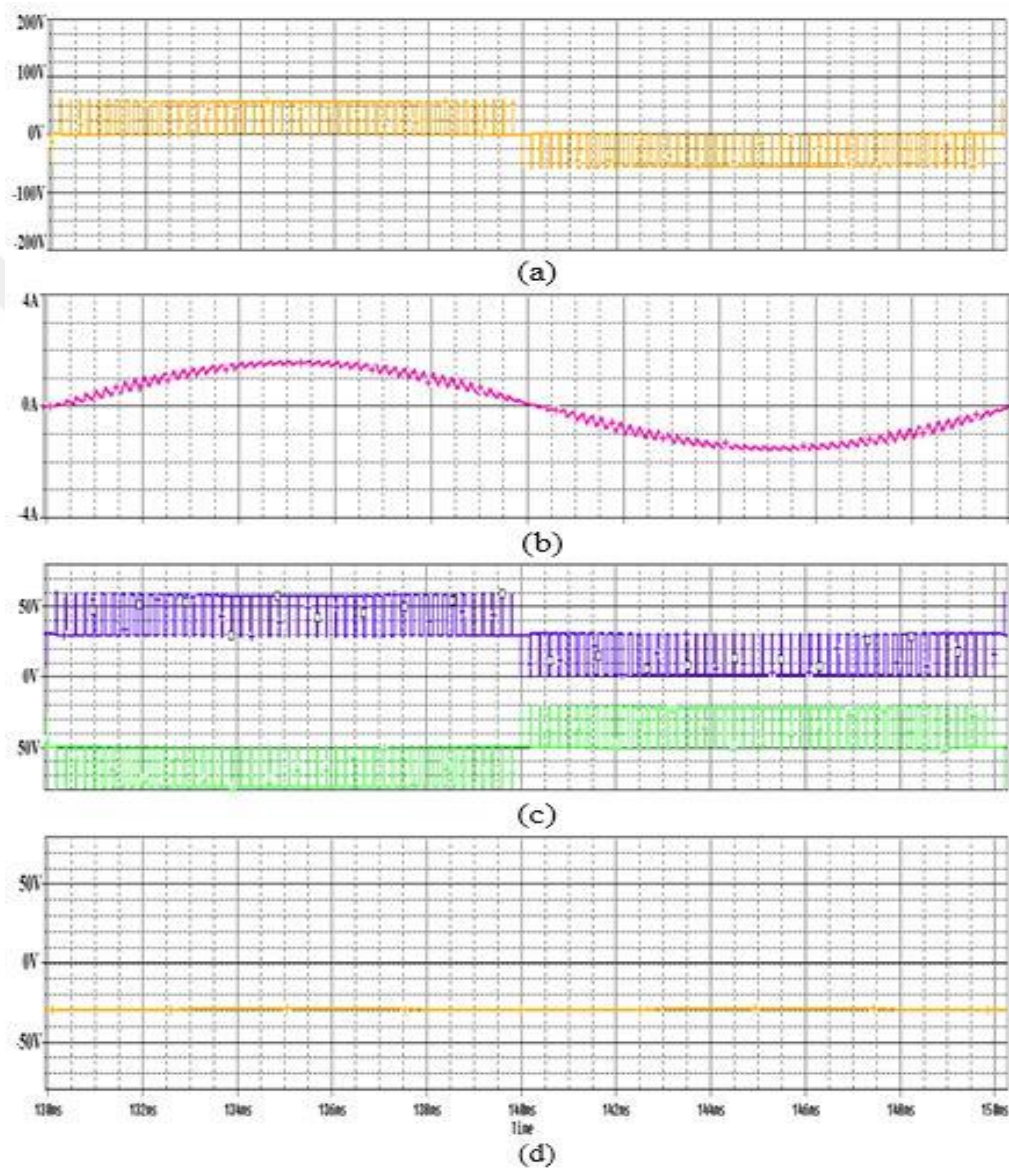


Figure 6.17 Simulation Results a) Differential mode voltage waveform b) Load current c) V_{A0} and V_{B0} voltage (Note that, V_{A0} is shifted to observe the waveform clearly) d) Common mode voltage ,time axis are same for all waveforms

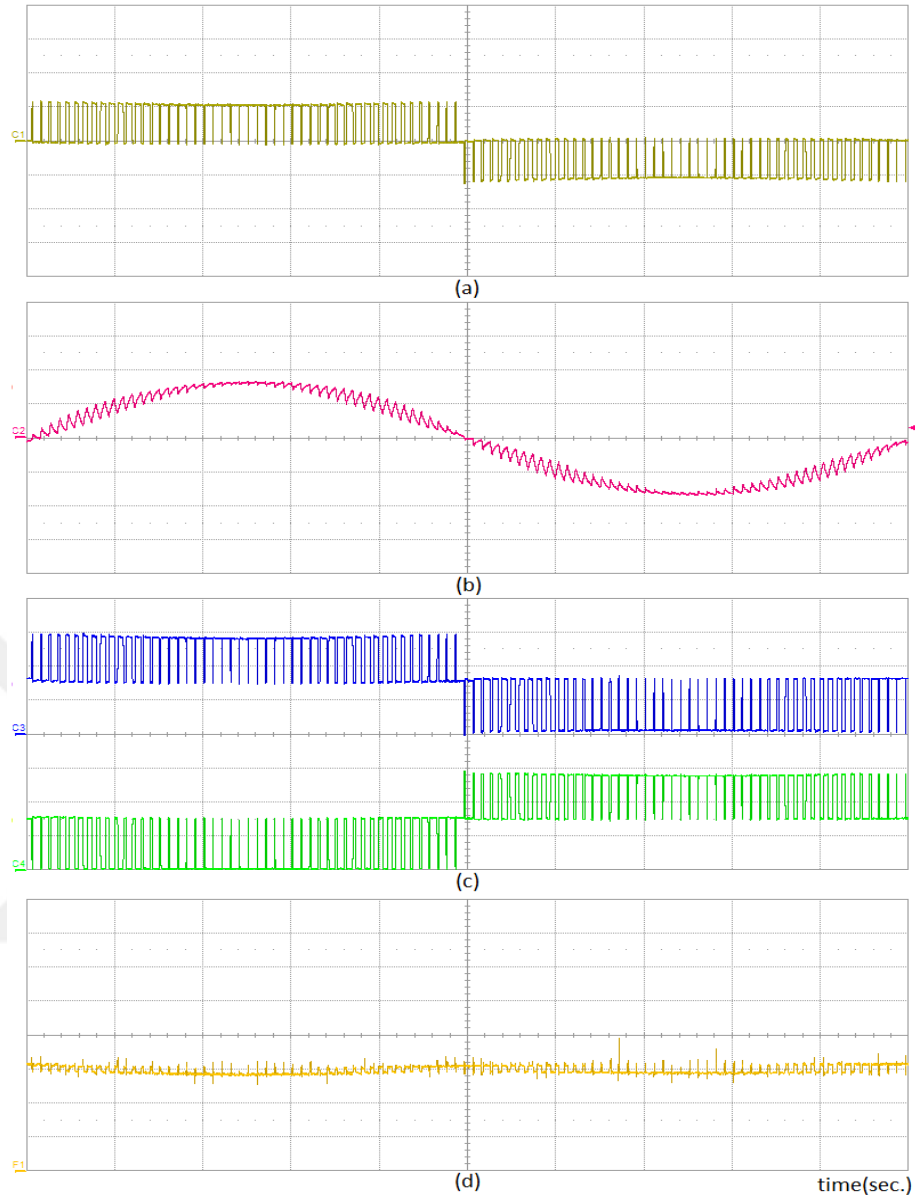


Figure 6.18 Experimental results a) Differential mode voltage wave form (50 V/div) b) Load current (1 A/div) c) V_{A0} and V_{B0} voltage (20 V/div) d) Common mode voltage (20 V/div)

The inverter efficiencies from the PSpice simulation, experimental work and theoretical calculation by using equation 3.11-3.18 are compared under the different loading condition in Table 6.3. The inductance value in the load is retained constant (7.14 mH) while the resistance is changed in order to vary the real power flowing through the load.

Table 6.3 Power and Efficiency comparison

Rload (Ω)	Efficiency Calculation ($\% \eta$)		
	Simulation	Theoretical	Experimental
48	88.93	86.85	89.63
32	88.61	86.56	88.64
24	88.08	87.76	87.97
19.2	87.45	86.07	86.97
16	86.5	85.84	86.21

6.3 Boost Converter with Model Predictive Current Control

The boost converter with model predictive control technique have been simulated by using MATLAB/Simulink. Firstly, valley current equation given in (5.11) is applied in order to control the valley current and then the same equation is used for the controlling peak and average currents by changing the modulation technique given in Figure (5.7). Figure 6.19 shows the MATLAB model for the boost converter with model predictive control. Reference inductor current of the boost converter has been selected as 40 A. Figure 6.20 shows the simulation results of the inductor current for the different modulation techniques. The trailing edge modulation (Figure 5.7-a), trailing triangle modulation (Figure 5.7-c) and leading edge modulation (Figure 5.7-b) techniques have been used and the valley average and peak inductor currents have been controlled respectively for them as seen in Figure 6.20.

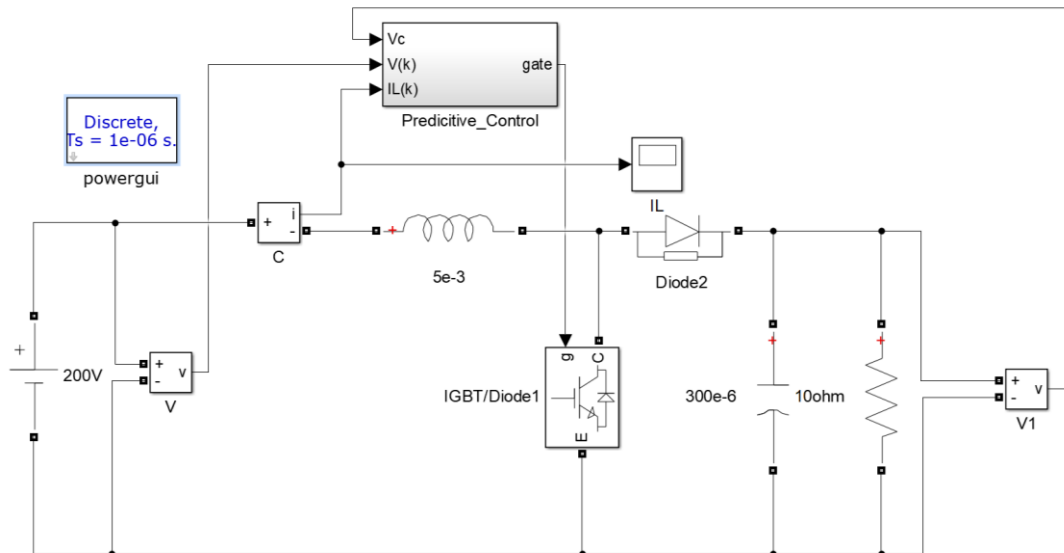


Figure 6.19 Boost converter with predictive control

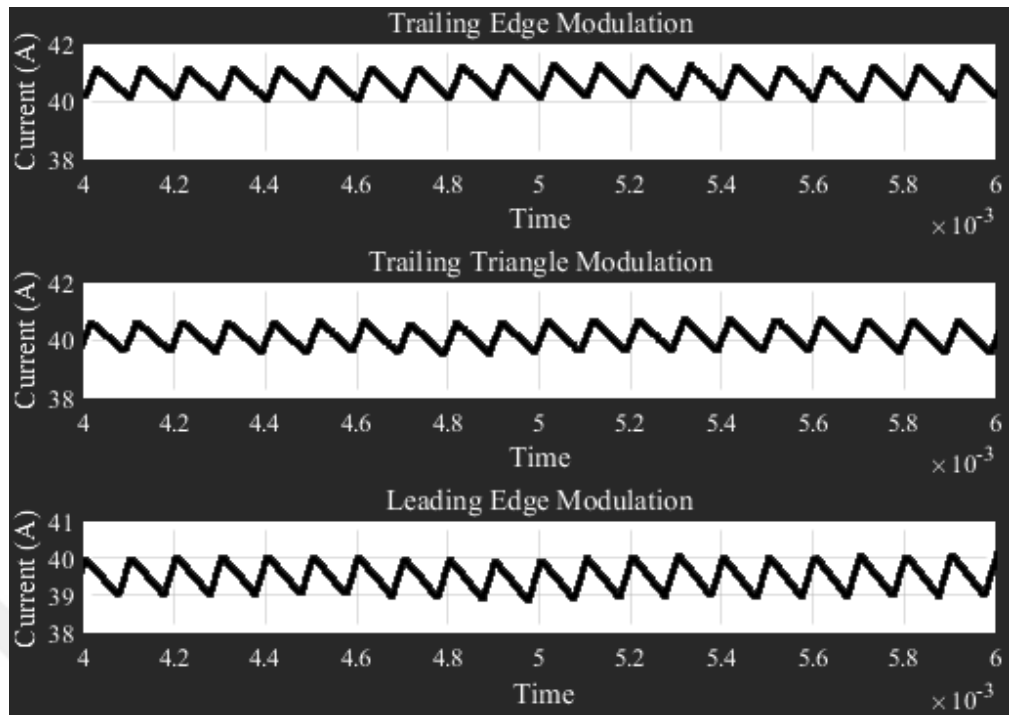


Figure 6.20 Inductor current of the boost converter under the different modulation technique (trailing edge, trailing triangle and leading edge modulation)

6.3.1 Predicted Current Control with Perturb and Observe Algorithm

The MATLAB/Simulink model shown in Figure 6.21 has been simulated to analyze the effect of the model predictive control for MPPT operation. In this model, three different control techniques have been examined; voltage oriented perturb observe (PO) MPPT algorithm with continuous control set MPC (valley current equation given in 5.11), voltage oriented PO-MPPT algorithm with finite control set MPC (equation 5.7), and only voltage oriented PO-MPPT algorithm given in Figure 5.4. The used control schematic is given in Figure 5.3 for voltage oriented MPPT with MPC.

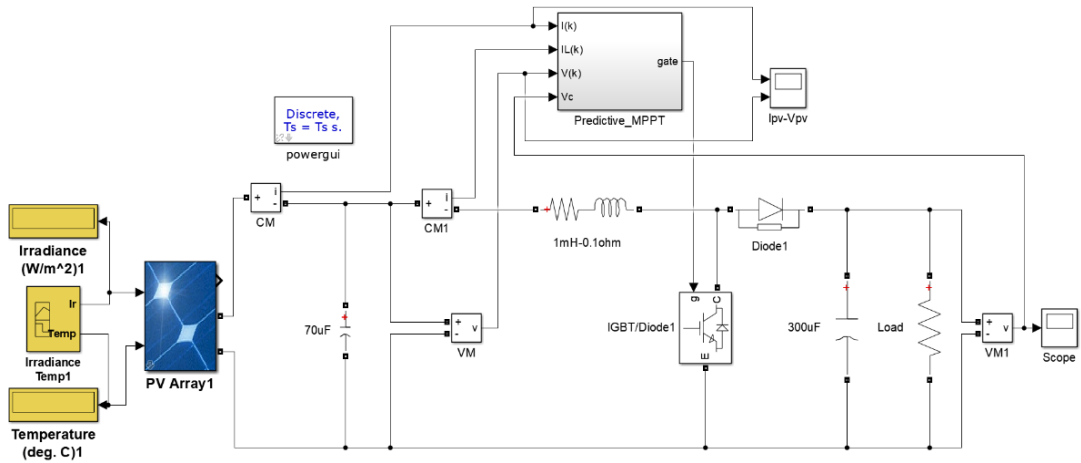


Figure 6.21 PV system with boost converter

A boost converter has been connected to the output of the PV module. The initially 1000W/m^2 irradiance is applied on the PV module until the 0.3 second and the irradiance of the PV module decreases sharply the 750W/m^2 after 0.3 seconds to analyze transient effect of the control methods. Figure 6.22 shows the characteristics of the PV module used in simulation. This transient operation of the system is analyzed with three different control methods.

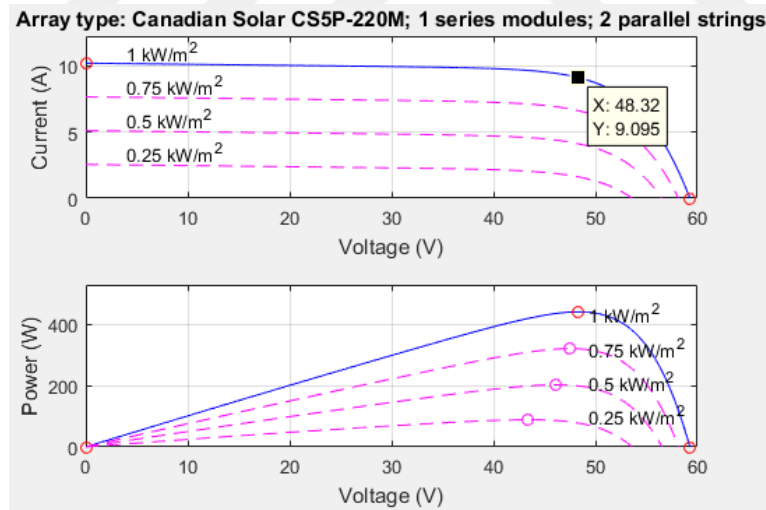


Figure 6.22 PV characteristic

The digital PI controller is used in Matlab/Simulink. The change of the output of the PI controller given in equation (5.31). By using the equation (5.32), the digital PI controller block has been created and used in Matlab as it is given in Figure 6.23. K_p and K_i shows the proportional and integral gain of the PI controller and T_s represent the sampling time of the system.

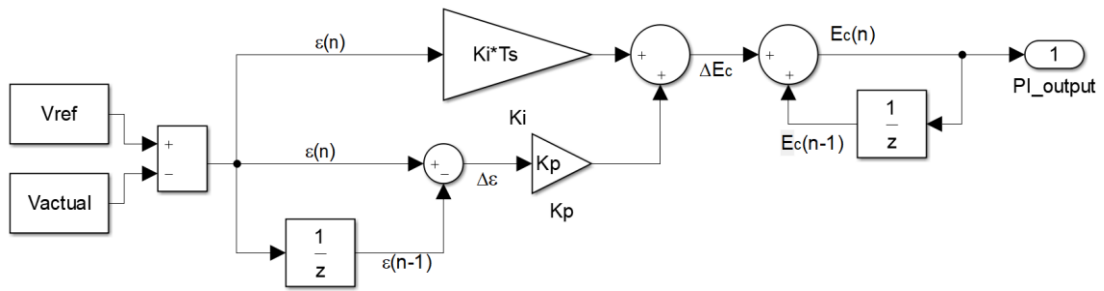


Figure 6.23 Digital PI controller used in Matlab

Figure 6.24 shows the PV voltage and PV current for voltage oriented MPPT algorithm. The output of the MPPT is the voltage and it is passed through the PI controller in order to generate the duty cycle as the reference for gate drive. In this control method, the sample time of the MATLAB is equal to $1\mu\text{s}$ and switching frequency is equal to 10 kHz. Figure 6.24 shows that a steady state oscillation occurs on the current and voltage of the PV module and the frequency of this oscillation is about 1 kHz. This oscillation has been created by the P&O algorithm oscillating around the MPP. It can be reduced by reducing the disturbance value of the P&O algorithm but the decreasing the disturbance value increases the convergence time.

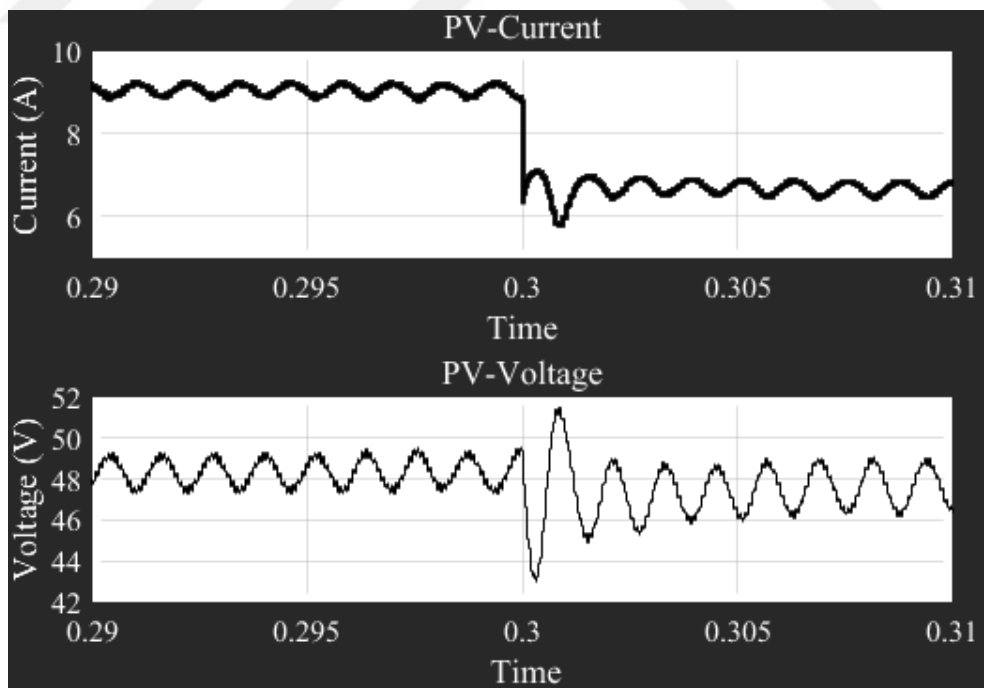


Figure 6.24 Voltage oriented perturb observe algorithm results

Figure 6.25 shows the PV voltage and PV current for voltage oriented MPPT algorithm with FS-MPC. The output of the MMPT is the reference voltage and it is

passed through the PI controller in order to obtain the current reference for FS-MPC based controller. In this model, the sample time of the model is selected $40\mu\text{s}$. The steady state oscillation still occurs because of the P&O algorithm.

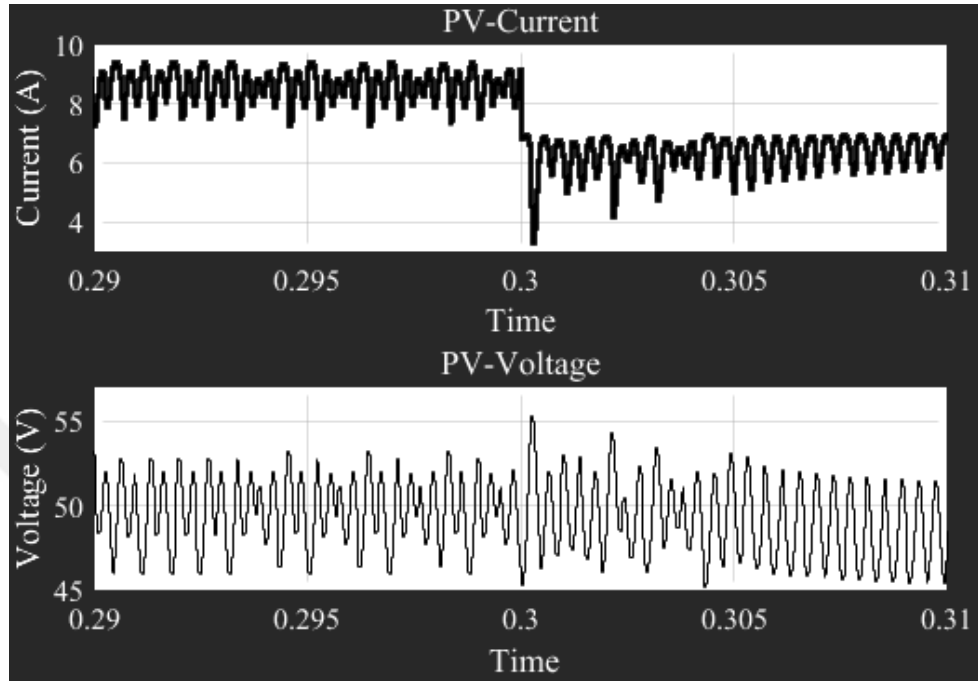


Figure 6.25 Voltage oriented perturb observe algorithm with FS-MPC results

Figure 6.26 shows the PV voltage and PV current for voltage oriented MPPT algorithm with the valley current control model predictive control (VCC-MPC). The output of the MMPT is the reference voltage and it is passed through the PI controller in order to obtain the current reference for VCC-MPC based controller. In this control method, the sample time of the MATLAB is equal to $1\mu\text{s}$ and the switching frequency is equal to 10 kHz. The P&O algorithm creates almost 1.5 kHz steady state oscillation in the voltage and current of the PV module as shown in Figure 6.26.

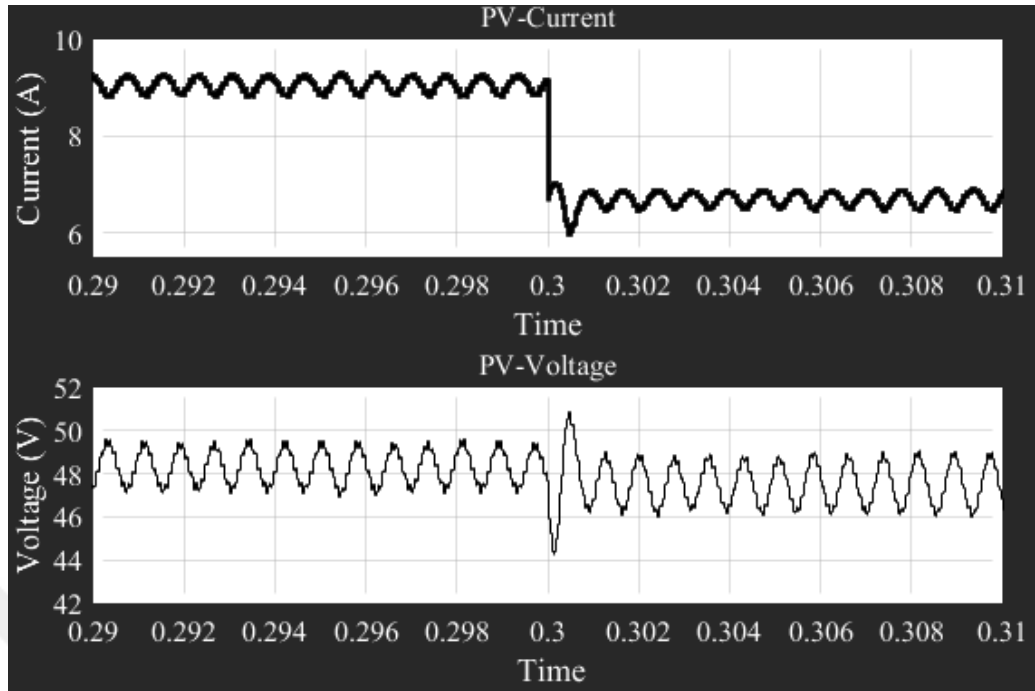


Figure 6.26 Voltage oriented perturb observe algorithm with VCC-MPC results

According to these results, it can be observed that, the voltage oriented perturb observe algorithm (MPPT) with VCC-MPC is effective control method. It tracks the maximum power point robustly. The voltage oriented perturb observe algorithm with FS-MPC does not has constant switching frequency since it does not require the modulator. Therefore, the switching frequency is varying and it increases up to 25 kHz (sample rate for the used model) and the maximum power point is not tracked robustly. Moreover, all the algorithms creates a steady state oscillation on the PV voltage and current, because all the control algorithms use P&O method for the MPPT operation.

6.3.2 Particle Swarm Optimization with Duty Cycle Control

In order to eliminate the steady state oscillation, the particle swarm optimization (PSO) based MPPT algorithm could be used instead of the P&O based MPPT algorithm. In this method, three duty cycles have been used as particle. This algorithm has been applied by using flowchart given in Figure 5.12. First of all, the PSO algorithm is employed in the simulation model given in Figure 6.21.

The initialization and boundaries of the parameters used in the simulation are given in Table 6.4. After the initialization, the particles (three different duty cycles)

are applied to the converter and the corresponding powers are calculated. It should be noted that the time interval between two particles applied to the converter must be longer than the settling time of the converter. Therefore, each particle has been applied to the converter during 0.1 seconds and then the related power of the particle has been calculated by multiplication of the PV voltage and current at the steady-state. After all particles have been applied to the converter and all powers are calculated, the g_{best} and p_{best} values have been determined, then new particles have been generated by using the equation (5.33) and (5.34). Note that, initial p_{best} have been selected as initial values of the particles and initial g_{best} have been determined after the first iteration. Before, the new particles are applied to the converter, the convergence criteria are checked. Maximum iteration number, which is selected as 30 and maximum velocity of the particles which is selected as 0.01, are selected as the convergence values.

Table 6.4 Initial values and boundaries of parameters

Parameters	Boundaries of Parameters
$d_{max} - d_{min}$	0.9 - 1
$c_{1max} - c_{2max}$	2
$c_{1min} - c_{2min}$	1
$r_1 - r_2$	0.1
$w_{max} - w_{min}$	1 - 0.1

After the convergence criteria is satisfied, g_{best} value is applied to the converter until the shading or load conditions change. If the loading or shading conditions change, the PSO algorithm re-initialized to find the new MPP. The equation (5.38) is used for detecting the photovoltaic power change. Here, ΔP is equal to 10% and if the equation (5.38) is satisfied, the PSO algorithm is re-initialized.

Figure 6.27 shows the simulation results for the PSO. The PSO algorithm have three particle to find MPP. Initially these particles (duty cycles) are selected as 0.17, 0.5 and .088. Each particle has been applied to the converter during 0.1 seconds. These three particle are applied to the converter and the related power of the particles are calculated at the end of one iteration cycle. One iteration cycle takes 0.3 seconds approximately. Since the transition time of the PSO algorithm takes longer time, the

simulation program has been run during 10 seconds. The 1000 W/m^2 irradiance level has been applied to the photolytic panel until 6.5 seconds from beginning after then the irradiance level has been sharply decreased to the 750 W/m^2 . As it can be seen in Figure 6.27, PSO algorithm has obtained the MPP with 99.4% correctness at 4.5 seconds for 1000 W/m^2 irradiance level. When irradiance change, the PSO algorithm has been re-initialized to search the new MPP with the three particle (duty cycle) and it has found the new MPP in 3 second.

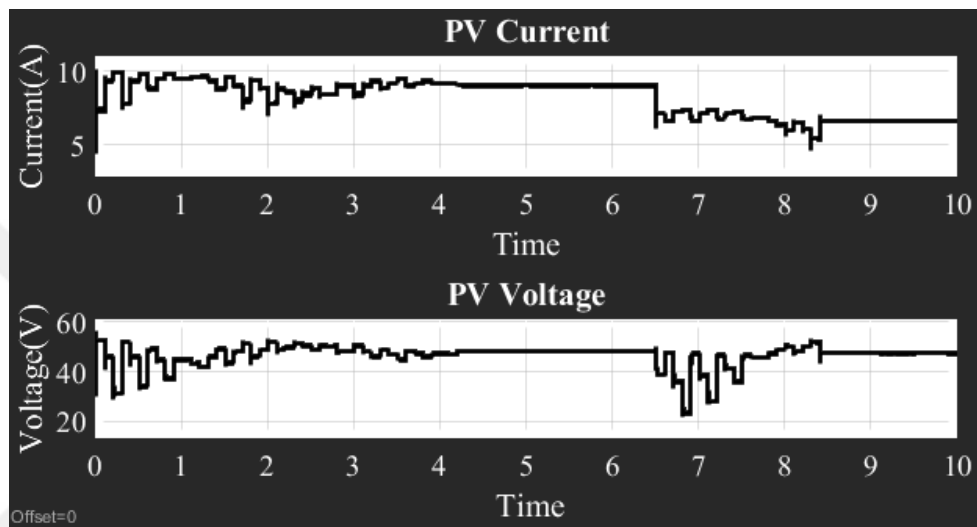


Figure 6.27 Simulation result of MPPT with PSO algorithm

The transient time of the PSO algorithm is longer than that of the P&O algorithm as it can be seen in Figure 6.24 and Figure 6.27. Although, the P&O based algorithm has steady state oscillation, the PSO algorithm has not created any steady state oscillation. The Figure 6.28 shows the current and voltage waveforms of the PV module with PSO algorithm. In this figure, it can be seen that the PSO algorithm does not create any steady state oscillation. The oscillations are at the switching frequency as it is expected.

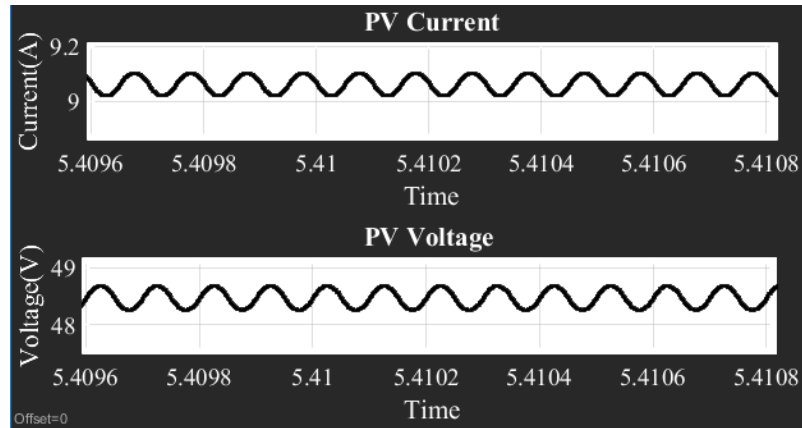


Figure 6.28 Zoomed current and voltage waveform of the PSO

Another comparison is performed between the P&O algorithm and the PSO algorithm based on the inductance current. Figure 6.29 shows the inductance current of boost converter with the voltage oriented P&O (voltage disturbance is 5mV each switching frequency.) algorithm. In this method P&O algorithm work with PI controller to generate duty cycle. Here, it can be seen that the inductance current has the steady state oscillation and it goes into the discontinuous conduction mode, too. Operation of converter in the discontinuous current mode increases the current rating of the solid state devices used in the DC to DC converter.

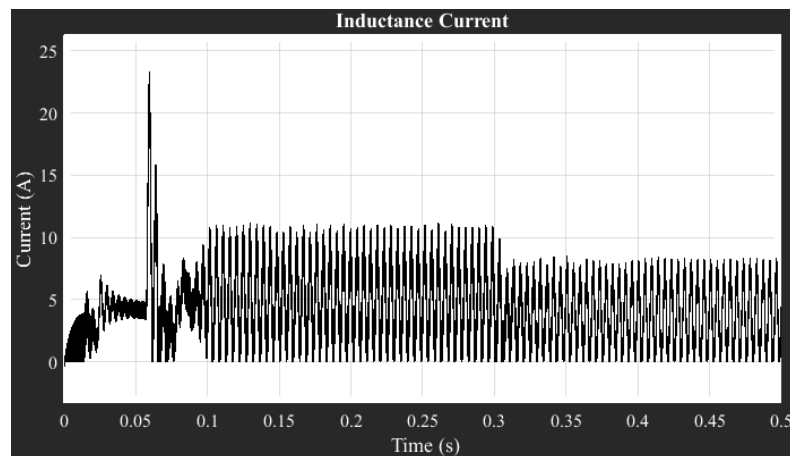


Figure 6.29 Inductance current of the boost converter with voltage oriented P&O

Moreover, only P&O algorithm can be used for MPPT operation. If the duty cycle is controlled instead of the voltage in the P&O algorithm, it do not need to any other controller such as PI controller to generate the duty cycle. In this method, output of the P&O algorithm is used directly as duty cycle (duty disturbance is 0.0001 at each switching cycle). Figure 6.30 shows the simulation result of the duty controlled P&O

algorithm. In here, it can be seen that the inductance current has the steady steady oscillation and it goes into the discontinuous conduction mode as in voltage oriented P&O algorithm. The frequency of the oscillation approximately 200 Hz.

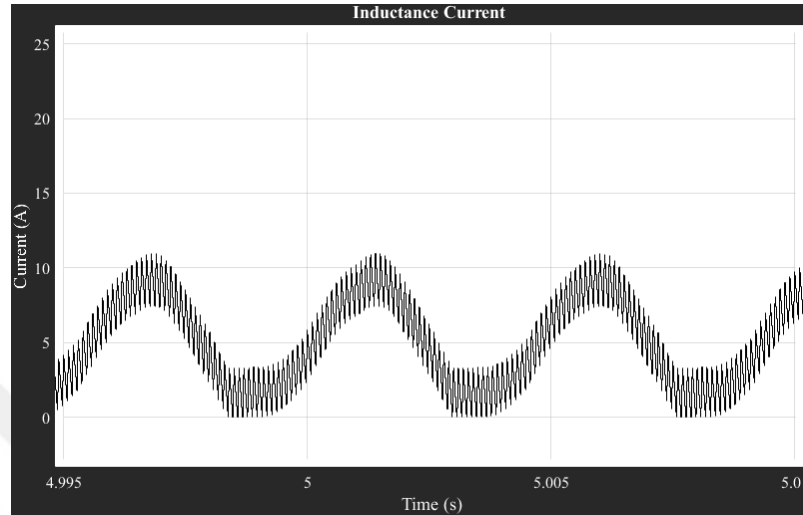


Figure 6.30 Inductance current of the boost converter with duty controlled P&O

However, if the PSO algorithm is used, the inductance current stays in the continuous conduction mode at the steady state under the MPP operating condition as it can be seen in Figure 6.31. The PSO algorithm apply the constant duty cycle after finding the global maximum power until the environmental conditions change. The high spikes on the inductance current are due to the sudden changes in the applied duty cycle during the search of the PSO algorithm. It can be eliminated by changing the duty cycle in a reasonable range.

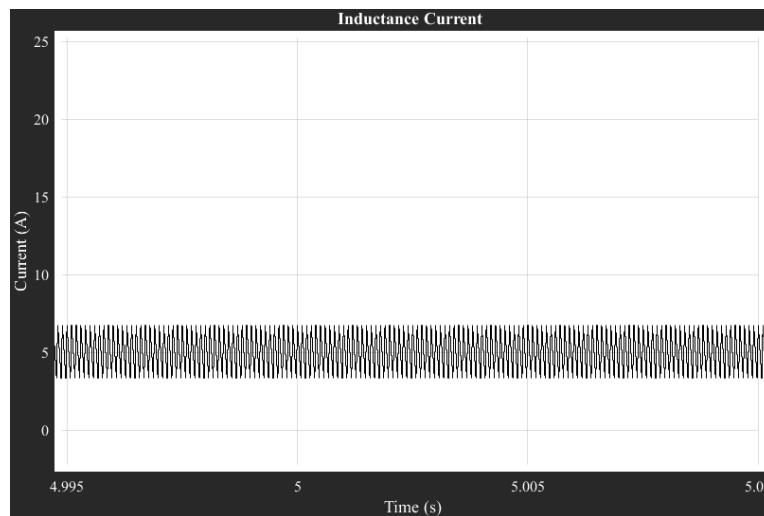


Figure 6.31 Inductance current of the boost converter with PSO

CHAPTER SEVEN

CONCLUSION

In this study, a single phase transformerless PV inverter is proposed and analyzed for the grid connected PV system application. This proposed inverter topology and other commonly used grid connected topologies have been simulated by using MATLAB/Simulink, and they have been tested in laboratory under the constant DC link voltage condition. The proposed inverter topology has seven fully controlled semi-conductor devices, one DC link capacitor and two snubber circuits. This topology decouples the PV panel from the grid during the zero voltage levels of inverter output voltage. It suppresses the high frequency common mode voltage and the leakage current without creating any resonance in the network. A single DC link capacitor is used to eliminate the voltage balancing issue and it reduces the failure probability of more electrolytic capacitors used in the system. Also, this proposed inverter topology is fully compatible with the standard unipolar switching enabling the use of PWM ports of digital signal processors.

A new simulation technique has also been proposed. This technique based on co-operation of the MATLAB/Simulink and PSpice package programs. This proposed technique is tested with one of the commonly used transformerless inverter. The results are compared to the experimental and the data used from the manufacturing data book. It is observed that the proposed method in this paper is less time consuming and fair technique, and can be implemented on any power converter that can be simulated in the MATLAB.

The proposed and other PV inverter topologies connected to the PV module with two-switch buck boost are analyzed and compared in detail. Also, the effect of the model predictive current control on determination of maximum power point of the photovoltaic modules has been studied to determine the fast and robust maximum power point tracking system.

The voltage controlled perturb and observe algorithm with the linear PI controllers and the voltage controlled perturb and observe with the predictive current control method have been compared by using the MATLAB/Simulink. The steady

state oscillation around the MPP due to perturb and observe algorithm has been recognized. In order to overcome this oscillation problem, the particle swarm optimization based MPPT algorithm is implemented. It observed that, the particle swarm algorithm does not create the steady state oscillation but its settling time is longer when it is compared to the perturb and observe algorithm. The inductance current of the step up DC/DC converter can go into the discontinuous conduction mode if the P&O algorithm is used because of this oscillation. However, the simulation results show that, if the PSO algorithm is used then the inductance current can stay in continuous conduction mode at same loading conditions.

7.1 Future Work

The work on the efficiency of proposed inverter will continue with possible modulation techniques in order to increase it. Also the MPPT algorithm with particle swarm optimization will be investigated more in order to reduce the settling time with fast computational capability under dynamic change of weather condition.

REFERENCES

- Araújo, S. V., Zacharias, P., & Mallwitz, R. (2010). Highly efficient single-phase transformerless inverters for grid-connected photovoltaic systems. *IEEE Transaction on Industrial Electronics*, 57(9), 3118-3128.
- Azary, M. T., Sabahi, M., Babaei, E., Meinagh, F. A. A. (2018). Modified single-phase single-stage grid-tied flying inductor inverter with MPPT and suppressed leakage current. *IEEE Transaction on Industrial Electronics*, 65(1), 221-231.
- Azri, M., Rahim, N. A., & Halim W. A. (2015). A highly efficient single-phase transformerless H-bridge inverter for reducing leakage ground current in photovoltaic grid-connected system. *Taylor&Francis Electric Power Component and System*, 43, 928-938.
- Balıkcı, A., Azizoglu, B. T., Durbaba, E., Akpınar, E. (2017). Efficiency calculation of inverter for PV applications using MATLAB and SPICE. Aegean Conference on Electrical Machines and Power Electronics (ACEMP), Romania, 593-598.
- Balıkcı, A., Akpınar, E., & Durbaba, E. (2017). Single-phase STATCOM with multilevel U-cell converter. 10th International Conference on Electrical and Electronics Engineering (ELECO), Bursa, 340-344.
- Barater, D., Buticchi, G., Cocari, C., Franceschini, G., & Lorenzani, E. (2012). Unipolar PWM strategy for transformerless pv grid-connected converters. *IEEE transactions on energy conversion*, 27(4), 835-843.
- Barater, D., Lorenzani, E., Cocari, C., Franceschini, G., & Buticchi, G. (2016). Recent advances in single-phase transformerless photovoltaic inverters. *IET Renewable Power Generation*, 10(2), 260-273.
- Bruckner, T., Bernet S., & Guldner, H. (2005). The active NPC converter and its loss-balancing control. *IEEE Transaction on Industrial Electronics*, 52(3), 855-867.

- Buticchi, G., Barater, D., Lorenzani, E., & Franceschini, G. (2012). Digital control of actual grid-connected converters for ground leakage current reduction in pv transformerless systems. *IEEE Transactions on Industrial Informatics*, 8(3), 563–572.
- Chen, J., Prodic, A., Erickson, W. R., & Maksimovic, D. (2003). Predictive current programmed control. *IEEE Transaction on Power Electronics*, 18(1), 411-419.
- Cortes, P., Kazmierkowski, P. M., Kennel, M. R., Quevedo, E. D., & Rodriquez, J. (2008). Predictive control in power electronics and drivers. *IEEE Transaction on Industrial Electronics*, 55(12), 4312-4324.
- Danandeh, A. M., Mousavi, S. (2018). Comparative and comprehensive review of maximum power point tracking methods for PV cell. *Renewable and Sustainable Energy Reviews*, 82, 2743-2767.
- Enrique, J. M., Duran, E., Cardona, M. S., & Andujar, J., M. (2006) Theoretical assessment of the maximum power point tracking efficiency of photovoltaic facilities with different converter topologies. *Solar Energy*, 81, 31-38.
- Esrām, T., & Chapman, P. L. (2007). Comparison of photovoltaic array maximum power point tracking techniques. *IEEE Transaction on Energy Conversion*, 22, 439- 449.
- Freddy, T. K. S., Rahim, N., Hew, W. P., & he, H. (2014). Comparision and analysis of the single phase transformerless grid connected pv inverters. *IEEE Transaction on Power Electronics*, 29(10), 5358- 5369.
- González, R., Lopez, J., Sanchis, P., & Marroyo, L. (2007). Transformerless inverter for single-phase photovoltaic systems. *IEEE Transaction on Power Electronics*, 22(2), 693-697.
- González, R., Gubia, E., Lopez, J., & Marroyo, L. (2008). Transformerless single-phase multilevel-based photovoltaic inverter. *IEEE Transaction on Industrial Electronics*, 55(7), 2694-2702.

- Gu, Y., Li, W., Zhao, Y., Yang, B., Li, C., & He, X. (2013). Transformerless inverter with virtual DC bus concept for cost-effective grid-connected PV power systems. *IEEE Transactions on Power Electronics*, 28(2), 793-805.
- Gurbuz, F. (1997). *Optimal control of digitally controlled DC motors*. Phd Thesis, Dokuz Eylül University, Izmir.
- Gurbuz, F., Akpınar, E. (1998a). Simulation of pulse width modulated (pwm) chopper drives using Z- transformation. Mediterranean Electrotechnical Conference, Israil, 1255-1259.
- Gurbuz F, Akpınar E, (1998b). Optimal control of digitally controlled DC drive using a quadratic performance index", Proc. of International Conference on Electrical Machines, ISTANBUL, 1207-1212.
- Gurbuz, F, Akpınar E. (2002). Stability analysis of closed-loop control for a pulse width modulated DC motor drive", *Turkish Journal of Electrical Engineering and Computer Sciences*, 10(3), 427-438.
- Hafezi, H., Akpınar, E., & Balikci, A. (2014a). Cascade PI controller for single-phase STATCOM. 16th International Power Electronics and Motion Control Conference and Exposition, Antalya, 88-93.
- Hafezi, H., Akpınar, E., & Balikci, A. (2014b). Assessment of two different reactive power estimation methods on single phase loads. 16th International Power Electronics and Motion Control Conference and Exposition, Antalya, 82-87.
- Hernandez, J.A., Velasco, D., Trujillo C. L. (2011). Analysis of the effect of the implementation of photovoltaic systems like option of distributed generation in Colombia. *Renewable & Sustainable Energy Reviews*, 15 (5), 2290–2298.
- Islam, M., Mekhilef, S., & Hasan M. (2015). Single phase transformerless inverter topologies for grid-tied photovoltaic system: A review. *Renewable and Sustainable Energy Reviews*. 45, 69-86.

- Ishaque, K., Salam, Z., Amjad, M., & Mekhilef, S. (2012). An improved swarm optimization (PSO)- based MPPT for PV with reduced steady-state oscillation. *IEEE Transactions on Power Electronics*, 27(8), 3627-3638.
- Kakosimos, E. P., Kladas, G., A. (2011). Implementation of photovoltaic array MPPT through fixed step predictive control technique. *Renewable Energy*, 36, 2508- 5414.
- Kakosimos, E. P., Kladas, G, A., & Manias, N, S. (2013). Fast photovoltaic-system voltage- or current- oriented MPPT employing a predictive digital current controlled converter. *IEEE Transaction on Industry Application*, 60(12), 5673-5685.
- Khan, A., Brahim, L.B., Gasli, A., & Benammar, M. (2017). Review and simulation of leakage current in transformerless microinverters for PV applications. *Renewable and Sustainable Energy Reviews*, 74, 1240-1256.
- Kjaer, S. B., Pedersen, J. K., & Blaabjerg, F.Khan. (2005). A review of single –phase grid-connected inverters for photovoltaic modules. *IEEE Transaction on Industry Application*, 41(5), 1292-1306.
- Koad, R. B. A., Zobaa, A. F., & El-Shahat, A. (2017). A novel MPPT algorithm based on particle swarm optimization for photovoltaic system. *IEEE Transaction on Sustainable Energy*, 8(2), 468-476.
- Kolar, J. W., Ertl, H., & Zach, F. C. (1991). Influence of modulation method on the conduction and switching losses of a PWM converter system. *IEEE Transaction on Industry Application*, 27(6), 1063-1075.
- Kot, R., Stynski, S., Stepień, K., & Zaleski, J. (2016). Simple technique reducing leakage current for H-bridge converter in transformerless photovoltaic generation. *Journal of Power Electronics*, 16(1), 153-162.
- Kouro S., Malinowski, M., Gopakumar, K., Pou, J., Franquelo, L. G., Wu, B., & et al. (2010). Recent advances and industrial applications of multilevel converters. *IEEE Transaction on Industrial Electronics*, 57(8), 2553-2580.

- Li, W., Gu, Y., Luo, H., Cui, W., He, X., & Xia, C. (2015). Topology review and derivation methodology of single-phase transformerless photovoltaic inverters for leakage current suppression. *IEEE Transaction on Industrial Electronics*, 62(7), 4537-4551.
- Liu, H. Y., Huang, C. S., Huang, W. J., & Liang, C. W. (2012). A particle swarm optimization-based maximum power tracking algorithm for pv systems operating under partially shaded conditions. *IEEE Transaction on Energy Conversion*, 27(4), 1027- 1035.
- Mellit, A., Rezzouk H., Messai A., Medjahed B. (2011). FPGA-based real time implementation of MPPT-controller for photovoltaic system. *Renewable Energy*. 36, 1652-1661.
- Meneses, D., Blaabjerg, F., Garcia, O., & Cobos, J. A. (2013). Review and comparison of step-up transformerless topologies for photovoltaic AC-module application. *IEEE Transactions on Power Electronics*, 28(6), 2649-2663.
- Miyatake, M., & Veerachary, M. (2011). Maximum power tracking of multiple photovoltaic arrays: A PSO approach. *IEEE Transactions on Aerospace and Electronic Systems*, 47(1), 367-380.
- Mitova, R., Ghosh, R., Mhaskar, U., Klikci, D., Wang, M., & Dentella, A. (2014). Investigation of 600-V GaN HEMT and GaN diode for power converter application. *IEEE Transactions on Power Electronics*, 29(5), 2441-2452.
- Morales, D.S. (2010). Maximum power point tracking algorithms for photovoltaic applications. Master Thesis, Aalto University, Finland.
- Naayagi, R. T., Shuttleworth, R., Forsyth, A J (2011). Investigating the effect of snubber capacitor on high power IGBT turn-off. 1st International Conference on Electrical Energy Systems (ICEES), India, 50-55.
- Prasad, B. S., Jain, S., & Agarwal, V. (2008). Universal single-stage grid connected inverter. *IEEE Transaction on Energy Conversion*, 23(1) 128-137.

- Rashid, M. H., Kumar, N., & Kulkarni, A. R. (2014). Power Electronics devices, circuits, and applications (4th ed.). Pearson.
- Schweizer, M., & Kolar, J. W. (2013). Design and implementation of a highly efficient three-level T-type converter for low-voltage applications. *IEEE Transactions on Power Electronics*, 28(2), 899-907.
- Solarpowereurope, 2017. *European solar association*. Retrieved July 2017 from <http://www.solarpowereurope.org/home>.
- Taghvaei, M.H., Radzi, M.A.M., Moosavain, S.M., Hizam, H., Marhaban, M.H. (2013). A current and future study on non-isolated DC–DC converters for photovoltaic applications. *Renewable and Sustainable Energy Reviews*. 17, 216-227.
- Wang, C. M. (2008). A novel ZCS-PWM flyback converter with a simple ZCS-PWM commutation cell. *IEEE Transaction on Industrial Electronics*, 55(2), 749-757.
- Wang, F., Wu, X., Lee, F. C., Wang, Z., Kong, P., & Zhuo, F. (2014). Analysis of unified output MPPT control in subpanel Pv converter system. *IEEE Transactions on Power Electronics*, 29(3), 1275-1284.
- Wang, H., & Blaabjerg, F. (2014). Reliability of capacitors for DC-Link applications in power electronic converters—An Overview. *IEEE Transactions on Industry Applications*, 50 (5), 3569-3578.
- Wang, H., Liserre, M., & Blaabjerg, F. (2013). Toward reliable power electronics: challenges, design tools, and opportunities. *IEEE Industrial Electronics Magazine*, 7 (2), 17-26.
- Xiao, H., & S. Xie, S. (2011). Transformerless split-inductor neutral point clamped three-level PV grid-connected inverter. *IEEE Transactions on Power Electronics*, 42(7), 1799-1808.

- Xiao, H., S. Xie, S., Chen, Y., & Huang, R. (2011). An optimized transformerless photovoltaic grid- connected inverter. *IEEE Transactions on Industrial Electronics*, 58(5), 1887-1895.
- Yang, B., Li, W., Gu, Y., Cui, W., & He, X. (2012). Improved transformerless inverter with common-mode leakage current elimination for a photovoltaic grid-connected power system. *IEEE Transactions on Power Electronics*, 27(2), 752-762.
- Yang, Y., & Blaabjerg, F. (2015). Overview of single-phase grid-connected photovoltaic system. *Electric Power Components and System*, 43(12), 1352-1363.
- Zhu, N. (2013). *Common-Mode Voltage Mitigation by Novel Integrated Chokes and Modulation Techniques in Power Converter System*. Phd Thesis, Ryerson University, Toronto.